



TECHNISCHE
UNIVERSITÄT
DARMSTADT

Mesoporous and Crystalline Carbonaceous Materials

Mesoporöse und kristalline Kohlenstoffmaterialien

vom Fachbereich Chemie
der Technischen Universität Darmstadt

zur Erlangung des Grades

Doktor-Ingenieur
(Dr.-Ing.)

Dissertation
von
Hauke Christians

Erstgutachter: Prof. Dr.-Ing. Bastian J. M. Etzold

Zweitgutachter: Prof. Dr. Ulrike Kramm

Darmstadt 2022

Tag der Einreichung: 01.02.2022

Tag der mündlichen Prüfung: 23.05.2022

Hauke Christians Mesoporous and Crystalline Carbonaceous Materials

Jahr der Veröffentlichung der Dissertation auf TUprints: 2022

URN: urn:nbn:de:tuda-tuprints-203307

Tag der mündlichen Prüfung: 23. Mai 2022

Veröffentlicht unter CC BY-NC-ND 4.0 International

<https://creativecommons.org/licenses/>



Erklärungen laut Promotionsordnung

§8 Abs. 1 lit. c PromO

Ich versichere hiermit, dass die elektronische Version meiner Dissertation mit der schriftlichen Version übereinstimmt und für die Durchführung des Promotionsverfahrens vorliegt.

§8 Abs. 1 lit. d PromO

Ich versichere hiermit, dass zu einem vorherigen Zeitpunkt noch keine Promotion versucht wurde und zu keinem früheren Zeitpunkt an einer in- oder ausländischen Hochschule eingereicht wurde. In diesem Fall sind nähere Angaben über Zeitpunkt, Hochschule, Dissertationsthema und Ergebnis dieses Versuchs mitzuteilen.

§9 Abs. 1 PromO

Ich versichere hiermit, dass die vorliegende Dissertation selbstständig und nur unter Verwendung der angegebenen Quellen verfasst wurde.

§9 Abs. 2 PromO

Die Arbeit hat bisher noch nicht zu Prüfungszwecken gedient.

Darmstadt, den

H. Christians

Die vorliegende Arbeit wurde am Ernst-Berl-Institut für Technische und Makromolekulare Chemie der Technischen Universität Darmstadt unter der Leitung von Herrn Prof. Dr.-Ing. Dipl.-Kfm Bastian J. M. Etzold in der Zeit von März 2017 bis Dezember 2021 angefertigt.

Teile dieser Arbeit wurden bereits in der folgenden Publikation veröffentlicht, sowie auf Fachkonferenzen vorgestellt:

Publikation

H. Christians, K. Brunnengräber, J. Gläsel, S. Schweizer, B. J. M. Etzold

Mesoporous and Crystalline Carbide-Derived Carbons: Towards a General Correlation on Synthesis Temperature and Precursor Structure Influence

Carbon **2021**, 175, 215 - 222, DOI: 10.1016/j.carbon.2021.01.003

Poster

H. Christians, C. Prössl, J. Gläsel, B. J. M. Etzold

Graphitization of Activated Carbons via Vacuum Annealing

World Conference on Carbon, Madrid, Spanien **2018**

H. Christians, C. Prössl, J. Gläsel, B. J. M. Etzold

Graphitization of Activated Carbons via Vacuum Annealing

ProcessNet Jahrestagung, Aachen, Deutschland **2018**

Danksagung

An dieser Stelle möchte allen danken, die mich in den letzten Jahren angeleitet, beraten, geholfen, gefördert, unterstützt, gefordert, entlastet und begleitet haben. Auf vielfältige Weise haben diese Personen zum Gelingen dieser Arbeit beigetragen.

Mein erster Dank gilt meinem Doktorvater Prof. Dr.-Ing. Dipl.-Kfm Bastian J. M. Etzold für die Aufnahme in die Arbeitsgruppe, sowie gleichermaßen das Fördern und Fordern schon seit meiner Masterarbeit, für angeregte Diskussionen und für das spannende Promotionsthema.

Prof. Dr. Ulrike Kramm möchte ich für die Übernahme des Korreferats danken.

Prof. Dr.-Ing. Alfons Drochner möchte ich für seine Unterstützung schon seit dem Studium danken, für sein offenes Ohr und angeregte Gespräche.

Dr.-Ing. Jan Gläsel für die tolle Leitung der *Materials* Arbeitsgruppe, für sein Engagement für alle Doktoranden der Arbeitsgruppe, sowie für seine stets offene Tür egal, ob es um Arbeit oder Privates ging.

Mein Dank gilt all denjenigen, die für mich oder mit mir Charakterisierungen durchgeführt haben: Dr. Katrin Hofmann aus dem Arbeitskreis von Prof. Dr. Barbara Albert für die zahlreichen XRD-Messungen an den Aktivkohlen; Daniel Huth, Gregor Meyer und Phillip Reif aus dem Arbeitskreis von Prof. Dr. Marcus Rose für die nicht weniger zahlreichen XRD-Messungen an CDCs und Katalysatoren; Kai Brunnengräber für die Durchführung der Argon-Physisorptionsmessungen und die anschließende kritische Diskussion der Ergebnisse; Patrick Schmatz-Engert für die Einführung in "seine" Raman-Anlage und die Diskussionen zur Auswertung.

Ich möchte Carolin Prössl, Miriam Geißler und Sinem Bayram danken, die ich jeweils eine Zeit lang während ihrer Abschlussarbeiten oder Praktika betreuen durfte. Sie haben einen wertvollen Beitrag zu dieser Arbeit geleistet, in Form von Experimenten, Messungen, Auswertungen, aber auch Diskussionen und neuen Blickwinkeln.

Ein spezieller Dank gilt den Kollegen aus dem "V1-Büro", namentlich Dominik Ohlig, Florian Knaus, Hendryk Steldinger, Johannes Landwehr, Lucien Beisswenger, Marco Schöpp, Michael George, Miriam Geißler, Nicolai Schmitt, Sebastian Wöllner und Timothy Nowak. Sie machten die Promotion zu einer besonderen Zeit mit

Büro-Ausflügen, Uni-Olympiaden und viel Spaß innerhalb und außerhalb der Universität.

Mein Dank gilt weiterhin allen Mitgliedern der Arbeitsgruppe Etzold für eine tolle Zeit. Insbesondere Andreas Widjaja, Fabian Schmitt, Felix Herold, Kai Brunnengräber, Katharina Jeschonek, Konrad Krois, Lucas Hüfner, Niklas Oefner, Patrick Schmatz-Engert, Stefan Prosch und Stephan Schultheis für fachliche und weniger fachliche Diskussionen, für Grillabende, Blütenwanderungen, ChemCups und andere schönen Momente.

Zu guter Letzt möchte ich meiner Familie danken, die mich immer unterstützt hat und während meiner Promotionszeit noch gewachsen ist. Meinem Vater Stefan, der in mir die Faszination für Naturwissenschaften geweckt hat und der diese Arbeit sicherlich gerne gelesen hätte. Meiner Mutter Petra, die mich gefördert hat, die immer ein offenes Ohr hat und die auch eine tolle Oma ist. Meinen Geschwistern Malte und Nele, die immer für mich da waren. Meiner Tochter Reva, die mich zwar gerne mal von der Arbeit abgelenkt hat, die mir dabei aber unzählige schöne Momente geschenkt hat. Und meiner Frau Janine, die mich unterstützt hat, die mir den Rücken freigehalten hat, die Höhen und Tiefen mit mir geteilt hat und die ich über alles liebe.

Zusammenfassung

Kohlenstoffmaterialien werden aufgrund ihrer speziellen Eigenschaftskombinationen vielseitig eingesetzt, von hochtemperaturbeständigen Graphiten mit niedrigem elektrischen Widerstand als Elektrodenmaterialien, über gasdichte Werkstoffe in Gleitringanwendungen mit starker mechanischer Beanspruchung bis hin zu hochporösen Adsorptionsmaterialien. Zunehmend an Bedeutung gewinnen Kohlenstoffmaterialien mit mesoporösen Strukturen, aber hoher Temperaturbeständigkeit für den Einsatz in elektrochemischen Anwendungen, die Adsorption von Molekülen mit großer räumlicher Ausdehnung und weiteren Spezialanwendungen. Diese Eigenschaftskombination kann nicht mit "klassischen" Kohlenstoffmaterialien erzielt werden, weshalb die Entwicklung solcher Materialien im Fokus der aktuellen Forschung steht.

Diese Arbeit beschäftigt sich mit zwei möglichen Methoden solche Materialien zu erhalten, wobei es von besonderem Interesse ist, zu erforschen, wie sich die Eigenschaften der erhaltenen Kohlenstoffe mit Hilfe der Syntheseparameter gezielt steuern lassen. Durch Ausheizen von kommerziellen Aktivkohlen, stark mikroporöse und amorphe Materialien, im Temperaturbereich von 1000 bis 1900 °C konnten Kohlenstoffmaterialien mit stark erhöhter thermooxidativen Beständigkeit erhalten werden, die deutlich größere Poren aufwiesen. Es konnte gezeigt werden, wie durch Einstellen der Ausheiztemperatur und Auswahl des Ausgangsmaterials Porenstruktur und Kohlenstoffmikrostruktur in einem gewissen Maße gezielt beeinflusst werden können.

Die zweite Gruppe der in dieser Arbeiten untersuchten Materialien bilden die sogenannten karbidabgeleiteten Kohlenstoffe (CDC, *eng.: carbide-derived carbon*). Diese werden durch Chlorierung von Metallkarbiden bei erhöhten Temperaturen synthetisiert. Es konnte gezeigt werden, dass aus allen binären Karbiden mit Kochsalzstruktur hochkristalline Materialien mit Meso- und Makroporen erhalten werden können. Die Temperatur, bei der der Übergang von mikroporösen, amorphen Kohlenstoffen zu graphitischen Materialien beobachtet wird, hängt dabei direkt mit der Struktur des Ausgangsmaterials bzw. der Gitterkonstante in dieser zusammen. So konnte das erste Mal ein Zusammenhang zwischen diesen beiden Haupteinflussfaktoren in der Chlorierung und der erhaltenen Kohlenstoffstruktur gezeigt werden. Weiterhin wurden die CDCs exemplarisch als Trägermaterial für Platinkatalysatoren in der Sauerstoffreduktionsreaktion eingesetzt. Dabei haben die Eigenschaften der CDCs Auswirkungen auf die Güte der Katalysatorschicht auf der Arbeitselektrode, sodass überlagernde Effekte die Ergebnisse der elektrochemischen Untersuchungen beeinflussen können. So besteht noch Optimierungsbedarf, um genauere Messungen durchführen zu können und eindeutige Aussagen zu treffen. Trotzdem konnte gezeigt werden, dass CDCs prinzipiell dazu geeignet sind, als Modellmaterialien zu fungieren, um den Einfluss des Kohlenstoffträgers auf Katalysatoreigenschaften und -aktivität zu untersuchen.

Contents

List of Abbreviations and Symbols	viii
1 Introduction	1
2 State of the Art	3
2.1 Application of Crystalline Carbons with Good Surface Accessibility	3
2.1.1 Application in Electrochemistry	4
2.1.2 Application in Heterogeneous Catalysis	7
2.2 Synthesis Strategies for Mesoporous Bulk Carbonaceous Materials	10
2.2.1 Templated Synthesis Strategies	11
2.2.2 Carbide-Derived Carbons: Influence of Synthesis Temperature on Pore Structure	13
2.3 Synthesis Strategies for Crystalline and Porous Bulk Carbonaceous Materials	16
2.3.1 Graphitization via Heat Treatment	17
2.3.2 Carbide-Derived Carbons: Influence of Synthesis Temperature on Crystallinity	20
3 Objectives and Scope of the Study	22
4 Experimental Section	24
4.1 Carbonaceous Material Synthesis	24
4.1.1 Annealing of Activated Carbons	24
4.1.2 Chlorination of Metal Carbides	24
4.2 Material Characterization	27
4.3 Electrochemical Performance Testing	32
4.3.1 Preparation of the Platinum Loaded Catalyst	32
4.3.2 Three Electrode Setup	32
5 Results and Discussion	35
5.1 Activated Carbon as Precursor for Mesoporous and Crystalline Carbons	35
5.1.1 Influence of Annealing Parameters for Darco KB-G as Exemplary Activated Carbon	35
5.1.2 Influence of Activated Carbon Precursor	40
5.1.3 Conclusion	45
5.2 Metal Carbides as Precursor for Mesoporous and Crystalline Carbons	46
5.2.1 Influence of Chlorination Temperature	46



5.2.2	Correlation of Carbide Precursor Structure to Carbide-Derived Carbon Structure	52
5.2.3	Conclusion	54
5.3	Exemplary Application of Pt/C Catalysts in Oxygen Reduction Reaction	56
5.3.1	Deposition of Platinum on Carbide-Derived Carbons with Varying Properties	56
5.3.2	Effect of Thermal Presintering of Carbon Supported Platinum Catalysts	63
5.3.3	Conclusion	66
6	Conclusion	67
	Bibliography	69
	Appendix	78
A	Activated Carbon as Precursor for Mesoporous and Crystalline Carbons	78
B	Metal Carbides as Precursor for Mesoporous and Crystalline Carbons	81
C	Exemplary Application of Pt/C Catalysts in Oxygen Reduction Reaction	86

List of Abbreviations and Symbols

Abbreviations

ADT	accelerated durability test
atm	atmospheric pressure
BET	Brunauer-Emmett-Teller method
BWF	Breit-Wigner-Fano
CDC	carbide-derived carbon
CE	counter electrode
CV	cyclic voltammogram
<i>et al.</i>	and other (<i>et alterii</i>)
HPA	hexachloroplatinic acid
HPLC	high-performance liquid chromatography
IC-OES	inductively coupled plasma optical emission spectrometry
<i>in situ</i>	on site
IUPAC	International Union of Pure and Applied Chemistry
MFC	mass flow controller
ORR	oxygen reduction reaction
Pt	platinum
PTFE	polytetrafluoroethylene
RDE	rotating disk electrode
RE	reference electrode
rel.	relative
RHE	reversible hydrogen electrode
TPO	temperature-programmed oxidation
VA	vacuum annealing
WE	working electrode
XRD	X-ray diffraction

Symbols

β	full width at half maximum (XRD)	°
d_{Pore}	average pore diameter	nm
DLC	double layer capacitance	F g ⁻¹
E	potential	V
ECSA	electrochemical surface area	m ² g ⁻¹
FWHM	full width at half maximum (Raman)	cm ⁻¹
I	current	A
I_D/I_G	Raman intensity ratio	-
K	Scherrer constant	-
L_a	in-plane crystallite size	nm
L_c	out-of-plane crystallite size	nm
L_{Pt}	average platinum particle size	nm
λ	wavelength	Å
m	mass	g
MSA	mass specific activity	A mg ⁻¹
ν	scan rate	V s ⁻¹
Q	electrical charge	C cm ⁻²
R^2	coefficient of determination	-
SSA	specific surface area	m ² g ⁻¹
T	temperature	°C
θ	reflex position (XRD)	°
V_{Pore}	total pore volume	cm ³ g ⁻¹

1 Introduction

Carbon is one of the most abundant elements found on earth and exists in several allotropic modifications. Consequently, the application of carbonaceous materials is manifold and almost as old as mankind with one of the oldest findings dating back over 30,000 years where carbon black and charcoal were used as color pigments for cave-painting [1]. Further historical applications include charcoal for reduction of metal ores (8,000 B.C.), charcoal powder as medicine (500 B.C.), natural graphite for cart grease (1220) and pencils (1565), graphite for carbon electrodes (1854) and carbon brushes (1866), and many others [1]. Today, carbonaceous materials are specialized high-tech materials tailor-made for their respective applications. For example synthetic industrial diamond is extremely hard and thus used for cutting and drilling. It is further used in high power transistors and piezoelectric devices due to its wide band gap [2]. Graphite on the other hand is an excellent electrical conductor and thus used as electrode material. Its tribological properties enable the application as lubricant and the combination of high temperature stability and chemical inertness leads to many applications of graphite as crucibles, molds, and heater materials [2].

The wide range of properties of carbonaceous materials is complemented by the pore structure in porous carbons. High pore volumes and large inner surface areas resulting from very small pores give these materials exceptional adsorption properties. Thus, porous carbonaceous materials are widely applied as adsorbents for water treatment, gas purification, and food processing [3]. In catalysis, porous carbonaceous materials are often employed as support materials to be able to disperse the active phase and obtain large active surface areas with less active material. Furthermore, the carbon surface may contribute to the catalytic activity by interacting with reactants or the active phase [4]. Additionally, carbon can be employed as the catalysts itself in many reactions involving hydrogen, oxygen, and halogens by making use of the broad variety of surface functionalization possible on carbonaceous materials [5, 6]. Commonly, activated carbons are used in these kind of applications as they are usually highly porous, abundantly available, and generally cheap [1, 3, 6]. The exceedingly high surface areas of activated carbons are advantageous for most applications but come with very small micropores and a mostly amorphous microstructure.

The low structural order of activated carbons leads to a low stability in oxidative conditions at higher temperature. This excludes them from a number of catalytic applications like the oxidative dehydrogenation of hydrocarbons where the catalyst has to withstand temperature above 350 °C under an oxidizing atmosphere [5]. Furthermore, the slow mass transport due to small pore sizes as well as the inaccessibility of microporous structures for larger molecules have to be considered. Mesoporous materials have been found to be advanta-

geous in the adsorption of huge molecules like vitamins and dyes [7], in biosensing and drug delivery [8], as well as in the biodiesel production [9] for this reason. In the still fast growing field of electrochemistry, the pore structure of an applied carbonaceous material has to be able to accommodate metal clusters of sizes around 3 to 8 nm which have been found to be most active in the oxygen reduction reaction [10]. Likewise, mesoporous carbons are used as intercalation material in lithium-sulfur batteries in order to be able to confine the large Li_2S molecules [11, 12]. In addition, microporous / amorphous carbonaceous materials exhibit low electrical conductivity due to the large amounts of defects in the carbon microstructure. From these examples and numerous similar applications arises the need for carbonaceous materials with a reasonable but especially good accessible surface area while exhibiting a crystalline structure.

One class of carbons combining high crystallinity with an accessible surface are carbon nanomaterials like carbon nanotubes [13, 14], onion-like carbon [15], and carbon nanofibers [16]. Nevertheless, intrinsic drawbacks of nanomaterials, like difficulties in scale-up of the synthesis, health safety concerns and high costs, limit their industrial applicability [17, 18]. Thus, there is an increasing demand for non-nanosized carbonaceous materials which combine high crystallinity with meso- or macroporosity, but are obtained in a scaleable synthesis route.

2 State of the Art

2.1 Application of Crystalline Carbons with Good Surface Accessibility

Crystalline carbonaceous materials are widely used due to their thermooxidative stability, chemical inertness, electrical conductivity, and tribological properties. Porous carbonaceous materials on the other hand are used in applications where large surface areas are needed in order to increase the number of interactions between the carbon surface and certain molecules. In comparison with highly microporous materials, mesoporous or macroporous carbonaceous materials generally exhibit lower surface areas, but the larger pores have a considerably better accessibility. Carbonaceous materials with both high structural order and meso- or macroporosity are able to combine the advantages of crystalline materials with the excellent surface accessibility of large pores and enable the application in a variety of fields ranging from adsorption and chromatography to electrochemistry, heterogeneous catalysis, and some specialized applications.

Outstanding surface accessibility and sufficient surface area are necessary for the adsorption of large molecules. Making use of the hydrophobicity of their surface, mesoporous carbonaceous materials are applied for the adsorption of large hydrophobic molecules like vitamins, dyes and polymers [19]. Tamai *et al.* examined the adsorption of different dyes and vitamins on prepared mesoporous carbons in comparison to commercial microporous carbons [7]. A commercial activated carbon showed exceptional adsorption of relatively small dyes (long axis < 1.4 nm) greater than 170 mg g⁻¹ but poor adsorption of only 22 mg g⁻¹ for a large molecular weight dye (long axis 2 nm). The mesoporous carbonaceous materials on the other hand were found to adsorb more than 60 mg g⁻¹ of the large dye. For vitamins B₁, B₂, B₆, and B₁₂ a similar behavior was observed, where the adsorption of the large vitamin was considerably higher for the mesoporous materials. Furthermore, the adsorption of methylene blue [20], vitamin E [21], L-histidine [22], and other large molecules [23–25] on mesoporous carbonaceous materials was investigated in literature and found to be superior compared to microporous carbonaceous materials or mesoporous silica materials.

In high-performance liquid chromatography (HPLC), the excellent adsorption behavior for large molecules of mesoporous carbons in combination with a graphitic structure result in a unique chromatographic behavior of crystalline but porous carbonaceous materials. Their outstanding chemical stability allows the use in a wide range of pH and temperature conditions while the stable carbon microstructure enables the materials to withstand the considerable shearing forces encountered in HPLC [26–28]. Furthermore, appropriate surface areas and modifiable surface chemistry are necessary for a suitable adsorption capacity in HPLC applications

[26]. In comparison with conventional alkyl-bonded silicas, porous graphitic carbons as stationary phase in HPLC show increased retention of non-polar compounds and increased selectivity towards structurally related compounds [28]. Additionally, a high affinity of solutes of increasing polarity towards the graphite surface enhances the possibility to separate very polar and ionized molecules [28]. Already in 1986, Knox *et al.* used spherical carbon particles with crystallite sizes of 10 nm and a specific surface area (SSA) of $150 \text{ m}^2 \text{ g}^{-1}$ in HPLC applications [27]. They obtained good peak shapes for the elution of a wide range of monofunctional benzenes in chromatograms of high efficiency. The carbonaceous materials showed unique chromatographic properties while acting as strong hydrophobic adsorbent. Furthermore, they could be operated under typical HPLC conditions of pressure and flow rate. Nowadays, crystalline carbonaceous materials with appropriate porosity are used as the stationary phase in pharmaceutical and clinical applications [28–31], for the complex separations of biomolecules [28, 31–33], as well as other individual separation tasks [28, 31].

Crystalline carbonaceous materials with mesoporous structures were found to show outstanding performances in a number of very specialized applications. For example, Wiener *et al.* investigated the use of ordered carbon aerogels treated at high temperatures as high-temperature thermal insulation material [34]. The study found thermal conductivities above 2000 K for the materials which were a factor of five to ten lower than the ones for commonly applied materials. Yang *et al.* used well-ordered mesoporous carbon as the solid template for the synthesis of zeolites with a unique combination of mesopores and supermicropores [35]. Despite this variety of applications, the bigger part of mesoporous and graphitized carbonaceous materials are synthesized and studied in order to be used either in electrochemistry or heterogeneous catalysis. Thus, applications that can be assigned to one of these categories will be discussed in the following sections.

2.1.1 Application in Electrochemistry

Electrochemistry is a fast growing branch of chemistry which deals mostly with the production of electrical energy via chemical reactions and the changes in chemical systems induced by an electric current [36]. Materials that can be used in electrochemical applications are required to exhibit excellent electron conductivity and electrochemical stability. Furthermore, a reasonable specific surface area and especially good accessibility of the surface via larger pore sizes are necessary for most applications. Crystalline carbonaceous materials with mesoporous structures fit these requirements perfectly and are thus topic of current research in electrochemistry.

One particularly interesting topic resulting from the energy transition away from fossil-based electricity is the storage of renewable electrical energy. Rechargeable lithium-sulfur batteries exhibit extremely high theoretical specific capacity and energy density of 1675 mAh g^{-1} and 2600 Wh kg^{-1} , respectively [37]. Carbonaceous materials are commonly used as intercalation material in the sulfur cathode as sulfur and Li_2S itself are naturally electronically and ionically insulating. Beside a high electron conductivity and high electrochemical stability to withstand a large number of charging cycles, the applied carbonaceous materials need to accommodate

sulfur particles which undergo volume expansions up to 80 % upon lithiation [11, 37]. For this task, larger pores are advantageous. Ji *et al.* used a composite of highly ordered mesoporous carbon (CMK-3) and sulfur to obtain nearly 80 % of the theoretical capacity of sulfur while maintaining a high conductivity of 0.2 S cm^{-1} and achieving a good cycling stability [38]. This was achieved by growing sulfur nanofillers inside the 3.3 nm diameter channels of the CMK-3, where most of the $21 \text{ cm}^3 \text{ g}^{-1}$ pore volume of the structure was filled with sulfur. Thus, a close contact of the sulfur with the conductive carbon framework was ensured and the active material was freely accessible for the redox processes to take place. Furthermore, Wang *et al.* showed that soluble polysulfide intermediates can be trapped efficiently inside the mesopores with diameters about 7 nm of carbonaceous materials preventing capacity fading through shuttle reactions and deposition of lithium-sulfur species on the anode [12]. He *et al.* employed hollow carbon nanospheres featuring a specific surface area of $550 \text{ m}^2 \text{ g}^{-1}$, a pore volume of $3.3 \text{ cm}^3 \text{ g}^{-1}$, and most importantly a narrow pore size distribution around 5 nm [11]. This led to a highly uniform filling with sulfur resulting in short lithium diffusion length similar in all particles. With this, it was demonstrated that the capacity and stability of lithium-sulfur batteries can be further increased by tuning the porosity of the carbon intercalation material towards uniform pore sizes and increased sulfur loading.

In electric double layer capacitors, the electrode material plays an important role in determining both capacitance and performance [39]. On the one hand, high specific surface areas but also the accessibility of the pores are important as even larger ions of organic electrolytes need to be accommodated in the pore structure [40]. On the other hand, high electron conductivity is needed to achieve high power densities [41]. Considering these correlations, crystalline carbonaceous materials with good surface accessibility present themselves as predestined electrode materials for electric double layer capacitors. Accordingly, Gao *et al.* synthesized partially graphitic ordered mesoporous carbons using a triblock-copolymer as template, phenolic resol as carbon source and ferric oxide as graphitizing catalyst [42]. The obtained carbonaceous material exhibits uniform bimodal pore sizes of 1.5 and 6 nm, with a high specific surface area of $1300 \text{ m}^2 \text{ g}^{-1}$, and a pore volume of $1.50 \text{ cm}^3 \text{ g}^{-1}$. Qualitative X-ray diffraction (XRD) analysis and Raman measurements showed the partial graphitization of the material resulting from the application of iron oxide. With this, large capacitances of 155 F g^{-1} over a wide range of scan rates up to 200 mV s^{-1} were achieved. Furthermore, Li *et al.* demonstrated good electrochemical stability with 94 % capacitance retention after consecutive 2500 cycles using graphitic carbon spheres with a Raman intensity ratio I_G/I_D of 0.99 exhibiting narrow distributions of micropores (1 nm) and mesopores (7.5 nm) [20].

Fuel cells are supposed to be a major source of clean energy for mobile and stationary application in the future [43, 44]. Although several commercial applications have been launched, improvements regarding the lifetime of fuel cell are necessary in order to enhance their competitiveness [45–47]. One of the most important factors to be considered is the degradation of the electrocatalysts employed, which are commonly based upon carbon-supported platinum catalysts [44, 48]. Five major degradation mechanisms were identified in literature and are illustrated in figure 2.1: Carbon corrosion, platinum dissolution, Ostwald ripening, agglomeration, and particle detachment [44, 49, 50].

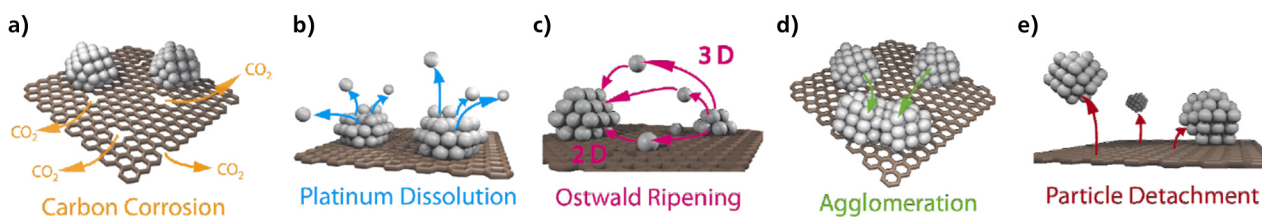


Figure 2.1: Simplified illustration of the major degradation mechanisms for carbon-supported platinum catalysts in fuel cells. Adapted from Meier *et al.* [49].

Carbon corrosion (figure 2.1a) results in carbon loss and thus loss of catalyst activity by reducing the contact with the current collector leading to an increased electric resistance [44, 51]. Additionally, the hydrophilicity of the carbon surface is increased resulting in decreased transport of oxygen to the active material due to a flooding of the pores with water [44, 49]. A collapse of the carbon structure may create higher amounts of isolated pores and thus reduces the porosity of the catalyst. This results in mass transport limitations for the reactants decreasing the catalyst activity further [49, 52]. Furthermore, carbon corrosion can lead to decreased interaction between platinum particles and the support material, resulting in platinum agglomeration or particle detachment (figures 2.1d and e) [49, 50]. The use of crystalline / graphitic carbonaceous materials suppresses carbon corrosion significantly as these materials are thermally and electrochemically more stable than amorphous carbonaceous materials [53–55]. Platinum dissolution (figure 2.1b) may result in the loss of active material or in redeposition to form larger platinum particles (Ostwald ripening, figure 2.1c), both possibilities resulting in a loss of electrochemical surface area and thus a decrease in catalyst activity [44, 49]. This mechanism is influenced by the platinum particle size, whereas small particles are less stable than larger ones and platinum cluster sizes between 3 and 4 nm have shown reduced dissolution [49, 56].

In summary, the carbon support for electrocatalysts employed in fuel cells needs to be crystalline to withstand the thermal and electrochemical stress, but provide sufficient surface area to enable a good dispersion of the active material. Furthermore, the pore structure needs to be easily accessible with pores large enough to accommodate the ideal cluster size of 3 to 4 nm. These requirements led to the application of new crystalline mesoporous carbonaceous materials as more durable fuel cell catalyst supports [57, 58]. For example, Shanahan *et al.* employed graphitic mesoporous carbons obtained via a soft-template method with subsequent heat-treatment at 2600 °C [59]. The material exhibited a pore size of 9 nm and showed sharp X-ray diffraction reflexes attributed to graphitic structures. After 16 h of being exposed to a constant potential of 0.9 V, the platinum catalyst with this carbonaceous support material lost 14% of its catalytic surface area. This was a significant improvement compared to a conventional catalyst supported on carbon black, which under the same conditions suffered a loss of catalytic surface area of 39%. Using highly ordered graphitic mesoporous carbon as support material, Su *et al.* improved the specific activity of a platinum catalyst for methanol oxidation [60]. The carbonaceous material was obtained from chemical vapor deposition of benzene on a silica hard-template and retained the pore size of the silica of 10 nm. Furthermore, it exhibited pronounced graphitic structures

shown in XRD, transmission electron microscopy and Raman spectroscopy. Catalysts based on this support material showed specific activities of 1.25 - 1.39 mA cm⁻², which were drastically higher than the specific activity of a commercial catalyst based on carbon black (0.57 mA cm⁻²).

Further increase of the stability of the small platinum particles could be achieved by encapsulating the particles inside the carbon pore structure and thus preventing the particles from further growths as well as decreasing the platinum loss [61–64]. With this goal, Galeano *et al.* used hollow graphitic spheres with a narrow pore size distribution as carbon support for a platinum electrocatalyst [65]. Small platinum particles were brought onto the carbon surface via incipient wetness impregnation and subsequently underwent a high temperature annealing up to 900 °C in order to confine the growing particles inside the mesoporous carbon structure. The annealing step led to an increase in platinum particle size from < 2 nm to 3 - 4 nm due to sintering processes, with the particles confined into the 5 nm diameter pores of the support material. The obtained catalysts showed significantly improved preservation of the platinum surface area after several thousand degradation cycles compared to a conventional carbon-supported platinum catalyst. Identical location transmission electron microscopy provided images that showed a significant loss of platinum particles for the conventional catalyst but only a small change for the catalyst with confined platinum particles. Yang *et al.* used a similar confinement method to stabilize platinum particles inside hollow carbon spheres and compared the stability to a catalyst with the same support material but with platinum particles on the surface of the carbonaceous material [66]. After 2000 potential cycles (0 - 1.1 V), the catalyst with confined platinum particles retained about 60 % of its electrochemical surface area while the comparison catalysts lost more than 70 % of its surface area. These two examples show the effectiveness of pore confinement in increasing the stability of platinum catalysts in electrochemical applications.

2.1.2 Application in Heterogeneous Catalysis

In heterogeneous catalysis, carbonaceous materials in general are used as catalyst support material due to their stability in various chemical environments and their large surface areas which enable the dispersion of the active components. In many applications, conventional activated carbons are preferred over mesoporous carbonaceous materials because they usually exhibit much higher surface areas and thus better dispersion of the active components can be achieved. Nevertheless, mesoporous carbons offer advantages in reaction systems, where a good accessibility of the surface area is of importance to enhance the mass transport of large molecules [67]. Several studies showed the superiority of mesoporous carbon supported catalysts over comparable conventional activated carbon supported catalysts in the conversion of cellulose to different products. Pang *et al.* studied the conversion of cellulose to hexitols with carbon supported Ni-based bimetallic catalysts and achieved hexitol yields above 50 % with mesoporous carbons and below 15 % for conventional activated carbons [68]. Furthermore, it was found that the dispersion of nickel particles was more uniform using mesoporous carbon supports in contrast with the conventional carbon support where larger nickel clusters could be found. A similarly improved performance was demonstrated by Ji *et al.* for the conversion of

cellulose into ethylene glycol with carbon supported tungsten carbide catalysts [69] and by Kobayashi *et al.* for the hydrolysis of cellulose to glucose with carbon supported ruthenium catalysts [70].

A huge drawback for most carbonaceous support materials is the oxidation to carbon dioxide under oxidative conditions at elevated temperatures. The oxidation rate for bulk carbon in general depends on the number of active sites on the material, i.e. carbon atoms on edges and defects [71–73]. Accordingly, graphitized and thus highly crystalline carbonaceous materials are able to withstand much higher temperatures than conventional activated carbons with their defect-rich structures [4, 74, 75]. This diminishes the drawback concerning the thermooxidative stability of carbonaceous materials significantly. Using heat treatment to increase the structural order of activated carbons, Kang *et al.* studied the activity and stability of platinum catalysts for the CO oxidation supported on carbonaceous materials with varying degrees of graphitization [75]. It was found that the graphitization not only increases the stability under reaction conditions considerably, but also improved the activity. Supposedly, interactions of the graphitic planes with the metal particles lead to an increased concentration of surface Pt⁰ which is the active species in CO oxidation. Combining the effects of larger and thus more accessible pores with high structural order, graphitic mesoporous carbons are sought support materials for catalysts in various reactions. These include Ce-doped nickel catalysts for steam-reforming of toluene [76], molybdenum carbide catalysts [77] and ruthenium catalysts [78] for the hydrogenation of carbon monoxide, CoO catalysts for the Fischer-Tropsch synthesis [79], and many more.

Apart from its use as support material, carbon is able to act as the heterogeneous catalyst itself. Aside from the obvious advantage of eliminating expensive noble metals in the catalyst, carbon exhibits unique properties advantageous in catalysis [5, 80]: (i) the structures, functionalities and properties of the carbon surface can be modified to a great extent and thus be optimized for different desires and active sites, (ii) the porous structure of many carbonaceous materials provides a large active surface area, (iii) with many important reactants, there is no subsurface or intercalation chemistry for carbon, thus minimizing the chemical complexity. Reactions taking place under oxidizing conditions at elevated temperatures require catalysts that are able to withstand these conditions without degradation. In the context of carbon catalysis, only carbonaceous materials with a high structural order are capable of this. Furthermore, a sufficiently large surface area is necessary to provide a high amount of active sites in order to achieve high conversion rates. Thus, there is a great demand for crystalline carbonaceous materials with meso- or macroporosity to be used as catalysts in various reactions [4, 5, 81].

The selective dehydrogenation of hydrocarbons is a class of reactions which presents the challenge that the products are often more active than the reactants leading to the undesired deep oxidation to CO and CO₂. Conventional metal-free carbonaceous materials have been shown to exhibit high activity and selectivity at mild reaction conditions but poor stability [5, 82]. Thus, a number of more graphitic carbonaceous materials have been studied as catalysts for these kind of reactions. Su *et al.* employed highly ordered mesoporous carbon as catalyst for the oxidative dehydrogenation of ethylbenzene to styrene and observed high activity and selectivity as well as a good stability compared to conventional carbon catalysts [83]. By modifying a

graphitic mesoporous carbon catalyst with phosphorous heteroatoms, Schwartz *et al.* improved the selectivity of the material in the oxidative dehydrogenation of isobutane to isobutene [84]. This underlines the versatility of the carbon surface and how it can be easily modified to further improve catalyst performances. Herold *et al.* developed a new hybrid amorphous/graphitic carbon which yields a highly crystalline carbonaceous material with both micro- and mesoporosity upon selective oxidation of the amorphous domains [82]. The resulting carbon was employed as catalyst in the oxidative dehydrogenation of ethanol and showed excellent selectivity and conversion as active material. Furthermore, the feasibility of mesoporous and graphitic carbon catalysts in direct dehydrogenation reactions was shown by Gläsel *et al.* by employing carbide-derived carbons obtained from titanium carbide at high temperatures [17].

Carbon nanomaterials comprise a class of carbonaceous materials with a controlled nanoscale dimension and crystalline microstructure such as carbon nanotubes [13, 14], onion-like carbons [15], and carbon nanofibers [16]. They usually exhibit high electrical and thermal conductivity, and mechanical strength as well as extremely low packing density [85]. These materials possess no inner porosity, thus their active centers are located at their outer surface and are highly accessible. Due to these combination of properties, different kinds of carbon nanomaterials were reported in literature to catalyze a multitude of reactions including oxidation reactions [86–88], transesterification [89], hydrolysis [90], and many more [5, 80, 81, 91, 92]. Nevertheless, the applicability of carbon nanomaterials in heterogeneous catalysis is limited due to difficulties in scale-up of the synthesis, large pressure drop, unclear health risks, and costs [17, 18, 82]. Therefore, it is the topic of several current research efforts to develop non-nanosized bulk carbonaceous materials which combine high crystallinity with meso- or macropores to provide both accessible surface area and stability [82, 93–96].

2.2 Synthesis Strategies for Mesoporous Bulk Carbonaceous Materials

When discussing the application of carbonaceous materials, their pore structure is an important factor. The porosity is one figure of merit for it and is defined as the ratio of the total pore volume to the volume of the particle or agglomerate [97]. It has major influences on the materials mechanical and physical properties like density, stability, conductivity, and adsorption capacity. However, porosity in itself is not able to fully describe the pore system of a material. The pore structure of materials exhibiting the same porosity may differ in the morphology of the pores, as well as their interconnection and accessibility. Often, pores are classified with regard to their size and three classes are recommended by IUPAC differing in their width [98]: (i) *micropores* (< 2 nm), (ii) *mesopores* (2 - 50 nm), and (iii) *macropores* (> 50 nm). Most carbonaceous material's pore structures are made up of pores of different morphologies falling into different categories. A variety of studies found in literature focus on methods to control and manipulate the pore size distribution of carbonaceous materials in order to tune materials towards specific applications.

One of the most used methods to create a pore structure within carbonaceous materials is the activation process either in the form of physical activation with gases (steam, CO₂) or chemical activation with oxidizing agents (zinc chloride, phosphoric acid, potassium hydroxide). During the process, parts of the carbonaceous material are burned off resulting in the development of porosity due to creation of new pores, opening of enclosed pores, and widening of existing pores [99]. Manipulating the process parameters of temperature, amount of oxidizing agent and time, the result of the activation process can be influenced and different kind of pore structures can be obtained. In order to produce mesoporous activated carbons, combinations of physical and chemical activation methods are employed. For example, Hu *et al.* combined chemical activation using ZnCl₂ with CO₂ activation at 800 °C and obtained mesoporous carbonaceous materials from coconut shells with surface areas according to the Brunauer-Emmett-Teller method (BET) above 2000 m² g⁻¹ and total pore volumes up to 1.9 cm³ g⁻¹ [100]. Manipulating the ZnCl₂/Shell ratio, it was possible to tune the pore size of the materials with higher amounts of oxidizing agents resulting in a shift of the pore size distribution towards larger pores as evidenced by an increase in mesopore volume. A ZnCl₂/Shell ratio of 3 led to a total pore volume of 1.91 cm³ g⁻¹ with 71 % of it being mesopore volume. Furthermore, with the help of metals or organometallic compounds, a catalytic activation can be performed in order to form mesopores. Tamai *et al.* studied the effect of a variety of organo rare-earth metal complexes in combination with steam activation of petroleum pitch [7]. Using only the pitch precursor without catalytic activation, an activated carbon was obtained at 930 °C with a BET surface area of 240 m² g⁻¹, an average pore size of 2.4 nm and mesopores made up only 5.7% of the total pore volume (labeled as 'mesopore ratio' in this publication). Using Ln(C₅H₅)₃ complexes (Ln = Y, La, Nd, Sm, Gd, Tb, Er, Yb, Lu) in addition to the steam activation under the same conditions, the average pore size of the obtained activated carbons could be increased up to 5.8 nm with a mesopore ratio of 81.3%. Based on phenolic resins carbonized at 900 °C in the presence of cobalt-acetylacetonate, Oya *et al.* were able to obtain mesoporous carbon fibers upon steam activation at 750 to 900 °C [101]. While the pristine carbons showed barely any mesopore volume, mesopore volumes above 0.3 cm³ g⁻¹ made up more than 50% of the total pore volumes of the carbonaceous materials treated

with cobalt-acetylacetonate. Other reported methods to obtain mesoporous carbonaceous materials include combinations of CO₂ with iron/nickel on polyfurfuryl alcohol, with boric acid on viscose rayon cloth, and aqueous Fe(NO₃)₃ on bamboo and sawdust [102].

Another approach is the carbonization of precursor materials already featuring the desired pore structure like aerogels or cryogels. These materials can be obtained from the sol-gel polycondensation of resorcinol or melamine with formaldehyde and subsequent drying in order to preserve the gel structure [103]. Supercritically dried gels are called *aerogels* while freeze-dried gels are called *cryogels* [104]. The gels can be obtained in form of monoliths, beads, powders or thin films and maintain their structure upon carbonization [105]. The prepared carbon aerogels are made up of a structure of interconnected nanosized primary particles which exhibit a microporous structure. Mesopores and macropores result from the inter-particle structure of the overall gel enabling the control of micropores and mesopores independently by either varying the primary particles or the inter-particle structure [105, 106]. Additionally, both micropore and mesopore volume can be increased further via activation. This was used by Hanzawa *et al.* to increase the micropore volume of an resorcinol-formaldehyde based carbon aerogel from 0.12 to 0.66 cm³ g⁻¹ and its mesopore volume from 1.19 to 1.98 cm³ g⁻¹ via CO₂ activation at 1173 K [107]. A new approach to control the structure of a precursor which is maintained upon carbonization was presented by Steldinger *et al.* [108]. A combination of stereolithography 3D printing and photoinduced copolymerization with liquid porogen templating lead to mechanically stable structures with a controlled porosity and pore sizes up to 100 nm. Additional CO₂ activation of the carbonized material also enables further tuning of the pore structure.

2.2.1 Templated Synthesis Strategies

The application of a template as mold to guide the carbon structure during the carbonization process is a widely used concept and can be divided into two categories: *hard template* methods use presynthesized organic or inorganic templates, while *soft template* methods utilize self-assembly of organic molecules to generate nanostructures [67]. With these methods, carbonaceous material can be obtained with a well-defined architecture and relatively narrow pore size distribution [109].

Figure 2.2 illustrates the process steps involved in the hard template method [19, 110]: (i) preparation of a porous template with the well-defined structure; (ii) introduction of suitable carbon precursor into the pores of the template by wet impregnation or chemical vapor deposition; (iii) Carbonization of the carbon precursor; (iv) removal of the hard template. The result is a continuous carbon framework with a pore structure that is defined by the template's structure. Lee *et al.* used the mesoporous silica *MCM-48* as a template to obtain mesoporous carbonaceous materials [111]. Phenol and formaldehyde were brought into the pores of the template under reduced pressure and polymerized at elevated temperatures under nitrogen atmosphere. Subsequent carbonization under nitrogen flow at 700 °C for 7 h and dissolution of the silica framework using hydrofluoric acid yielded a carbonaceous material exhibiting a uniform pore size of 2.3 nm with a high specific

surface area of $1257 \text{ m}^2 \text{ g}^{-1}$. Ryoo *et al.* employed the same silica template but using sucrose as carbon precursor [112]. Catalyzed with sulfuric acid, the precursor was carbonized before the template was removed with a sodium hydroxide solution. The resulting carbon exhibited micropores within the amorphous carbon framework and mesopores where the silica template was removed with a specific surface area of $1380 \text{ m}^2 \text{ g}^{-1}$. In this way, a multitude of different ordered mesoporous silicas were applied as hard templates resulting in various mesoporous carbonaceous materials with pore structures determined by the silica's structure [19, 67]. Other materials employable as hard template for mesoporous carbonaceous materials include colloidal silica particles [113, 114], silica / aluminosilicate gels [115–117], anodic aluminum oxide [118, 119], and polymer beads [120].

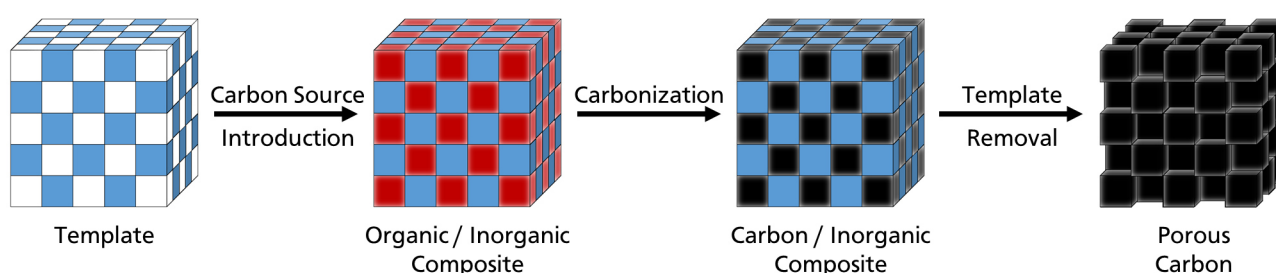


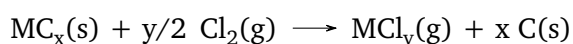
Figure 2.2: Schematic illustration of the process for the preparation of porous carbon from porous inorganic hard templates. Adapted from Kyotani *et al.* [110].

The soft template method does not use presynthesized templates but instead utilizes cooperative assembly between structure-directing agents and organic carbon precursors in solution. Usually, Amphiphilic molecules like surfactants and block copolymers are used as structure-directing agents as they form micelles in suitable solvents and thus create a template *in situ*. Together with the carbon precursor, mostly phenol resins, an ordered mesophase develops which is stabilized via thermal or catalytic cross-linking. During the carbonization of the carbon precursor, the template is removed and a porous carbonaceous material is obtained [19, 67, 121, 122]. One of the first methods to form mesoporous carbonaceous materials in this way was reported by Liang *et al.* [123]. The commercial triblock copolymer (Pluronic F127) mixed with phloroglucinol and formaldehyde in ethanol and water were used to obtain ordered carbon with a specific surface area of $288 \text{ m}^2 \text{ g}^{-1}$ and broad pore size distribution in the range of 5 to 10 nm. Furthermore, with the same method, carbonaceous materials in the forms of monoliths, fibers, and films were prepared, exhibiting higher specific surface areas and narrower pore size distributions in the mesopore range. Using three different commercial triblock copolymers (P123, F127, F108) and a phenolic resin, Meng *et al.* demonstrated how the choice of structure-directing agent and the carbon precursor / template ratio influences the pore structure of the resulting carbonaceous materials [124]. Materials with BET surface areas ranging from 130 to $1490 \text{ m}^2 \text{ g}^{-1}$ and average pore sizes from 2.0 to 7.4 nm were obtained. Generally, an increasing carbon content led to the formation of smaller pores and higher surface areas. Another parameter to consider is the carbonization temperature as Meng *et al.* also reported the decrease of the average pore size from 7.4 to 5.9 nm upon increasing the temperature from 400

to 800 °C [125]. These examples show the complexity of controlling the porous structure with this method, particularly as solvent, carbon precursor and degree of cross-linking play important roles as well [67, 122].

2.2.2 Carbide-Derived Carbons: Influence of Synthesis Temperature on Pore Structure

In the context of controlling the pore structure of carbonaceous materials, carbide-derived carbons (CDCs) are of high interest due to their tuneability. In order to form carbons from carbides, a selective extraction of metal or metalloid atoms from the carbide precursor is necessary. The most economic and scaleable and for this reason most common method is chlorination wherein the metals are chemically extracted at elevated temperatures and ambient pressure with the help of chlorine [126]. The chlorination of different carbides follows the general reaction [127]:



The reaction yields solid carbon and gaseous metal chlorides, which are carried away by excess chloride and carrier gas. The method was first used with silicon carbide for a large-scale synthesis of silicon tetrachloride, where carbon was initially the undesired byproduct [128]. This established process shows the possibility of an easy scale-up of CDC synthesis. Another factor for a possible commercial CDC process is cost reduction by the utilization of high-purity metal chlorides. An example for the high demand of those chlorides is titanium tetrachloride, a byproduct of CDC synthesis from titanium carbide. The hydrolysis of $TiCl_4$ is the most common commercial route to synthesize TiO_2 [129–131]. Via chlorination, CDCs can be obtained from a multitude of binary and ternary carbides like Al_4C_3 [132], B_4C [133], Cr_xC_y [133], HfC [127, 134, 135], Mo_2C [136], NbC [127, 134, 135, 137], SiC [138], TaC [127, 134, 135], TiC [139], VC [127, 134, 135, 140], WC [127, 134, 135, 141], ZrC [127, 134, 135, 142], Ti_3SiC_2 , Ti_2AlC , and Ta_2AlC [143, 144]. In order to remove residual chlorine from the CDC, post-synthesis treatment with hydrogen, ammonia or an inert gas is commonly employed at reaction temperature or at lower temperatures [126, 145]. In addition, post-synthesis treatments with hydrogen and ammonia are able to make clogged pores accessible and result in increased pore volume and specific surface area without affecting the carbon microstructure [146].

During the chlorination process, the carbon layer is formed in the geometrically outmost part of the carbide by an inward growth as illustrated in figure 2.3. In this schematic view, the particle on the left side consists completely of carbide, as represented by the grey color on the outside and in the inside shown by the pyramidal sectional view. After a short time of chlorination, the shell of the depicted particle is black, representing the formation of carbon, while the inside is still made up of carbide (grey center of the sectional view). After a longer time of chlorination, the particle consists completely of carbon throughout the whole sectional view. This so-called shrinking-core mechanism was found experimentally in form of a clear reaction front [147–149]. Knorr *et al.* successfully represented the shrinking-core mechanism in a transient reaction engineering model for the chlorination of SiC [150]. Another feature of the CDC synthesis is that it represents a conformal transformation process [151, 152]. This means, that the original shape and volume of the carbide

is maintained throughout the reaction which allows the synthesis of metal carbides coated with CDC with a precise control over the coating thickness [153].

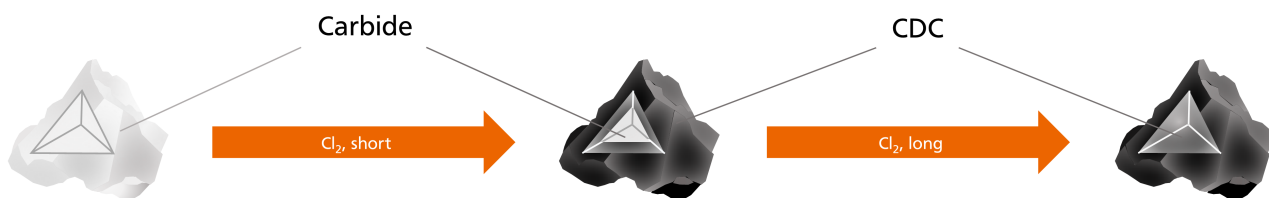


Figure 2.3: Schematic illustration of the shrinking-core mechanism including a pyramidal sectional view of the particle. Upon chlorination, the carbide particle on the left side is converted to a carbon particle of the same shape by an inward growth. Stopping the chlorination after a short time results in a particle with a carbon shell (black) and a carbide core (grey).

Anyway, the most remarkable characteristic of carbide-derived carbons is the tuneability of their pore structure. In general, the bulk porosity of CDCs is very high and dependent on carbide precursor and synthesis temperature. Figure 2.4 summarizes experimental results from literature regarding the specific surface area and total pore volume of CDCs from different carbide precursors with respect to the synthesis temperature.

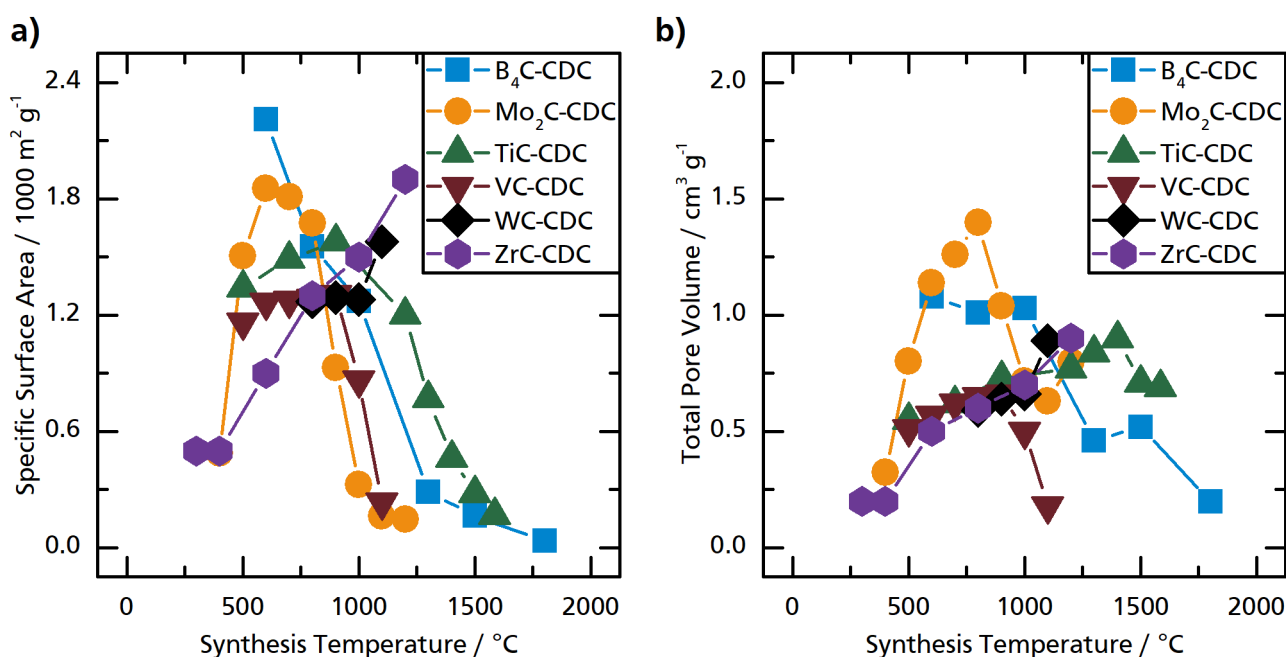


Figure 2.4: Influence of synthesis temperature on **a)** specific surface area and **b)** total pore volume for CDCs from B₄C [154], Mo₂C [136], TiC [17, 139], VC [140], WC [141], and ZrC [142].

For most carbide precursors, it can be seen that specific surface area and total pore volume are initially increasing with increasing synthesis temperature up to a certain point, resulting in microporous materials. Increasing the synthesis temperature further leads to a decrease in SSA and pore volume and slightly increasing

pore sizes. Just a few publications studied the synthesis of CDCs at temperatures above 1200 °C. For TiC [17, 155] and B₄C [154] it could be shown, that above 1200 °C mesoporous or even macroporous structures begin to form. On the other hand, CDCs from VC show mesoporous structures already at lower temperatures [140]. Other carbide precursors, like silicon carbide [138], zirconium carbide [142], tungsten carbide [141], and others [135], seem to result in microporous CDCs over the entire temperature range studied. This shows that both chlorination temperature and carbide precursor play an important role in controlling the porosity of carbide-derived carbons. Up to now, the combined influence of both parameters could not be explained completely and is still subject of current research.

2.3 Synthesis Strategies for Crystalline and Porous Bulk Carbonaceous Materials

In addition to the textural properties discussed in the previous section, the carbon microstructure is an important characteristic of a carbonaceous material. It includes the hybridization of the carbon atoms, their bonds to their nearest neighbors, as well as the long-range order of the material. Diamond is one of the naturally occurring carbon allotropes and represents one extreme of a range of carbonaceous materials by being formed completely from sp^3 -hybridized carbon atoms. Every carbon atom is bonded tetrahedrally to four other carbon atoms forming a three-dimensional structure which is rigid and isotropic. The unit cell of the most common cubic diamond structure is depicted in figure 2.5a and exhibits bond lengths of 0.154 nm [2]. The strong covalent bonds between the carbon atoms make diamond a very hard material with a density of 3.515 g cm^{-3} but a bad conductor due to the lack of a conjugated π bond system [156]. Graphite represents the other extreme of the range of carbonaceous materials by being formed from sp^2 -hybridized carbon atoms and is the other naturally occurring carbon allotrope. Its anisotropic structure is made up of separate basal planes which are layered parallel to each other. In a single plane, called graphene, carbon atoms form a conjugated system of aromatic six-membered rings in a hexagonal lattice with a bond lengths of 0.142 nm as depicted in figure 2.5b [2]. π orbitals perpendicular to the basal planes give rise to van der Waals forces between them resulting in a regular interlayer spacing of 0.335 nm [157]. Figure 2.5c depicts the unit cell of hexagonal graphite with a stacking sequence of ABA where the carbon atoms in every other layer are superimposed over each other. Graphite is the thermodynamically most stable allotrope of carbon at standard conditions. It is mechanically soft and less dense than diamond (2.266 g cm^{-3}) but an excellent conductor of electricity [2, 156]. Imperfections in the crystal structure, such as vacancies, stacking faults, disclination or impurities influence the bulk properties of graphite. For example, graphene sheets without a common orientation make up turbostratic graphite, which shows isotropic properties [2].

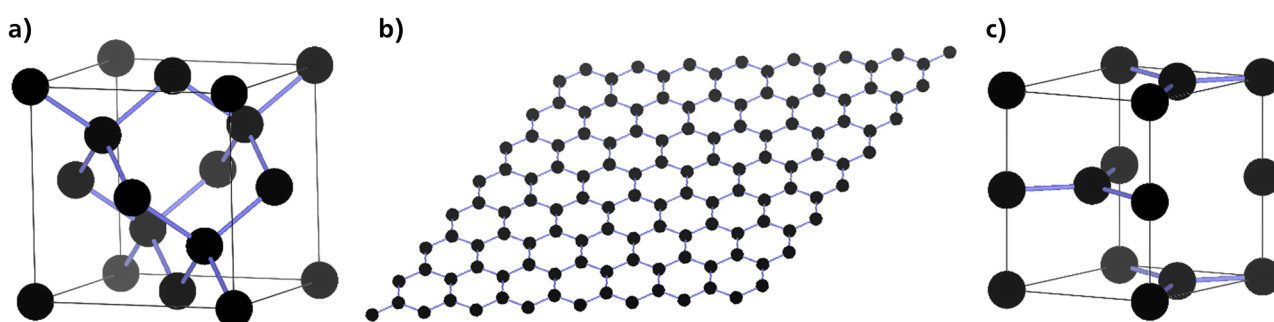


Figure 2.5: **a)** Cubic unit cell of diamond, **b)** structure of graphene sheet, and **c)** hexagonal unit cell of graphite with ABA stacking.

Most carbonaceous materials usually do not consist of either sp^2 or sp^3 hybridized carbon exclusively but are rather made up of a mixture of both. Thus, they are mostly amorphous and do not exhibit a pure crystalline

diamond or graphite structure. Nevertheless, amorphous carbonaceous materials can contain graphitic domains in which a small amount of carbon ribbons are stacked. These crystallites are characterized by their size in-plane (L_a) and out-of-plane (L_c) as well as their interlayer spacing. With these data from X-ray diffraction analysis, the material's thermooxidative stability as well as Raman measurements, the structural order of carbonaceous materials can be evaluated.

2.3.1 Graphitization via Heat Treatment

The structural order, or in other words the crystallinity, of a carbonaceous material can be increasing via heat treatment under nonoxidative conditions. In this context, Franklin *et al.* coined the term of "graphitizing" carbons by describing materials that are able to partially develop three-dimensional graphite structures upon heating to 3000 °C in contrast to "non-graphitizing" carbons [158]. It was found that the structure of graphitizing carbons already resembles the graphite structure with small crystallites that are almost parallel to each other. The heat treatment of these carbons result in a rearrangement of these crystallites in regard to each other forming larger crystalline structures. Non-graphitizing carbons on the other hand usually exhibit more porous structures and small crystallites with a mutually random orientation. Due to the strong cross-linking in these material, the rigid crystallites cannot be moved enough upon heat treatment to form graphite-like layers exceeding a size of 7 nm. Figure 2.6 gives an illustration of the structural development in carbonaceous materials during heat treatment up to the formation of a graphite lattice [159].

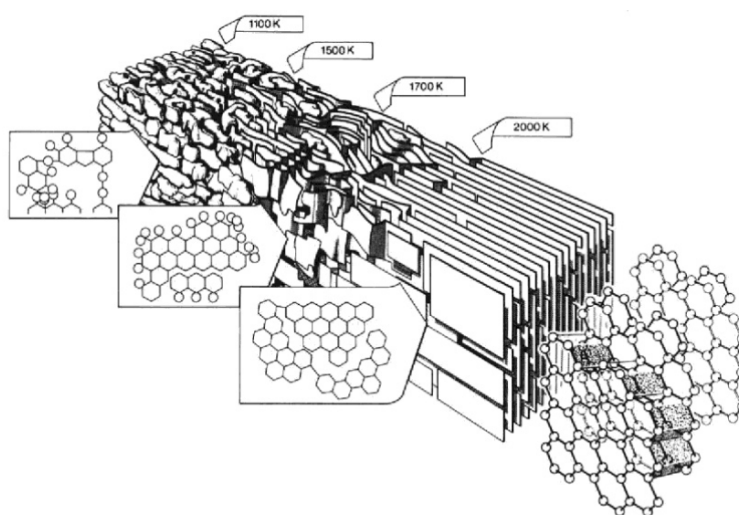


Figure 2.6: Structural development in carbonaceous materials during heat treatment up to the formation of a graphite lattice. Reproduced with permission from reference [159].

Mostly amorphous carbon gradually forms more aromatic structures and graphite-like layers with increasing temperature. These layers merge to growing crystallites, the aforementioned processes coming into action

with further increasing temperature. In this way amorphous structures are transformed into turbostratic and then graphitic structures [2, 157]. Crystallite growth is the only mechanism of graphitization in microcrystalline carbonaceous materials. Thus, the crystallite size can be used as a measure for the state of the graphitization process. Crystallite growth involves one of two mass transport processes: Either the movement and merging of layers or atomic diffusion lead to increased crystallite sizes [160]. With increasing layer size, the energy necessary for translation is increased so that crystallite growth is only possible to a certain limit at a specific temperature.

In addition to the temperature, pressure can play a role in the graphitization process. Noda *et al.* achieved a lattice spacing of 0,672 nm after heat treatment of glassy carbon, a typical non-graphitizing carbon, at 2600 °C and 10 kbar [161]. This is significantly lower than the lattice spacing of 0,681 nm reported at 3000 °C and atmospheric pressure. Furthermore, they demonstrated that the temperature at which polyvinylchloride coke and petroleum coke become graphitized could be lowered by 1000 °C by applying a pressure of 10 kbar during the graphitization process. It was also shown, that pressures below 1 atm retards graphitization for calcined petroleum coke [162]. Furthermore, introducing additional matter to the process will influence the graphitization of the carbonaceous material. Oxidizing gases like carbon dioxide and oxygen can increase the degree of graphitization [163, 164] while sulfur atoms may reduce the graphitizability [165]. Using transition metals such as aluminum [166, 167], iron [166, 168–170], copper [167, 171], chromium [166, 171], cobalt [167, 170], and nickel [166, 167, 170] significantly decreases the temperature needed for the graphitization of carbonaceous materials. The mechanism of catalytic graphitization involves the dissolution of amorphous carbon into the catalyst particle and subsequent precipitation of graphitic carbon due to supersaturation [171, 172]. This process only takes place in the immediate vicinity of the catalyst particle with the metal acting as transporting medium leading to graphitization on the metal's path [165]. The result is the formation of graphitic nanostructures within the material while maintaining amorphous or turbostratic structures in-between [172, 173]. In this way, highly crystalline but still porous materials could be obtained from different carbonaceous materials. Liu *et al.* used nickel to graphitize highly microporous biomass-derived activated carbon [173]. While larger highly graphitic domains were created with increasing temperature, the specific surface area decreased and the pore size distribution shifted to larger pores resulting in a mostly mesoporous material at 1000 °C. Catalytic graphitization was employed on templated mesoporous carbons by Sevilla *et al.* using nickel and iron [172]. While the untreated materials and the carbons heated without the addition of metals were completely amorphous showing no reflexes in XRD patterns, the catalytically graphitized carbons exhibited crystallite sizes obtained from XRD up to 9 nm. The previously unimodal pore size distribution develops into a bimodal distribution upon graphitization exhibiting large mesopores. Another possibility is the combination of chemical activation with catalytic graphitization as demonstrated by Zhai *et al.* using $ZnCl_2$ as activating agent and nickel and iron as graphitization catalysts [174]. Starting from mesophase pitch, mesoporous carbonaceous materials with crystallite sizes up to 5.4 nm were obtained at 900 °C. Although the lower energy consumption due to lower synthesis temperature of the catalytic process in comparison to the conventional method without catalysts is advantageous, there are some drawbacks. The catalyst has to be dispensed on the carbon precursors as evenly as possible before the heat treatment and residues of it have to

be removed via acid washing afterwards. Furthermore, heterogeneity of the carbonaceous materials resulting from the formed graphitic nanostructures may result in inferior mechanical, thermal and electrical properties compared to more homogeneous materials [171].

Vázquez-Santos *et al.* graphitized polymer-derived carbon fibers without a catalyst at temperatures between 900 and 2800 °C [175]. It could be shown that a gradual increase in structural order is achieved even in the lower temperature regime as evidenced by an increased crystallite size from 3.7 nm at 900 °C to 9.1 nm at 2000 °C. This means, that materials with increased crystallinity can be obtained in the temperature range between 1000 and 2000 °C without using graphitization catalysts. These materials have the advantage of being able to maintain porosity although the porous structures undergoes changes. An example for this is the work of Wiener *et al.* on the graphitization of porous carbons derived from phenolic resin [41]. In a temperature range between 800 to 2000 °C, the crystallite size of the carbonaceous materials obtained from XRD increases with increasing temperatures up to a maximum of 14 nm. At the same time, BET surface area and micropore volume are decreasing and the pore size is increasing. The result after heat treatment at 2000 °C is a mostly mesoporous carbonaceous material with an increased crystallinity. Similarly, Osswald *et al.* studied the vacuum annealing of TiC-CDC-600 between 1000 and 2000 °C [176]. Up to a temperature of 1500 °C, the surface area of the material increases, resulting in a porous and still amorphous carbonaceous material with subnanometer pore size and an SSA above 2000 m² g⁻¹. Above that temperature, the development of reflexes in XRD patterns can be observed as the crystallinity generally increases from that point on. Furthermore, the SSA is decreasing significantly while the average pore size increases drastically resulting in a mesoporous and more crystalline carbonaceous material after vacuum annealing at 2000 °C.

A number of studies focused on the heat treatment of activated carbons as broadly available commercial precursors. Most studies are limited to a single activated carbon as precursor and focus on a specific application. For the application as support material for platinum catalysts in the carbon monoxide oxidation, Kang *et al.* studied the heat treatment of one commercial activated carbon at temperatures of 1300, 1400, and 1500 °C [75]. A decrease in specific surface area and micropore volume, as well as an increase in mean pore size with increasing temperature was accompanied by an increase in structural order and increased stability under oxidizing conditions. Blazewicz *et al.* studied the heat treatment of another activated carbon in a broad temperature range (950 - 2100 °C), observing almost linearly decreasing micropore volume, constant mesopore volume, and the increased formation of turbostratic carbon up to 1800 °C [177]. At higher temperatures, the mesopore volume decreased as well and graphitic structures were formed. Kusmierk *et al.* were able to increase the adsorption rate for phenol of an activated carbon due to annealing under argon atmosphere at 1500 and 1800 °C [178]. Increased crystallinity in combination with decreased micropore volume and increased mesopore volume was found in the heat treated carbonaceous materials. An extended study containing a broad variety of different activated carbon precursors is missing in literature to this date.

2.3.2 Carbide-Derived Carbons: Influence of Synthesis Temperature on Crystallinity

In section 2.2.2, the influence of chlorination temperature and choice of carbide precursor on the resulting CDC's pore structure was discussed. The pore structure of carbonaceous materials is closely connected to its microstructure. Thus, the influence of synthesis parameters on the resulting microstructure in the chlorination process is of interest as well. Figure 2.7 summarizes experimental results from literature regarding the Raman intensity ratio I_D/I_G as a measure for the crystallinity of CDCs from different carbide precursors with respect to the chlorination temperature. Generally, the microporous CDCs obtained at temperatures below 1200 °C show rather amorphous structures with low structural order. With increasing synthesis temperature the Raman intensity ratio decreases. As the materials can be put in the first stage of the phenomenological three stage model proposed by Ferrari *et al.* [179], this hints towards an increase in structural order. Furthermore, for titanium carbide [17, 155] and boron carbide [154], remarkably high crystallinity could be shown with sharp reflections in X-ray powder diffraction measurements and interlayer spacings approaching the value of graphite. The increasing structural order coincides with the decreasing porosity discussed in section 2.2.2 in terms of synthesis temperature (microporous and amorphous at lower temperatures; mesoporous and crystalline at higher temperatures) as well as the unknown influence of the carbide precursor.

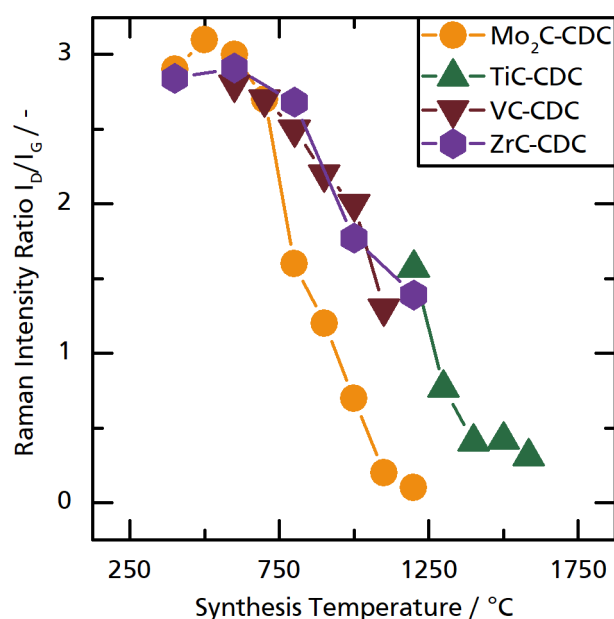


Figure 2.7: Influence of synthesis temperature on intensity ratio of Raman bands (I_D/I_G) for CDCs from Mo₂C [136], TiC [17], VC [140], and ZrC [142].

The increasing crystallinity at higher temperatures is known in literature and no unique feature of CDCs as heat treatments commonly increase the structural order of carbonaceous material (see previous section). As mentioned before, Osswald *et al.* found a visible increase of structural order and simultaneous decrease in SSA for carbide-derived carbons obtained from titanium carbide at 600 °C upon vacuum annealing starting at 1600 °C [176]. In contrast, Gläsel *et al.* found a comparable increase in crystallinity in TiC-CDCs starting

already at 1200 °C by synthesizing the material at that temperature instead of a post-treatment [17]. These 400 °C difference shows that the crystalline structures in these carbonaceous materials are formed during the chemical extraction of the metal atoms, hinting towards the carbide precursor as an important factor in this process. Consequently, several attempts were made to correlate their influence on the resulting carbon structure. For the three precursors niobium carbide, titanium carbide, and vanadium carbide, Xu *et al.* correlated an influence of the volumetric concentration of carbon atoms in the precursor carbide with the crystallinity of the resulting carbide-derived carbons obtained at 1000 °C [180, 181]. In contrast, Jeong *et al.* deduced for α -SiC and β -SiC an influence on the resulting microstructure of the respective CDC materials, although the two precursors show no difference in the volumetric concentration of carbon. Thus, to this date, it is not possible to predict when a mesoporous and crystalline CDC results from the chlorination of a specific carbide precursor. Therefore, it is necessary to understand how synthesis temperature and carbide precursor, the two major influencing factors, are coupled.

3 Objectives and Scope of the Study

Nowadays, porous carbonaceous materials are specialized materials that are often produced and adjusted to suit their respective applications. As shown in the previous chapter, few materials are available which combine a meso- and macroporous structure with a high crystallinity in order to provide an easily accessible but reasonable large surface area as well as thermooxidative and electrochemical stability. It is of great interest to develop such materials from a scalable synthesis route and to be able to tune their properties to fit different applications and purposes. In this work, two different approaches to synthesize mesoporous and crystalline carbonaceous materials are taken: thermal annealing of commercial activated carbons and chlorination of metal carbides. Although it is clear from literature that mesoporous and crystalline may be obtained via these approaches, an extensive understanding of the involved influencing factors is still missing for both. Thus, the influence of process parameters and their interactions on the resulting carbon microstructure and textural properties will be investigated in this work.

On the basis of one commercial activated carbon (*Darco KB-G*), the influence of argon pressure and annealing temperature in the range from 1000 to 1900 °C will be deduced by thoroughly characterizing the resulting annealed carbonaceous materials in regard to their carbon microstructure and textural properties. Furthermore, with the help of 25 additional commercial activated carbons, the influence of the activated carbon precursor will be investigated. For this, all activated carbons will be annealed at two temperatures (1000 °C, 1600 °C) and the resulting annealed carbons will be characterized via temperature-programmed oxidation as a fast screening method. Based on these results, some activated carbons will be selected to be annealed in the complete temperature range and characterized more thoroughly in order to be compared to *Darco KB-G*. This will show, if mesoporous and crystalline carbonaceous materials can be obtained from different abundantly available activated carbons and if it is possible to control their properties by adjusting annealing parameters and choice of precursor.

For carbide-derived carbons on the other hand, it is known from literature that the structural order increases with increasing chlorination temperature, but unfortunately, only a few studies go above synthesis temperatures of 1200 °C. The studies that did exceed these temperatures could show exemplary, that more crystalline CDCs with increased pore sizes could be obtained. Furthermore, it is known that the choice of carbide precursor affects the resulting CDC structure but no concrete correlation could be found yet. In order to augment the understanding of the coupling between these two major influencing factors, this work studies the conversion of six different carbide precursors to CDC via chlorination in the temperature range between 800 and 1600 °C.

A detailed characterization via X-ray powder diffraction, temperature-programmed oxidation (TPO), Raman spectroscopy, and argon physisorption will shed light on this correlation and further improve the possibilities to employ CDCs for numerous applications.

Based on the findings about the carbon microstructure and textural properties of CDCs obtained from different carbide precursors in this temperature range, a number of carbons will be selected to act as support material for platinum catalysts. In order to exemplarily show the viability of the prepared CDCs in electrochemical applications, these catalysts will be characterized via inductively coupled plasma optical emission spectrometry (ICP-OES), XRD, and cyclic voltammetry and their stability will be tested via accelerated durability test (ADT) procedures. This will help to deduce the influence of the carbon support structure on the catalysts' properties and stability. Furthermore, thermal presintering will be applied to selected catalysts in order to improve the stability of the catalysts and understand how the carbon support will influence the sintering process. Eventually, the catalysts selected for presintering, pristine and sintered, will be tested in the oxygen reduction reaction (ORR) to obtain first impressions of their activity and how it is influenced by sintering process and carbon support structure.

4 Experimental Section

4.1 Carbonaceous Material Synthesis

4.1.1 Annealing of Activated Carbons

The synthesis of carbonaceous materials via annealing of activated carbons took place in the graphite vacuum furnace *CAF 140/140-2000G* (*MUT Advanced Heating GmbH*) under a pressure of 16 mbar unless noted differently. In order to prevent fouling on the glass windows in front of the two pyrometers necessary for temperature control, a steady argon gas flow of 2 L min^{-1} was applied. For a typical vacuum annealing, three activated carbon samples of 500 mg each were placed into the bores of a graphite sample holder with a lid and loaded into the furnace. After an inertization program, where the furnace chamber was evacuated to 2 mbar by a membrane pump, tested for leakages, flushed with argon and evacuated again, the furnace was heated to 200°C . This temperature was held for 2 h in order to remove any humidity from the samples and the furnace chamber. Subsequently, the furnace was heated to the target temperature which was held for 90 min before cooling down. Heating and cooling were conducted at maximum rates depending on the respective temperature regimes listed in table 4.1. Finally, after reaching a temperature of 100°C and flushing the furnace chamber with argon, the annealed carbon could be unloaded.

Table 4.1: Maximum heating (left) and cooling (right) rates for the vacuum furnace with respect to the relevant temperature regimes.

Temperature Regime / $^\circ\text{C}$	Rate / K min^{-1}	Temperature Regime / $^\circ\text{C}$	Rate / K min^{-1}
20 - 1200	20	1900 - 1000	20
1200 - 1500	15	1000 - 500	10
1500 - 1700	10	500 - 20	5
1700 - 1900	5		

4.1.2 Chlorination of Metal Carbides

The synthesis of carbide-derived carbons via chlorination of metal carbides took place in a tubular horizontal reactor. The whole setup necessary for the reaction is depicted simplified in figure 4.1. Basically, it can be divided into three modules, highlighted by different colors. They will be discussed subsequently from left to right following the gas flow during the reaction.

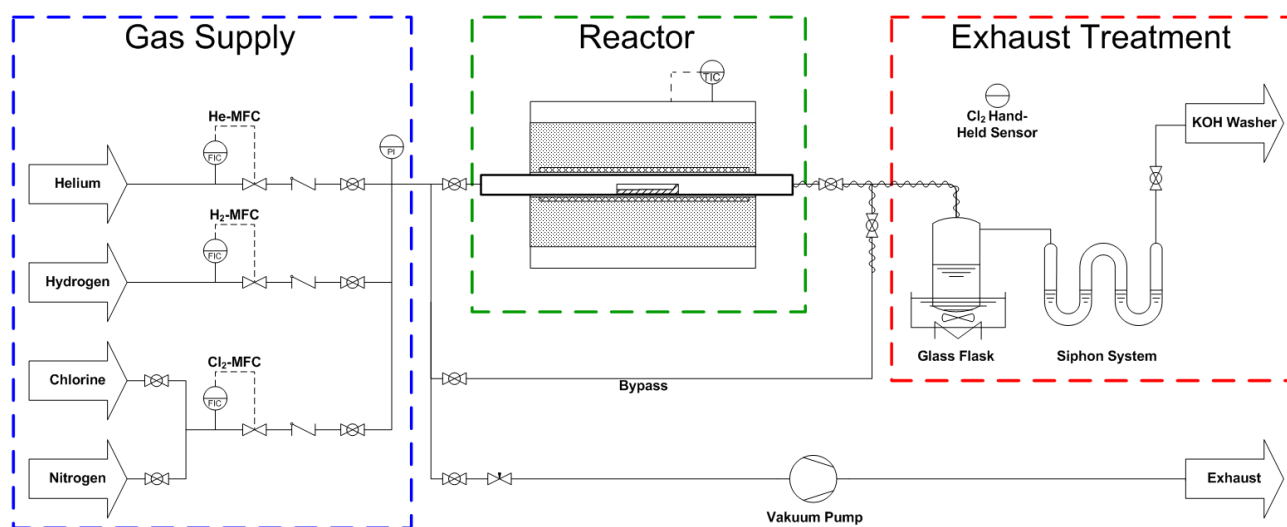


Figure 4.1: Schematic depiction of the experimental chlorination setup. The system is divided into the three modules 'Gas Supply', 'Reactor', and 'Exhaust Treatment', highlighted by boxes in blue, green, and red, respectively.

The first module (blue) is the gas supply, which includes helium, hydrogen, and nitrogen from gas bottles and chlorine from a liquid gas bottle. Helium and hydrogen gas flows go directly into the reactor system and can be controlled via mass flow controllers (MFC) of type *EL-FLOW* (*Bronkhorst*). Chlorine has to pass a separate gas panel before going into the reactor system and the flow can be controlled via mass flow controller of type *LOW- Δp -FLOW* (*Bronkhorst*). The gas panel makes it possible with valves to shut down chlorine and flush the system with nitrogen for maintenance without interfering with other chlorine experiments on the same gas line.

The next module is the reactor itself (green), being an alumina tube (*Degussit AL 23, Friatec*) with a diameter of 33 mm and a length of 1500 mm. The tube is fitted with stainless steel flanges cooled with an ethylene glycol water mixture to connect the reactor with the surrounding gas system via vacuum flanges (DN 40) with viton o-ring seals. A 0.5 mm graphite foil (*Sigraflex, SGL*) lines the inner tube wall in order to protect the alumina during the chlorination. The reactor is placed into a high temperature furnace of type *HTRH100-600/18* (*Carbolite Gero*). MoSi_2 heaters enable the furnace to reach temperatures up to 1600 °C with a maximum heat rate of 200 K h^{-1} . For safety reasons, a bypass system is installed to avoid the reactor in case of a blockage or other issues. Furthermore, the whole reaction setup is connected to a vacuum pump to remove air out of the system before reactions and to find leakages.

In the final module (red), the exhaust gases of the reactor are treated in order to be safely dismissed into the exhaust system of the building. In a first step, metal chlorides react with steam in a two neck flask (heated to 80 °C) to the respective metal oxides and hydrogen chloride. The gas line connecting reactor and two neck flask is a metal braided flexible tube with a core of PTFE and is heated to 130 °C to prevent condensing of reaction products and subsequent clogging of the tubing. The two neck flask is followed by a siphon system

filled with 20 wt-% of KOH which neutralizes formed HCl and residual chlorine. Before going into the exhaust system, the exhaust gases finally pass a 80 L KOH washer (*CSV/Q2.5-2/1DE, AIRTEC*) to ensure the complete chlorine removal.

For the chlorination of a particular carbide, the precursor was loaded into a graphite crucible, which was then placed into the middle of the alumina tube. After closing the flanges, the reaction system was evacuated to exclude any air from the reactor and to check the system for leakages. If the pressure could be held for at least 30 min, the reactor was flushed with helium. Experiments were conducted at 800 - 1600 °C, reached with a heating rate of 200 K h⁻¹. Throughout the experiment, a superficial velocity of 0.03 m s⁻¹ was ensured for the total gas flow. The chlorine concentration was 0.5 mol m⁻³ at the start and was raised up to 2.0 mol m⁻³ throughout the reaction. After chlorination, the resulting CDC was post-treated with 1.0 mol m⁻³ hydrogen in helium. The annealing was carried out at reaction temperature, except when the reaction temperature was above 1400 °C, then the reactor was cooled down to 1400 °C before the treatment. Afterwards, the reactor was cooled down to room temperature under helium flow with a rate of 200 K h⁻¹.

The nomenclature of the CDCs in this work consists of the precursor (i.e. TiC) and the reaction temperature in degree Celsius (i.e. 1400), connected by 'CDC'. For example, 'TiC-CDC-1400' is a CDC from titanium carbide, chlorinated at 1400 °C.

4.2 Material Characterization

X-Ray Powder Diffraction

X-Ray powder diffractograms of activated carbons before and after the annealing process were obtained in a *STADI P* diffractometer (*Stoe & Cie GmbH*) with a *Mythen1K* detector (*Dectris*). The samples were filled into capillaries with diameters of 0.5 mm and measured in Debye-Scherrer geometry using Ge[111]-filtered $\text{Cu}_{K\alpha 1}$ radiation ($\lambda = 1.54060 \text{ \AA}$).

XRD patterns of CDCs were recorded by a *Phaser D2* (*Bruker*) operated at 30.0 kV and 10.0 mA using $\text{Cu}_{K\alpha 1}$ radiation ($\lambda = 1.54060 \text{ \AA}$). The samples were analyzed with a *Lynxeye XE 1D* detector (*Bruker*) in rotating silicon crucibles (10 rpm) in a range of 10 to 80° , with a step size of 0.016° , and an acquisition time of 1 s per step.

In order to evaluate the diffractograms of carbonaceous materials, a fitting procedure was applied after baseline correction of the patterns. The (002) reflex was fitted with two Voigt functions, the reflexes (100) and (101) were fitted with a total of three Voigt function. An example for the fitting procedure can be seen in figure 4.2 for TiC-CDC-1400.

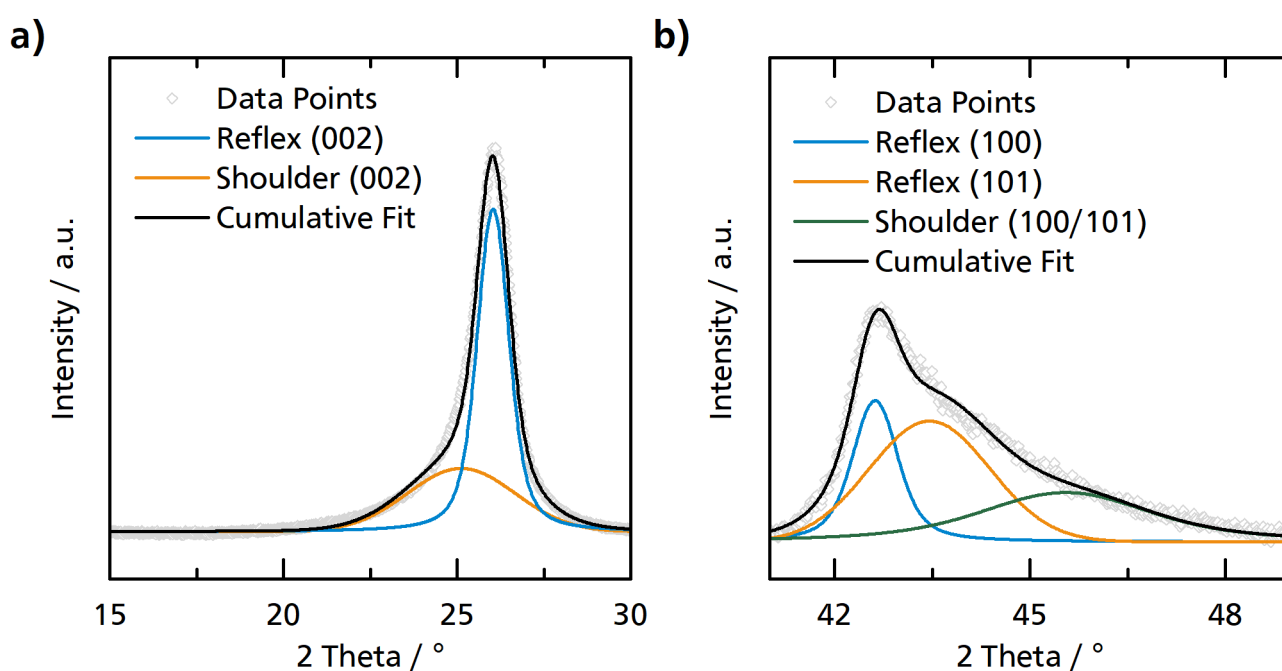


Figure 4.2: Fitting procedure for X-Ray diffractograms of carbonaceous materials. The exemplary sample is TiC-CDC-1400. **a)** Fitting of reflex (002) using two Voigt functions, **b)** fitting of reflexes (100) and (101) using three Voigt functions.

For platinum particles on carbonaceous materials, one Voigt function is used to fit the (220) reflex as can be seen exemplary for Pt/TiC-CDC-1400 in figure 4.3. The fit was deemed adequate, if the coefficient of determination (R^2) was 80% or higher.

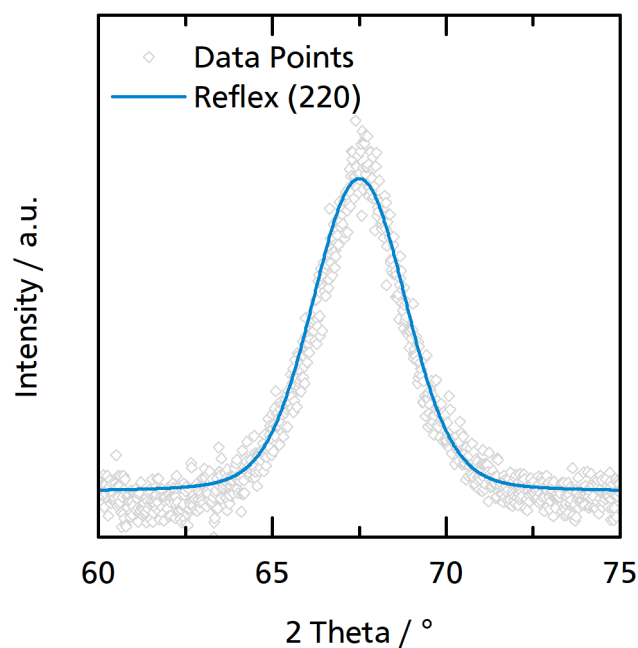


Figure 4.3: Fitting procedure of X-Ray diffractograms for platinum particles on carbon support. The (220) reflex of the exemplary sample (20 wt% Pt on TiC-CDC-1400) is fitted by using one Voigt function.

The crystallite size of graphitized carbon domains in the 100 lattice plane L_a (along the a axis) and in the 002 lattice plane L_c (along the c axis), as well as the average platinum particle size L_{Pt} can be calculated from the (100), (002), and (220) reflexes, respectively, using the Debye-Scherrer equation [182, 183]:

$$L_{a/c/Pt} = \frac{K_{a/c/Pt} \cdot \lambda}{\beta \cdot \cos\theta} \quad (4.1)$$

Where β is the full width at half maximum and θ the position of the respective reflex. $K_{a/c/Pt}$ is the Scherrer constant with values of 1.84 (K_a) [175], 0.91 (K_c) [136], and 0.90 (K_{Pt}) [184].

Raman Spectroscopy

Raman measurements were carried out with a *Senterra XY* Raman micro spectrometer (*Bruker*) using an Nd:YAG laser with a wavelength of 532 nm and a maximum power of 50 mW. For every sample, spectra were collected on twelve spots on the surface with a diameter of 2 μm , magnified with a 50x object lens. Other parameters for the measurements were a resolution of 9 to 15 cm^{-1} , 2 s integration time, an aperture of 50x1000, 30 coadditions and a laser power of 0.5 mW. The selected measurement conditions ensured the collection of Raman spectra with high resolution and good intensity without damaging the carbon surface.

Literature offers a multitude of combinations of different mathematical functions to fit Raman spectra of carbonaceous materials in order to evaluate them [179, 185]. Although the fitting procedure influences the resulting parameters, there is no conclusive reason to prefer a particular function [179]. The following fitting procedure for G and D band obtained good representations of the actual spectrum. A Breit-Wigner-Fano (BWF) function was used for the G band [185]:

$$I_G(\omega) = I_G \frac{\left(1 + \frac{\omega - \omega_G}{q\Gamma_G}\right)^2}{1 + \left(\frac{\omega - \omega_G}{\Gamma_G}\right)^2} \quad \omega_{\max} = \omega_0 + \frac{\Gamma}{2Q} \quad (4.2)$$

Its asymmetric shape should arise from the coupling of a discrete mode to a continuum [179]. The D band can be fitted by using two symmetric Voigt functions centered at the same position, which is related to the processes of single (D_1 , sharp) and double (D_2 , broad) scattering within the double resonance process [186]. The intensity of the D band is the sum of the D_1 and D_2 intensities. Together with another symmetric function for the D' band, this procedure involves four functions in total, as depicted in figure 4.4.

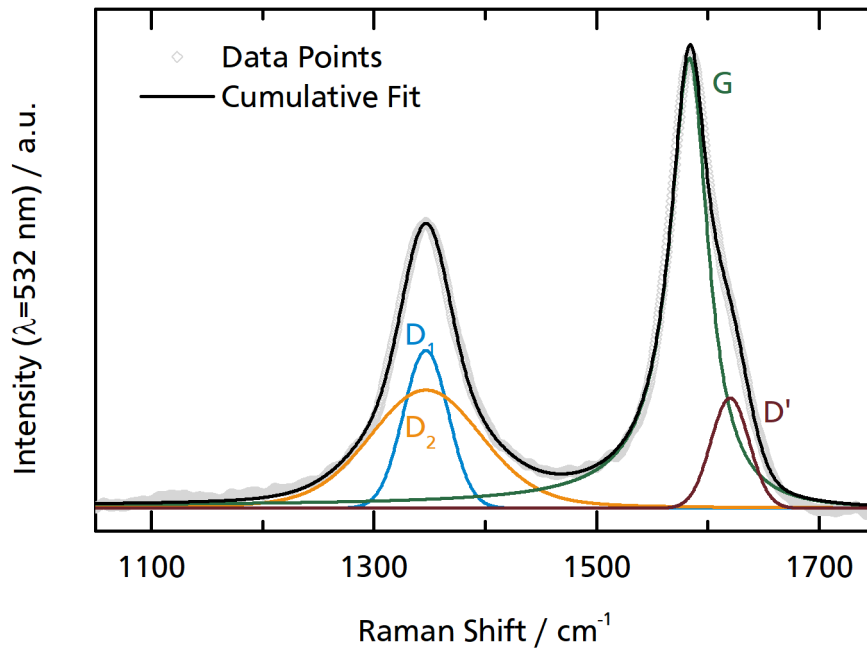


Figure 4.4: Fitting procedure for Raman spectra of carbonaceous materials. The exemplary sample TiC-CDC-1200 is fitted by using three Voigt functions (D_1 , D_2 , D') and one Breit-Wigner-Fano function (G). Shown are also the measured data points and the cumulative fit.

The correlation of Raman spectra characteristics to the mean in-plane size of the crystallites was the topic of numerous scientific studies in the past [179, 185, 187–192]. It could be shown, that effects of laser power, sample preparation, and detailed microstructure of different carbons can be expected to influence the results

of Raman spectroscopy. Furthermore, there seems to be the necessity to differentiate between crystallite regimes smaller and bigger than 10 nm. In this work, samples may lie just on the border of those regimes. Thus, intensity ratios of D and G band as well as the full width at half maximum (FWHM) of the G band are used to illustrate trends in the structural disorder of the examined carbonaceous materials.

Temperature-Programmed Oxidation

Temperature-programmed oxidation was investigated with 20 mg of the sample in a Al_2O_3 crucible using the thermogravimetric balance *STA 449 C (Netzsch)*. After drying in the balance for 20 minutes at 50 °C, the sample was heated to 1000 °C with a rate of 5 K min^{-1} . The temperature was held for 30 min before cooling down with a rate of 10 K min^{-1} . The whole measurement takes place under synthetic air atmosphere at ambient pressure. The materials are characterized by their onset of oxidation determined via the software *Proteus Thermal Analysis (Netzsch)* in conformation with DIN 51007.

Physisorption

Textural properties of activated carbons before and after the annealing process were studied via nitrogen physisorption analysis at -196 °C using a *Quadrasorb evo (Quantachrome)*. The samples were outgassed under vacuum at 350 °C for 18 hours. Subsequently, 25 points and 16 points were recorded for the adsorption and desorption branch, respectively.

Argon physisorption at -189.3 °C was conducted on a *3Flex analyzer (Micromeritics)* in order to study the textural properties of CDCs. After degassing of the samples under vacuum at 350 °C for 18 hours, adsorption (70 points) and desorption (40 points) branches were recorded.

Evaluation of the isotherms was realized with the software *VersaWin (Quantachrome)* using the Brunauer-Emmett-Teller multipoint method. Carbide-derived carbons synthesized at high temperatures exhibit a unique chemical surface structure and an unknown pore geometry. Furthermore, the materials range from microporous to mesoporous pore structure, enhancing the challenge of finding an appropriate evaluation method. Nevertheless, it is preferred to use a single method in order to follow the transition of the carbon structure seamlessly. Thus, the textural properties will be discussed only with the help of the specific surface area and the total pore volume in addition to the isotherms. In a previous publication, my coworkers and I were able to show, that this approach can be applied to describe trends in these kind of materials [93].

Inductively Coupled Plasma Optical Emission Spectrometry

The accurate platinum loading of catalysts used in this work were obtained via inductively coupled plasma optical emission spectrometry. Before the measurement, a chemical digestion had to be performed. For this, 5 mg catalyst were weighted out into a glass crucible, which was subsequently heated to 700 °C for 3 h to burn off all carbon. The remaining material was dissolved in *aqua regia* ($\text{HCl}:\text{HNO}_3$ 3:1) and then diluted to

50 mL with water. The measurement itself was conducted via contract measurement in a *ICP-OES Optima 2000DV (Perkin Elmer)* at the Center for Structural Materials in Darmstadt.

4.3 Electrochemical Performance Testing

4.3.1 Preparation of the Platinum Loaded Catalyst

Before the actual catalyst preparation, CDC particle sizes were reduced by wet milling to prevent an increased mass transport resistance through the catalyst layer caused by thick catalyst films. For this, 500 mg of the CDC and 10 mL isopropanol were milled with ZrO_2 balls (3 mm, 100 g) in the planetary ball mill *PM100 (RETSCH GmbH)* for 1 h at 450 rpm. To prevent heating of the material, the milling was conducted at intervals of 10 min with breaks of 5 min in-between. The milled carbon was dried at 50 °C.

The electrochemical catalysts were prepared via incipient wetness impregnation of hexachloroplatinic acid ($H_2PtCl_6 \cdot xH_2O$, HPA) solution in ethanol and subsequent gas phase reduction. Typically, the exact amount of HPA required for a target loading of 20 wt-% platinum was dissolved in the exact volume of ethanol corresponding to the pore volume of the respective carbide-derived carbon (obtained via argon physisorption, see section 4.2). The solution was then mixed with the CDC in an alumina crucible until the mixture was visibly dry. Afterwards, the crucible was transferred to a tubular horizontal furnace for drying and reduction. Initially, the furnace was heated under nitrogen gas flow to 100 °C ($150 K h^{-1}$) and held there for 1 h to remove the ethanol from the CDC's pores. Subsequently, the sample was heated to 250 °C ($150 K h^{-1}$) and kept at this temperature for 3 h. This reduction step was carried out with constant gas flow of 30 vol-% hydrogen in nitrogen. In the end, the furnace was cooled down under nitrogen gas flow.

Sintering of selected catalysts was conducted in an alumina crucible placed in a tubular horizontal furnace. Under nitrogen gas flow, the furnace was heated to the desired sintering temperature with a rate of $300 K h^{-1}$. The temperature was held for 2 h before cooling down to room temperature. In order to ensure the comparability of the sintered materials, one batch of catalyst was used for a complete sintering series. Due to the limited availability of the material, the sintering was conducted step wise. This means that approx. 50 mg of each catalyst was initially sintered at 400 °C, samples for electrochemical and structural characterization were taken, and the remaining catalyst was used for the next sintering step. This procedure was continued with temperature steps of 100 °C until the highest sintering temperature of 900 °C was reached.

The nomenclature of the catalysts in this work uses the prefix 'Pt' to indicate the presence of platinum particles. Furthermore, the carbide precursor and the chlorination temperature is specified. Sintered catalysts can be identified by the addition of 'T' and the sintering temperature in degree Celsius divided by 100. For example 'Pt/TiC-1300_T5' is a catalyst with platinum particles on a TiC-CDC-1300 support, which was sintered at 500 °C.

4.3.2 Three Electrode Setup

The three-electrode electrochemical cell is an established method to predict performance trends of electrochemical catalysts in membrane electrode assemblies of fuel cells [193]. The setup used a calibrated Ag/AgCl

electrode as the reference electrode (RE) and platinum for the counter electrode (CE). The working electrode (WE) was a glassy carbon electrode with 5 mm diameter and 0.196 cm² geometric surface area. 0.1 M HClO₄ in ultrapure water was the electrolyte for all methods carried out. The setup was run using the instrument *Ivium-n-Stat* (*Ivium Technologies B.V.*) and the software *IviumSoft*.

In order to deposit the catalyst on the working electrode, a catalyst ink was prepared and applied. For this, 3.0 mg catalyst were dispersed in a mixture of 1.5 mL isopropanol and 0.09 mL nafion solution (5 wt-% in isopropanol). The ink was homogenized via ultrasonic treatment. Before application of the ink, the working electrode was cleaned with acetone, ethanol, and water, subsequently. Afterwards, 10 μL of the fresh ink was applied to the WE by a micro pipette to achieve a target loading of 19.2 μg cm⁻² platinum. The working electrode was dried under argon gas flow. This preparation led to acceptable but not optimal catalyst films on the working electrode. In detail, the films looked uniform over the entire surface with small differences in thickness on the edges or in the center, equivalent to the 'intermediate film' described by Garsany *et al.* [194]. This type of film is a compromise accounting for the highly different carbon microstructures in the examined carbonaceous support materials. Optimizing the ink for one group of materials always led to a significant worsening of the film for other groups. Thus, a deposition method was chosen which could be applied to all examined support materials and which yielded a comparable film quality for all.

Cyclic Voltammetry

Cyclic voltammetry was carried out in order to evaluate the electrochemical surface area (ECSA) and the double layer capacitance (DLC). Before starting the measurements, the electrolyte was saturated with nitrogen and a constant nitrogen gas flow was applied during the measurements. Furthermore, the working electrode was cleaned electrochemically via potential cycling between 0.06 V and 1.2 V versus RHE (reversible hydrogen electrode) at 500 mV s⁻¹ for 200 cycles. Afterwards, the cyclic voltammetry itself was recorded from 0.06 V to 1.2 V versus RHE with a scanning rate of 20 mV s⁻¹. The sample was cycled five times and the fifth cycle was used for evaluation.

The recorded cyclic voltammograms (CVs) had to be corrected for double-layer charging by subtracting the current at 0.40 V from the total current. Then, the hydrogen adsorption charge $Q_{\text{H-ad}}$ could be extracted by integrating the negative-going potential scan in the range of 0.400 V to 0.075 V. The Pt electrochemical surface area was calculated from $Q_{\text{H-ad}}$ using equation (4.3) with Q_{H} being the charge of full coverage for clean polycrystalline Pt (210 μC cm⁻²). Furthermore, it was normalized to the platinum mass m_{Pt} [194].

$$ECSA = \frac{Q_{\text{H-ad}}}{Q_{\text{H}} \cdot m_{\text{Pt}}} \quad (4.3)$$

The double layer capacitance acts as a measure for the total surface area accessible to the solvent and can be calculated from equation (4.4). The double layer current I_d can be taken from the current difference between

the cathodic and the anodic sweep at 0.40 V. Taking into account the scan rate ν and normalizing to the catalyst mass m gives the double layer capacitance:

$$DLC = \frac{I_d}{2\nu \cdot m} \quad (4.4)$$

Oxygen Reduction Reaction

Rotating disk electrode (RDE) measurements were performed in order to investigate the catalyst activity in the oxygen reduction reaction. Initially, the background current was measured under nitrogen with a rotation of 1600 rpm from 0.06 V to 1.06 V versus RHE (20 mV s^{-1}). After saturating the electrolyte with oxygen, the sample was cycled three times under the same condition and the third cycle was used for evaluation.

Baseline correction was carried out by subtracting the recorded voltammogram under nitrogen conditions from the ORR polarization curve with oxygen saturation. To ensure the comparability between catalysts, the mass-transport correction (equation (4.5)) was used to calculate the kinetic current I_{kin} . The diffusion limited current I_{diff} is defined as the average current in the potential range 0.2 V to 0.5 V and $I(0.90)$ is the current at $E = 0.90 \text{ V}$. The platinum mass specific activity (MSA) of the catalyst was then calculated from I_{kin} by normalization to the platinum loading of the working electrode [194].

$$I_{\text{kin}} = \frac{I_{\text{diff}} \cdot I(0.90)}{I_{\text{diff}} - I(0.90)} \quad (4.5)$$

Accelerated Durability Test

The catalyst stability was examined via two accelerated durability test procedures, where the catalysts were cycled in a given potential range to provoke deactivation. The procedure for milder condition included 5000 cycles in the range from 0.6 V to 1.1 V, the one in the harsher conditions 3000 cycles in the range from 0.6 V to 1.4 V. In-between the cycling, a total of 5 CVs were recorded and in the end another ORR polarization curve was taken. With this, the changes of the catalyst's ECSA, DLC and activity during the process could be monitored. They are represented as the ratio of the value after and before the ADT, labeled as 'relative' ECSA, DLC, or MSA.

5 Results and Discussion

5.1 Activated Carbon as Precursor for Mesoporous and Crystalline Carbons

5.1.1 Influence of Annealing Parameters for Darco KB-G as Exemplary Activated Carbon

In this section, the influence of annealing temperature, argon pressure, and activated carbon precursor during the annealing process under nonoxidative conditions on the resulting carbon structure is discussed. Furthermore, the possibilities to tune the properties of activated carbons in order to satisfy the demands of specific applications are investigated. The powdered activated carbon *Darco KB-G* is used as an exemplary activated carbon precursor in order to deduce the influence of annealing temperature and argon pressure. The material is made from wood and activated with phosphoric acid. It is mostly used in the adsorption of high molecular weight organics due to its high adsorptive capacity and good filtration characteristics [195]. The annealing temperature was varied between 1000 and 1900 °C in steps of 100 °C. For the pressure variation, experiments at atmospheric pressure (labeled 'atm') were conducted in addition to the standard procedure at 16 mbar (labeled 'VA'). To begin with, the carbon microstructure of the materials will be discussed in the following by applying temperature-programmed oxidation, Raman spectroscopy, and X-ray powder diffraction measurements. Subsequently, a detailed review of the textural properties will be given on the basis of nitrogen physisorption measurements.

Carbon Microstructure

Mass loss curves from the temperature-programmed oxidation of *Darco KB-G* and selected annealed materials are shown in figure 5.1a. All examined carbonaceous materials are stable up to certain individual temperatures, but quickly oxidize above these temperatures. In contrast to the annealed carbons, the precursor shows a small increase in mass at around 300 °C before the mass loss starts. This indicates surface groups which could be oxidized and thus increase the carbonaceous material's mass. Due to the high temperatures during annealing, these surface groups are gone in the annealed materials leaving a nonfunctionalized carbon surface. Furthermore, *Darco KB-G* exhibits some ash content which could not be burned in the TPO, indicated by the remaining mass in the mass loss curve (7 wt-%), which cannot be seen for the annealed materials. Most importantly, the mass loss curve is shifted to higher temperatures due to the annealing, where higher annealing temperatures led to more pronounced shifts. This can be quantified by using the onset temperature of oxidation, depicted in figure 5.1b. It clearly shows the huge step from the pristine material with an onset temperature of 388 °C to the annealed materials with onset temperatures above 540 °C. By increasing the

annealing temperature, the onset temperature increases up to a maximum of 596 °C. Thus, the oxidation stability of the materials was increased by the temperature treatment. Furthermore, this process seems to be independent of the argon pressure as the onset temperature of the materials obtained at atmospheric pressure and the ones obtained under vacuum are decidedly similar.

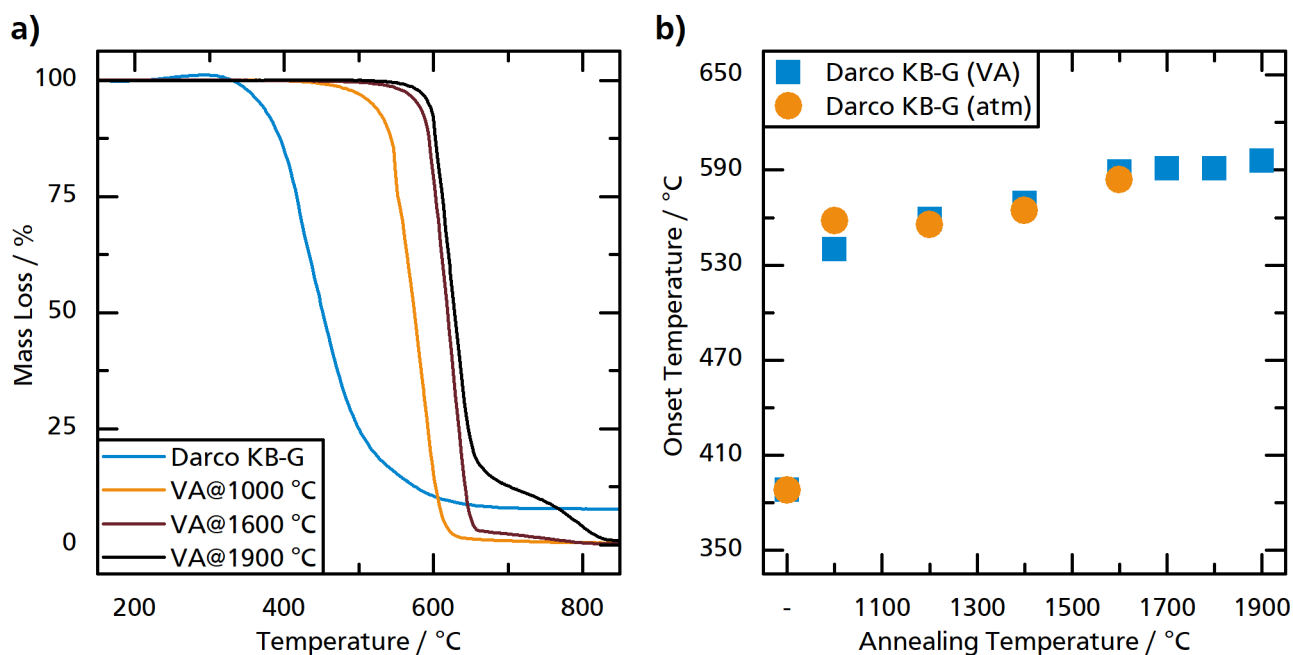


Figure 5.1: **a)** Mass loss curves from temperature-programmed oxidation of *Darco KB-G* before and after vacuum annealing at different temperatures. **b)** Oxidation onset temperature of *Darco KB-G* before and after annealing at 16 mbar and atmospheric pressure.

Raman spectra of *Darco KB-G* and selected annealed materials are shown in figure 5.2. The characteristic carbon bands, the disorder-induced D band around 1360 cm^{-1} and the graphitic G band around 1580 cm^{-1} , can be seen in all depicted spectra, although the D band is rather broad for the pristine activated carbon. The bands become more separated and both bands become narrower with increasing annealing temperature. Furthermore, the G band develops a shoulder towards higher wavenumbers at high annealing temperatures. All these developments hint towards an increased structural order with increasing annealing temperature [196]. The full width at half maximum of the G band (figure 5.2b), as well as the intensity ratio of the Raman bands I_D/I_G (figure 5.2c) give further indications towards increasing crystallinity. The FWHM is decreasing from 70 cm^{-1} at 1000 °C to 39 cm^{-1} at 1900 °C , the intensity ratio is increasing from 1.3 at 1000 °C to a maximum of 1.9 at 1400 °C and then decreasing to 1.2 at 1900 °C . Especially the evolution of the intensity ratio exactly fits into the phenomenological three-stage model proposed by Ferrari *et al.* [179, 197]: Below 1400 °C , sp^3 sites are converted to sp^2 sites (increasing I_D/I_G), while at higher temperatures, clustering of sp^2 sites takes place, forming graphitic domains (decreasing I_D/I_G). FWHM and intensity ratios from the materials obtained at atmospheric pressure match those of the materials obtained at 16 mbar, showing that the argon pressure does not play a role here.

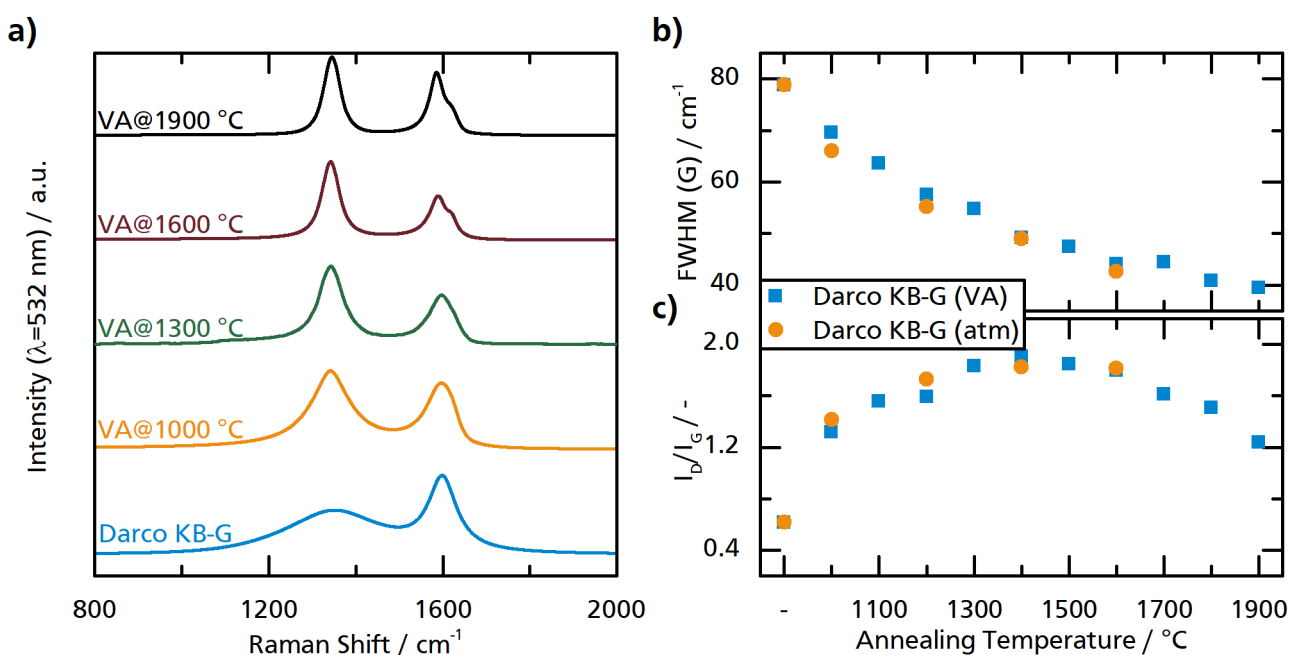


Figure 5.2: **a)** Raman spectra of *Darco KB-G* before and after vacuum annealing at different temperatures. **b)** Full width at half maximum of Raman G band (FWHM), and **c)** intensity ratio of Raman bands (I_D/I_G) of *Darco KB-G* before and after annealing at 16 mbar and atmospheric pressure.

Figure 5.3a shows powder diffraction patterns of the precursor *Darco KB-G*, and of the resulting materials from vacuum annealing at different temperatures. It can be seen that the activated carbon is completely amorphous as no distinct reflections can be seen in the pattern. The same can be said for the material that was annealed at 1000 °C. With increasing annealing temperature however, the characteristic carbon reflections, namely (002) at around 26° and (100/101) at around 43°, appear and become more distinct the higher the temperature. Nevertheless, the intensity of the reflexes do not indicate a highly crystalline material, but rather a mostly amorphous material with crystalline domains in it. The resulting in-plane crystallite sizes L_a and out-of-plane crystallite sizes L_c are depicted in figures 5.3b and c, respectively. Missing values in the figures indicate that the reflections of the respective materials are too unincisive to be evaluated accurately (see section 4.2 in the experimental section). L_a is increasing with increasing annealing temperature, while L_c shows a clear step from close to 0 nm at lower temperatures to above 30 nm at higher temperatures, with the transition taking place between 1300 and 1600 °C. Missing data points render it almost impossible to compare the crystalline sizes of materials annealed at 16 mbar with materials annealed at atmospheric pressure, but the shown crystallite sizes in figure 5.3 indicate congruent behavior.

All three characterization methods (TPO, XRD, Raman spectroscopy) show that the activated carbon precursor *Darco KB-G* is initially almost completely amorphous and thus prone to decomposition under oxidating conditions. With the help of a heat treatment at temperatures of at least 1000 °C, the crystallinity and with this the thermooxidative stability of the carbonaceous material, could be increased significantly. Increasing the annealing temperature leads to a further increase of the crystallinity, showing that the structural order could be

controlled via the choice of synthesis temperature. Furthermore, the applied characterization methods suggest that the argon pressure plays a neglectable role regarding the crystallinity of the obtained carbonaceous materials.

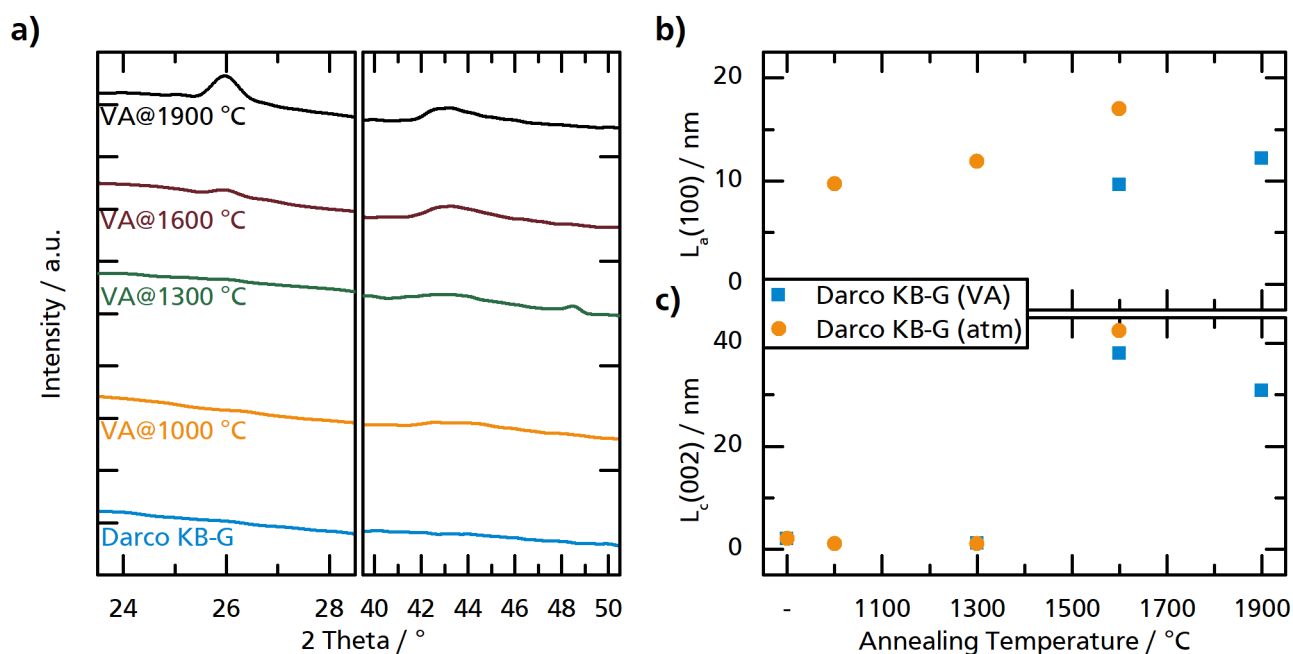


Figure 5.3: **a)** X-Ray powder diffraction patterns of *Darco KB-G* before and after vacuum annealing at different temperatures. **b)** Crystallite size $L_{a(100)}$ and **c)** Crystallite size $L_{c(002)}$ from x-ray powder diffraction measurements of *Darco KB-G* before and after annealing at 16 mbar and atmospheric pressure.

Textural Properties

Figure 5.4a illustrates the adsorption and desorption isotherms of *Darco KB-G* before and after vacuum annealing obtained from nitrogen physisorption. The materials exhibit isotherm hybrids of types I and IV with a little hysteresis. The untreated material has a high specific surface area of $1508 \text{ m}^2 \text{ g}^{-1}$, a pore volume of $1.17 \text{ cm}^3 \text{ g}^{-1}$, and an average pore diameter of 3.09 nm (see figure 5.5). The high knee of the adsorption branch indicates a high micropore volume. Upon vacuum annealing, the isotherm's knee is decreasing with increasing annealing temperature, indicating decreasing micropore volume. Furthermore, total pore volume and specific surface area are decreasing from $0.83 \text{ cm}^3 \text{ g}^{-1}$ and $1122 \text{ m}^2 \text{ g}^{-1}$ ($1000 \text{ }^\circ\text{C}$) down to $0.30 \text{ cm}^3 \text{ g}^{-1}$ and $169 \text{ m}^2 \text{ g}^{-1}$ ($1900 \text{ }^\circ\text{C}$), respectively. On the other hand, the average pore diameter is increasing from 2.94 nm up to 7.23 nm . This shows that the initially amorphous and highly porous material with a high micropore volume can be converted to a significantly more crystalline material with almost no porosity left by undergoing vacuum annealing at $1900 \text{ }^\circ\text{C}$. In this range, the carbon structure and textural properties can be tuned via the choice of annealing temperature.

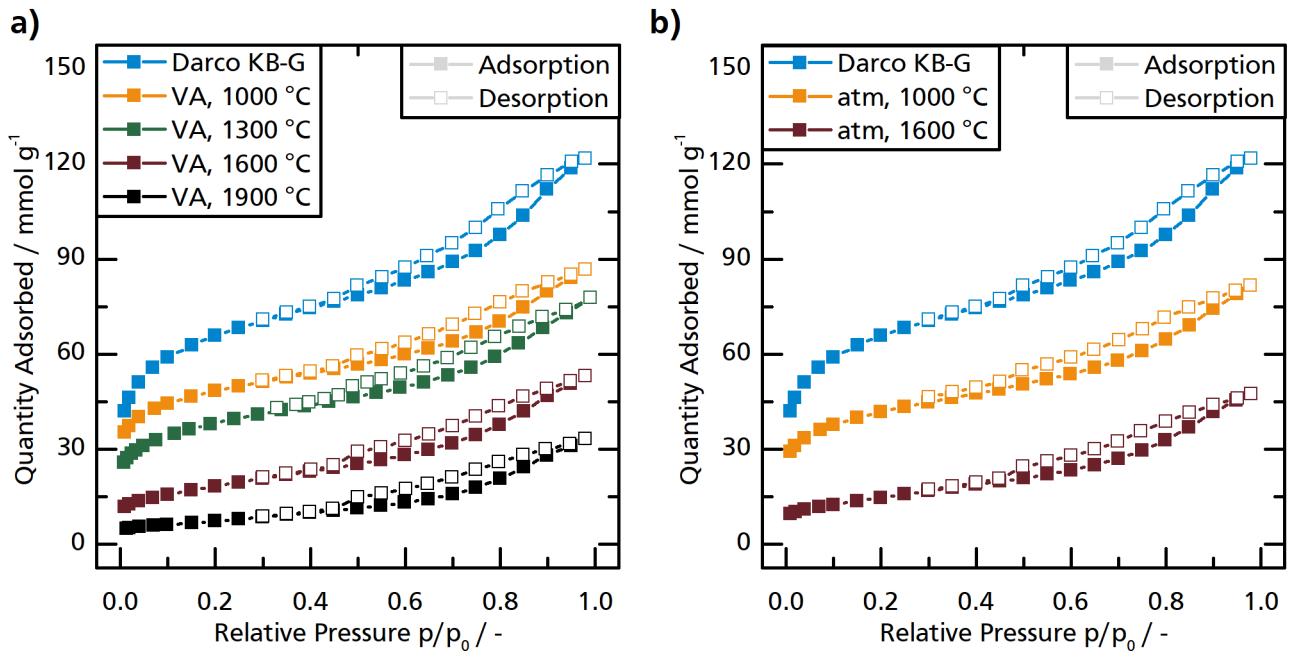


Figure 5.4: Adsorption / desorption isotherms from nitrogen physisorption of *Darco KB-G* before and after annealing at **a)** 16 mbar and **b)** atmospheric pressure.

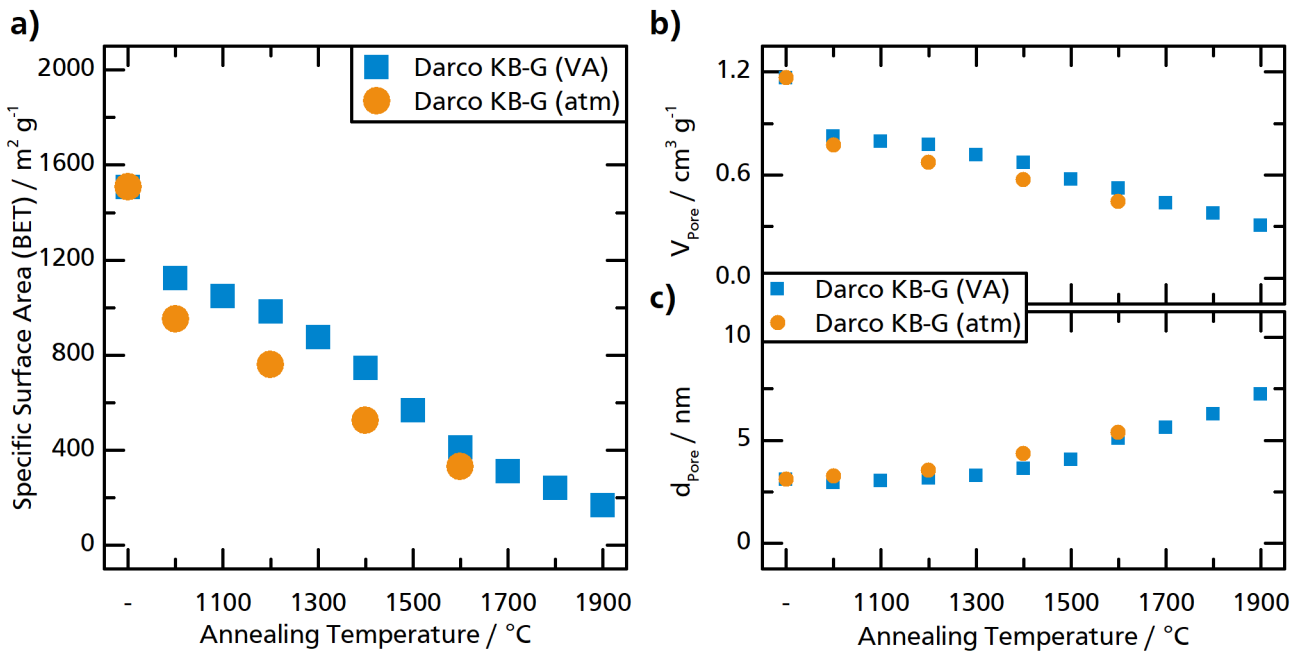


Figure 5.5: **a)** BET specific surface area, **b)** total pore volume, and **c)** average pore diameter from nitrogen physisorption of *Darco KB-G* before and after annealing at 16 mbar and atmospheric pressure.

Adsorption and desorption isotherms of *Darco KB-G* before and after annealing at atmospheric pressure can be seen in figure 5.4b. They are virtually congruent with the isotherms obtained from the corresponding vacuum annealed materials, exhibiting the same features. The specific surface areas are slightly lower for the materials obtained at atmospheric pressure, ranging from $951 \text{ m}^2 \text{ g}^{-1}$ (1000 °C) to $333 \text{ m}^2 \text{ g}^{-1}$ (1600 °C). Total pore volume and average pore diameter are very similar for both material types. Thus, the influence of argon pressure during the annealing process of activated carbon on the resulting material's structure can be seen as neglectable. Consequently, further experiments will only be conducted under the standard conditions of 16 mbar.

5.1.2 Influence of Activated Carbon Precursor

26 commercial activated carbons from seven different manufacturers were used to examine the influence of the activated carbon precursor on the resulting carbon structure after vacuum annealing. These carbons are produced from a variety of different feedstocks like wood or coconut via different activation methods (e.g. steam, phosphoric acid). Unfortunately, most manufacturers do not provide detailed information about the production process. Thus, no correlation of findings in this work to process parameters of the activated carbon precursor will be possible. A detailed characterization of the pristine materials via temperature programmed oxidation, Raman spectroscopy and nitrogen physisorption was necessary in order to find commonalities and differences in the variety of material. The results are shown in the following. For all of the discussed activated carbons, vacuum annealing experiments were conducted at 1000 and 1600 °C, respectively. Temperature programmed oxidation was then used as a quick characterization method, to provide insights into the resulting carbon microstructure. Based on this, a more detailed characterization will be provided for selected activated carbons and resulting annealed materials obtained at different temperatures.

Examined Activated Carbon Precursors

The broad variety of properties resulting from the detailed examination of the pristine activated carbons is summarized in table 5.1 and shows that the materials give an excellent basis for a study on the influence of the activated carbon precursor on the resulting carbonaceous materials after vacuum annealing. As expected, the carbon microstructure is mostly amorphous for all examined activated carbons, but nevertheless different states of structural order were found. This can be seen in the oxidation onset temperature, ranging from 352 °C (*Carbotech PAK A 1500 C*) to 520 °C (*Kuraray YP-50F*), the full width at half maximum of the Raman G band, ranging from 53 cm^{-1} (*Norit SX Plus*) to 79 cm^{-1} (*Darco KB-G*), and the Raman intensity ratio, ranging from 0.62 (*Darco KB-G*) to 0.35 (*Carbopal CCP 90*). High specific surface areas from $900 \text{ m}^2 \text{ g}^{-1}$ (*Norit SXRO*) up to more than $2300 \text{ m}^2 \text{ g}^{-1}$ (*Kuraray YP-80F*) and total pore volumes from $0.39 \text{ cm}^3 \text{ g}^{-1}$ (*Norit SXRO*) to $1.25 \text{ cm}^3 \text{ g}^{-1}$ (*Kuraray YP-80F*) show the generally high porosity with average pore diameters ranging from 1.68 nm (*Carbotech PAK C 1000 C*) to 3.27 nm (*Norit SX Ultra CAT*).

Table 5.1: Onset temperature from temperature-programmed oxidation, full width at half maximum of the Raman G band, Raman intensity ratio, as well as specific surface area, total pore volume, and average pore diameter from nitrogen physisorption for 26 commercial activated carbons.

Activated Carbon	T(Onset) /°C	FWHM(G) / cm ⁻¹	I _D /I _G / -	SSA / m ² g ⁻¹	V(Pore) / cm ³ g ⁻¹	d(Pore) / nm
AAA AQUA CP 2	392	60.7	1.31	1192	0.54	1.81
AAA AQUA CP 6/400F	394	57.8	1.26	1546	0.69	1.79
Carbopal CCP 1400 sp.	504	59.1	1.24	1502	0.65	1.74
Carbopal CCP 90	487	65.9	1.35	1068	0.46	1.71
Carbopal CCP 90 FF sp.	493	66.1	1.28	1060	0.46	1.72
Carbopal CCP 90 UF	501	66.8	1.22	1019	0.66	2.57
Carbopal SC 11 UF	514	64.2	1.26	1028	0.64	2.48
Darco KB-G	388	78.8	0.62	1508	1.20	3.17
Jacobi CP1	357	61.1	1.24	1222	0.58	1.89
Jacobi HS12x40	513	-	-	917	0.39	1.70
Jacobi JHS-500	465	57.6	1.29	1692	0.82	1.94
Jacobi SP-Pharma	502	60.8	1.25	1455	0.64	1.77
Kuraray YP-50F	520	59.6	1.16	1661	0.77	1.86
Kuraray YP-80F	510	50.1	1.32	2322	1.25	2.15
Norit A Supra	518	59.6	1.27	1845	0.89	1.93
Norit A Supra EUR	517	57.2	1.32	1677	0.82	1.96
Norit SXRO	477	65.3	1.15	897	0.39	1.73
Norit SX Plus	508	52.9	1.10	979	0.79	3.23
Norit SX Ultra CAT	499	58.3	1.18	957	0.78	3.27
PAK A 1500 C	352	59.2	1.23	1526	0.71	1.86
PAK A 1500 C AR	434	56.8	1.13	1486	0.76	2.05
PAK C 1000 C	404	63.8	1.22	1176	0.49	1.68
PAK C 1000 C AR	516	64.1	1.19	1111	0.47	1.70
Silcarbon CW 20	418	73.1	0.82	1419	1.14	3.22
Silcarbon TH90I	378	64.8	1.17	1239	0.57	1.85
Silcarbon TH90spezial	422	77.0	0.82	1265	1.02	3.23

Onset temperatures from temperature-programmed oxidation of all examined activated carbons and the resulting annealed materials obtained at 1000 and 1600 °C are depicted in figure 5.6. While onset temperatures of the pristine activated carbons lay in a broad temperature window of about 170 °C, onset temperatures of the vacuum annealed carbons are found in comparably small ranges of about 40 °C for each respective annealing temperature: materials annealed at 1000 °C range from 510 to 550 °C; materials annealed at 1600 °C range from 570 to 610 °C. An exception for this are carbons based on the precursor *PAK A 1500 C AR* with onset temperatures of 471 and 532 °C, respectively. In this context, the activated carbons can be divided into two distinct groups: materials from group 1 initially exhibit onset temperatures between 465 and 520 °C and only a marginal increase can be observed after vacuum annealing; activated carbons assigned to group 2 initially exhibit onset temperatures between 352 and 434 °C and a large increase can be observed upon vacuum annealing. The two groups cannot be told apart anymore after vacuum annealing at temperatures of at least

1000 °C as the onset temperatures of the resulting materials lay in a small range. No immediate correlation to any other examined property of the activated carbons was evident.

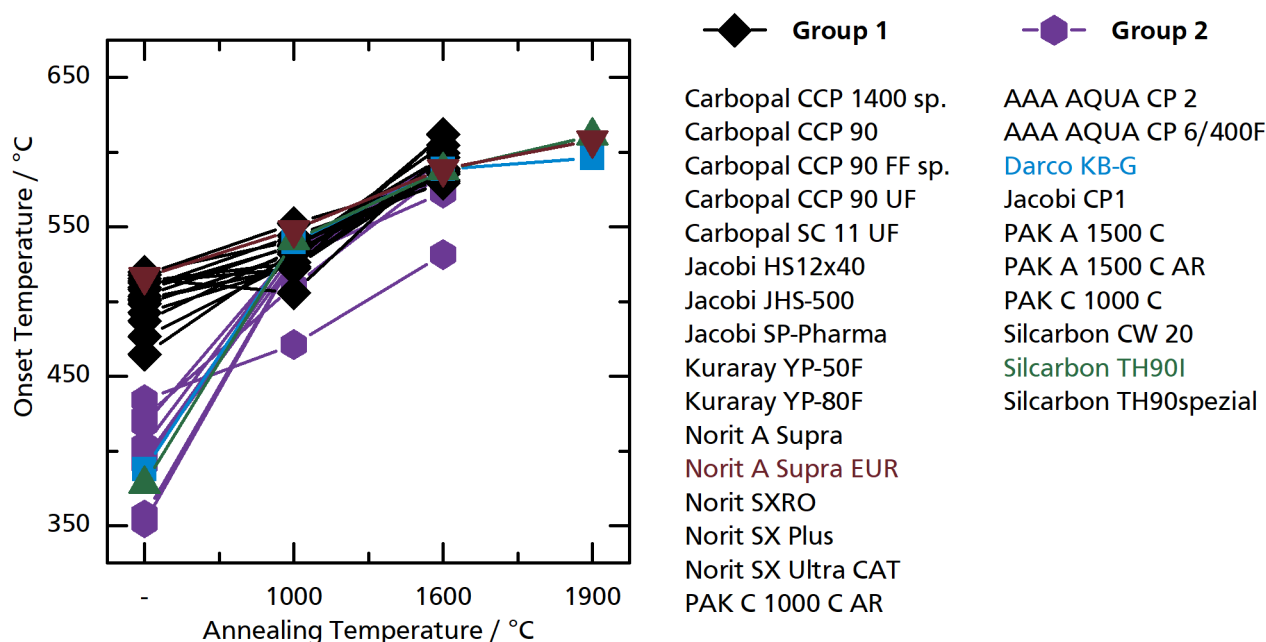


Figure 5.6: Onset temperatures from temperature-programmed oxidation of pristine activated carbons and the resulting carbonaceous materials after vacuum annealing at 1000, 1600, and 1900 °C. Commercial activated carbons are grouped regarding their onset temperatures before vacuum annealing.

Detailed Characterization of Selected Carbonaceous Materials

In addition to the heat treated carbonaceous materials obtained from *Darco KB-G*, materials from one precursor of each group were prepared via vacuum annealing in the range of 1000 to 1900 °C and characterized thoroughly in order to further investigate the influence of the activated carbon precursors. *Silcarbon TH90I* from group 2 is made from coconut whereas *Norit A Supra EUR* from group 1 is made from different renewable sources, both are activated with steam. The former is used for the removal of micro-pollutants, like chlorinated hydrocarbons, while the latter is used for the purification of pharmaceutical products and as antidote [195, 198]. In figure 5.6 it can be seen that the onset temperatures for the materials annealed at 1900 °C are slightly higher than those annealed at lower temperatures. With 596 °C (*Darco KB-G*), 608 °C (*Norit A Supra EUR*), and 611 °C (*Silcarbon TH90I*), the values are close to each other. Figure 5.7 summarizes the results from Raman spectroscopy of these materials. The same trend of increasing structural order with increasing annealing temperature can be seen for all three precursors in FWHM of the G band and I_D/I_G . Although the pristine activated carbons show different degrees of structural order in Raman spectroscopy with the FWHM of the G band ranging from 57.2 to 78.8 cm^{-1} and the intensity ratio ranging from 0.62 to 1.32, the values for the

annealed material are considerably more similar. In the case of the FWHM of the G band, 9.7 cm^{-1} at $1000 \text{ }^\circ\text{C}$ is the highest difference, while for the intensity ratio, 0.44 at $1700 \text{ }^\circ\text{C}$ is the largest deviation.

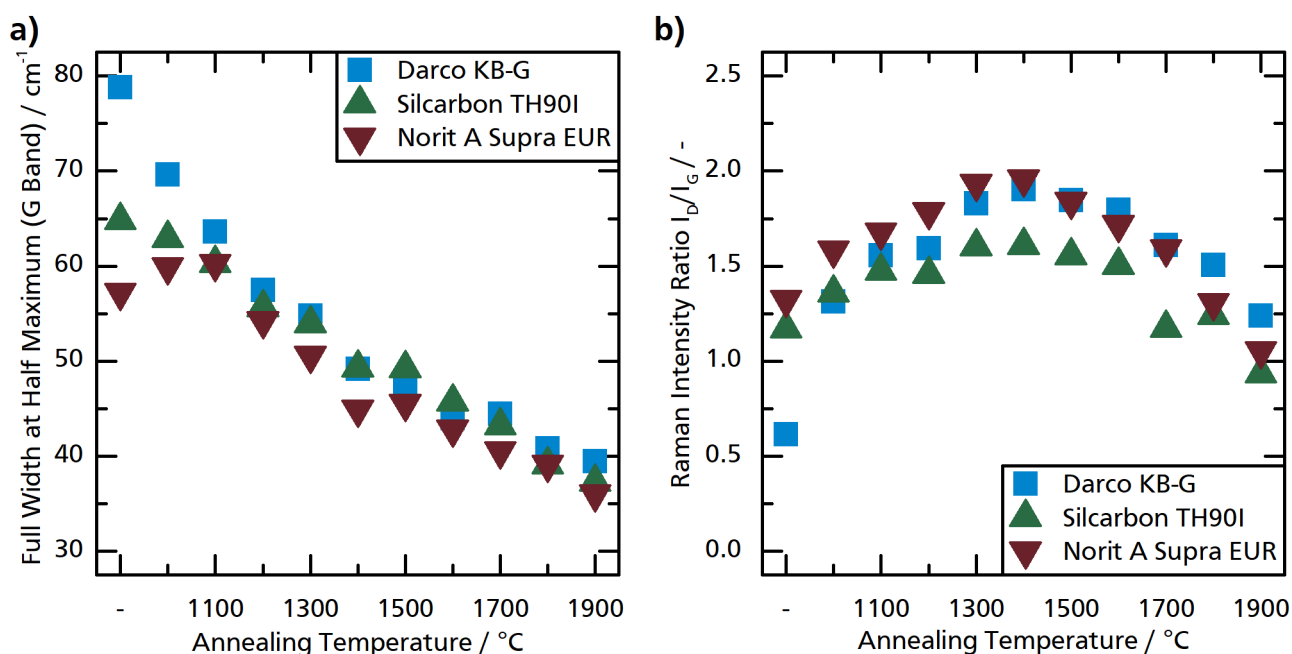


Figure 5.7: Influence of annealing temperature on **a)** full width at half maximum of the G band and **b)** intensity ratio of Raman bands from Raman spectroscopy for materials made from *Darco KB-G*, *Silcarbon TH90I*, and *Norit A Supra EUR* via vacuum annealing.

Figure 5.8a depicts the in-plane crystallite size obtained from XRD for the three activated carbon precursors and the resulting annealed materials. While no (100) reflex could be seen for either precursor, it develops after annealing with increasing temperatures. For *Darco KB-G*, the reflection starts to appear at $1600 \text{ }^\circ\text{C}$ and L_a increases slightly from 9.6 to 12.2 nm upon increasing the annealing temperature to $1900 \text{ }^\circ\text{C}$. For *Silcarbon TH90I* and *Norit A Supra EUR*, the reflection can be seen already at $1000 \text{ }^\circ\text{C}$ and the development of L_a is similar for all activated carbons with small deviations. In figure 5.8b, it can be seen that the deviation at higher temperatures is larger for L_c than for L_a . Nevertheless, a general trend of increasing out-of-plane crystallite size with increasing annealing temperature can be seen all precursors. Furthermore, the crystallite growth out-of-plane seems to be significantly higher than the in-plane growth. This indicates that a rearrangement of the orientation of basal planes to form larger crystallites might be primarily responsible for the increased crystallinity of the annealed materials.

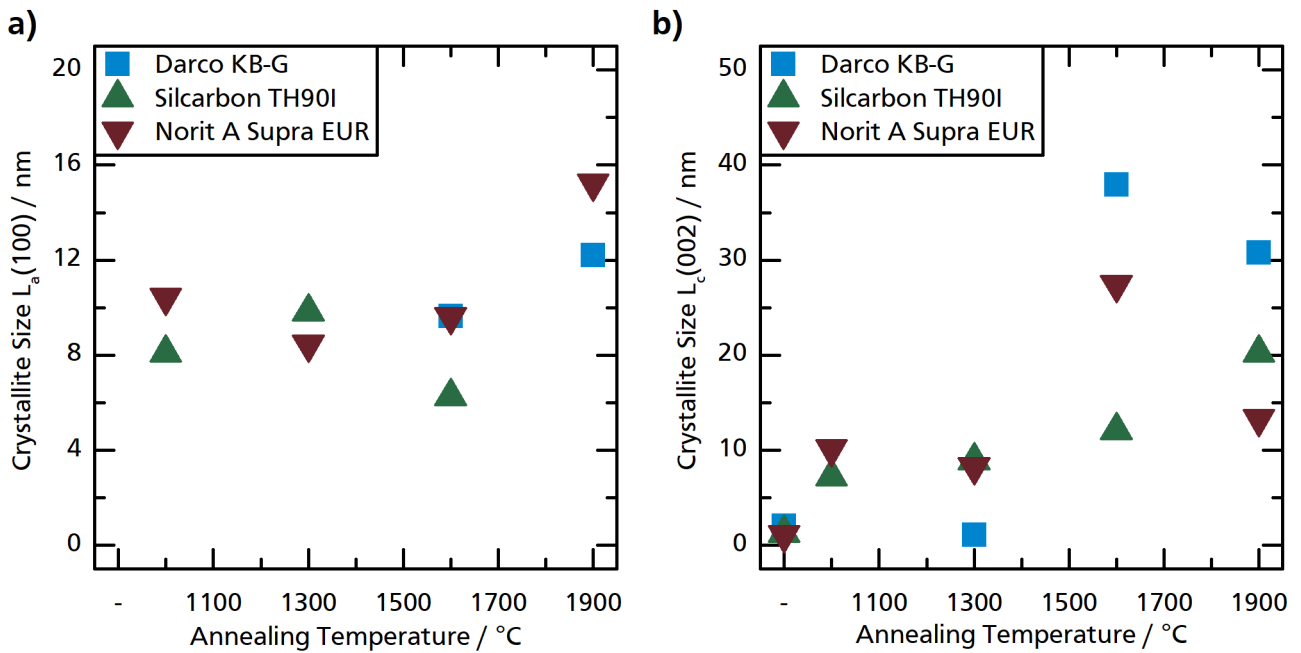


Figure 5.8: Influence of annealing temperature on **a)** crystallite size L_a and **b)** crystallite size L_c from X-Ray powder diffraction for materials made from *Darco KB-G*, *Silcarbon TH90I*, and *Norit A Supra EUR* via vacuum annealing.

Textural properties (BET specific surface area, total pore volume, average pore diameter) obtained from nitrogen physisorption are illustrated in figure 5.9 for the activated carbon precursors *Darco KB-G*, *Silcarbon TH90I*, and *Norit A Supra EUR* before and after vacuum annealing. All precursors initially show very high specific surface areas and exhibit a high micropore volume, but differ nonetheless in the values for the specific surface area (between 1239 and 1677 $\text{m}^2 \text{g}^{-1}$), total pore volume (between 0.56 and 1.17 $\text{cm}^3 \text{g}^{-1}$), and average pore diameter (between 1.82 and 3.09 nm). A common trend of decreasing SSA and total pore volume and increasing pore size with increasing annealing temperature can be observed for all three activated carbon precursors. In contrast to the microstructural properties, the textural properties do not converge to similar values after annealing at lower temperatures. Instead, the deviation of SSA between the pristine precursors of around 440 $\text{m}^2 \text{g}^{-1}$ increases up to 490 $\text{m}^2 \text{g}^{-1}$ after vacuum annealing at 1500 °C. Annealed carbons obtained from *Norit A Supra EUR* in the range from 1000 to 1500 °C exhibit higher specific surface areas than the corresponding carbonaceous materials obtained from the other precursors, because *Norit A Supra EUR* was the activated carbon with the highest initial SSA. Similar observations can be made for total pore volume and average pore diameter up to 1600 °C. At higher annealing temperatures, the textural properties of the different materials are closer to each other. While the resulting microstructure of the vacuum annealed materials are virtually independent of the initial precursor structure, the textural properties seem to depend on the activated carbon precursor.

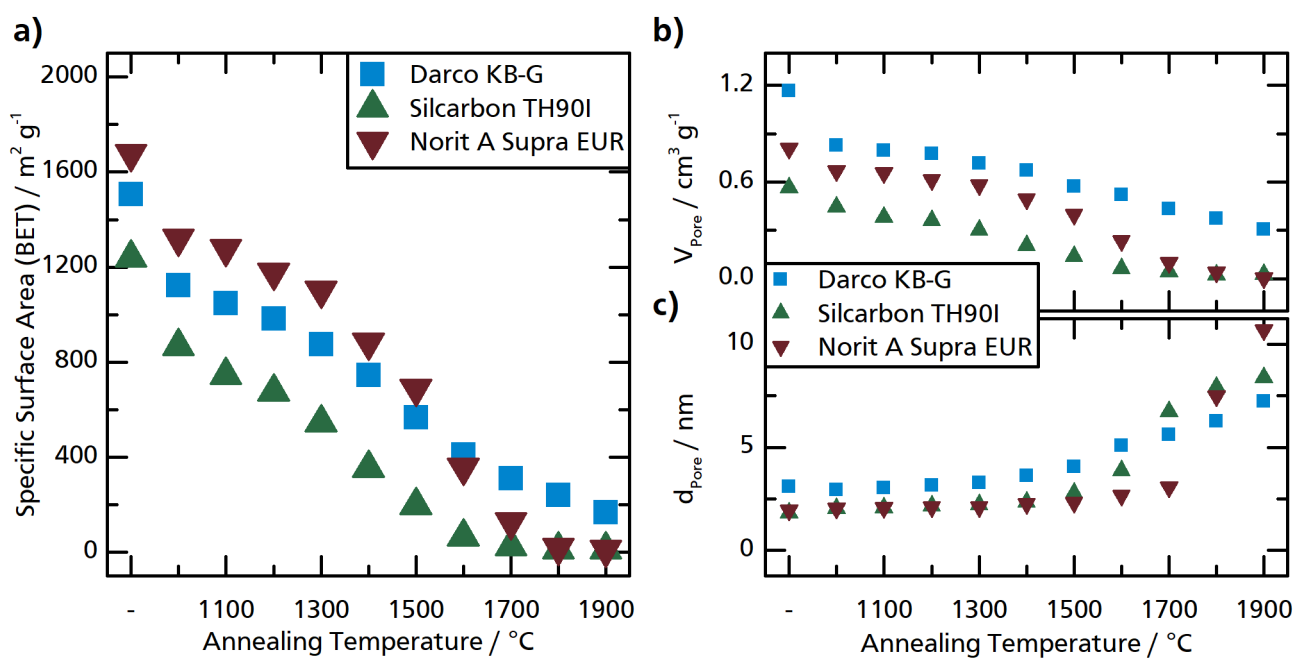


Figure 5.9: Influence of annealing temperature on **a)** BET specific surface area, **b)** total pore volume, and **c)** average pore diameter from nitrogen physisorption for materials made from *Darco KB-G*, *Silcarbon TH90I*, and *Norit A Supra EUR* via vacuum annealing.

5.1.3 Conclusion

It could be shown, that vacuum annealing of commercially available activated carbons presents a suitable pathway to obtain mesoporous and crystalline carbonaceous materials. With the help of vacuum annealing, the properties of different activated carbons can be modified to an extend. The annealing temperature is an important tuning parameter to influence both microstructure and textural properties of the resulting annealed carbonaceous materials, whereas the choice of argon pressure is negligible. Independent of the chosen activated carbon, materials with increased crystallinity and thermooxidative stability are obtained. Although the porosity of all these materials decrease and larger pores form, the extend of this development depends on the pore structure of the activated carbon precursor. Thus, the choice of the activated carbon can be seen as an additional tuning parameter. Unfortunately, with this method only low pore volumes and specific surface areas below $0.4 \text{ cm}^3 \text{ g}^{-1}$ and $200 \text{ m}^2 \text{ g}^{-1}$, respectively, were achieved for the highly crystalline materials obtained at the highest annealing temperature. The already existing structure of the received precursors limits the extend of control over the resulting carbon structure. In order to enhance this control even further, a process is needed, where the structure only starts to form during the process. A process where this might be possible is the chlorination of metal carbides for the synthesis of carbide-derived carbons.

5.2 Metal Carbides as Precursor for Mesoporous and Crystalline Carbons

An interesting feature of carbide-derived carbons is the tuneability of pore structure and crystallinity via the choice of synthesis parameters, mainly chlorination temperature and carbide precursor. Nevertheless, it is not understood, how these parameters determine the resulting CDC's structure. In this section, the thoroughly characterized carbide-derived carbons are discussed extensively in order to deduce the influence of synthesis temperature and carbide precursor on microstructure and textural properties.

5.2.1 Influence of Chlorination Temperature

The influence of the synthesis temperature was investigated by varying the chlorination temperature between 800 and 1600 °C. In this temperature range, CDCs from six different carbide precursors (NbC, SiC, TaC, TiC, VC, ZrC) were synthesized in order to compare the trends. X-ray diffraction patterns, TPO mass loss curves, Raman spectra, and adsorption / desorption isotherms from argon physisorption of the examined CDCs can be found in appendix B together with DOI links to the raw characterization data in an open access repository.

Carbon Microstructure

Figure 5.10a shows exemplary X-ray diffraction patterns of CDCs synthesized from NbC at different chlorination temperatures. Noticeably, no distinct reflection can be seen from the material produced at 1000 °C, showing that it is a rather amorphous material. Increasing the chlorination temperature leads to more pronounced carbon reflexes (002) and (100/101) the higher the temperature indicating an evolution from amorphous to more crystalline materials. This general trend can be observed for all examined carbide precursors, although CDCs from SiC show small reflexes even at lower temperatures. Furthermore, small but distinct carbide reflexes can be seen only for the materials TaC-CDC-1300, TaC-CDC-1400, VC-CDC-1000, and VC-CDC-1100. None of the other 32 CDCs show clearly distinguishable carbide reflexes, hinting to a close to complete conversion of the carbides. Both in-plane crystallite size L_a and out-of-plane crystallite size L_c , illustrated in figures 5.10b and c, generally increase with increasing synthesis temperature. An exception for this is L_c calculated from XRD patterns of SiC-CDCs, which is exceptionally high with more than 17 nm for all synthesis temperatures. CDCs from other carbide precursors show out-of-plane crystallite sizes ranging from 1.0 nm (NbC-CDC-1100) to 12.8 nm (TiC-CDC-1600), slightly increasing in this range with increasing chlorination temperature. Furthermore, all examined carbide-derived carbons exhibit in-plane crystallite sizes around 7 nm and thus comparable structural order in this direction in the low temperature regime. Synthesized at the highest temperature of 1600 °C, the CDC made from SiC shows an increased L_a of 14.2 nm, while all CDCs in the high temperature regime exhibit crystallite sizes above 20 nm. For all of them, the change from around 7 nm to above 20 nm is not gradual with increasing synthesis temperature but rather abrupt at certain temperatures differing for the different carbide precursors.

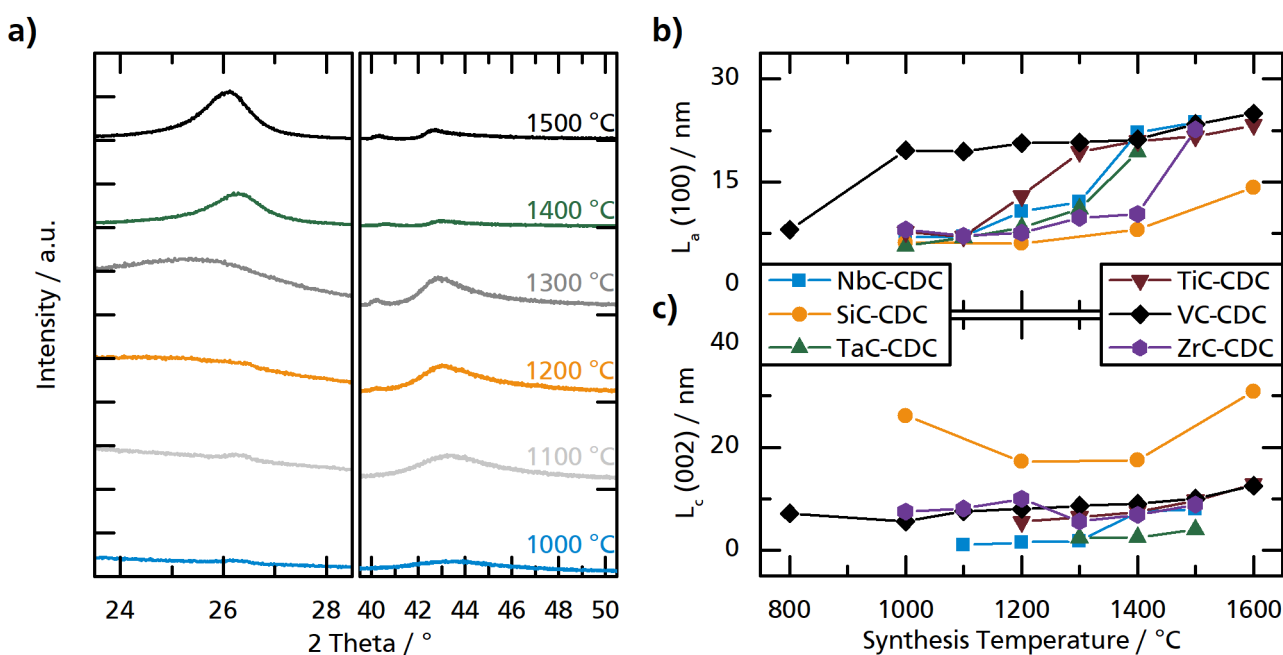


Figure 5.10: **a)** X-Ray powder diffraction patterns of CDCs synthesized from NbC at different temperatures. **b)** Crystallite size L_a and **c)** crystallite size L_c from X-ray powder diffraction measurements of CDCs synthesized from NbC, SiC, TaC, TiC, VC, and ZrC at different temperatures.

The mass loss curves of CDCs synthesized at different temperatures are shown exemplary in figure 5.11a with NbC-CDCs. The materials are stable up to a certain temperature, but after reaching the onset of oxidation, they quickly decompose with little remaining ash. The remaining ash mostly consists of metal oxides from incompletely converted carbide precursor enabling the calculation of conversions for the chlorination process. For most CDCs, the conversion exceeds 99 %. The only exceptions are VC-CDC-1000 and VC-CDC-1100 with 91 % and 80 % conversion, respectively. Xu *et al.* reported similar difficulties in completely converting vanadium carbide to carbide-derived carbon in this temperature range [180]. In this regime, vanadium atoms may be trapped inside the fast forming carbon structure, making them inaccessible for chlorine molecules. On the one hand, lower synthesis temperatures ($< 1000\text{ }^\circ\text{C}$) lead to more disordered carbon structures with an abundance of pores enabling the gas transfer. On the other hand, CDCs synthesized at higher temperatures ($> 1100\text{ }^\circ\text{C}$) usually exhibit larger pores with good accessibility. The temperature range in-between does not seem to benefit from either process in the case of VC and thus hinders the complete conversion. The small amount of vanadium atoms are not expected to influence the characterization methods regarding the carbon microstructure, but specific surface area and total pore volume from argon physisorption may be underestimated as they are normalized to the sample mass. With increasing chlorination temperatures, the mass loss curves of the CDCs are moved to higher temperatures regardless of the used carbide precursor. This indicates an increased thermooxidative stability in accordance with the increased structural order indicated by XRD measurements. Analogous to the annealed activated carbons, the onset temperature is used to compare the different materials (see figure 5.11b). It can be seen, that it is increasing with increasing synthesis temperature for all of them up to a maximum close to $650\text{ }^\circ\text{C}$ at the highest synthesis temperatures.

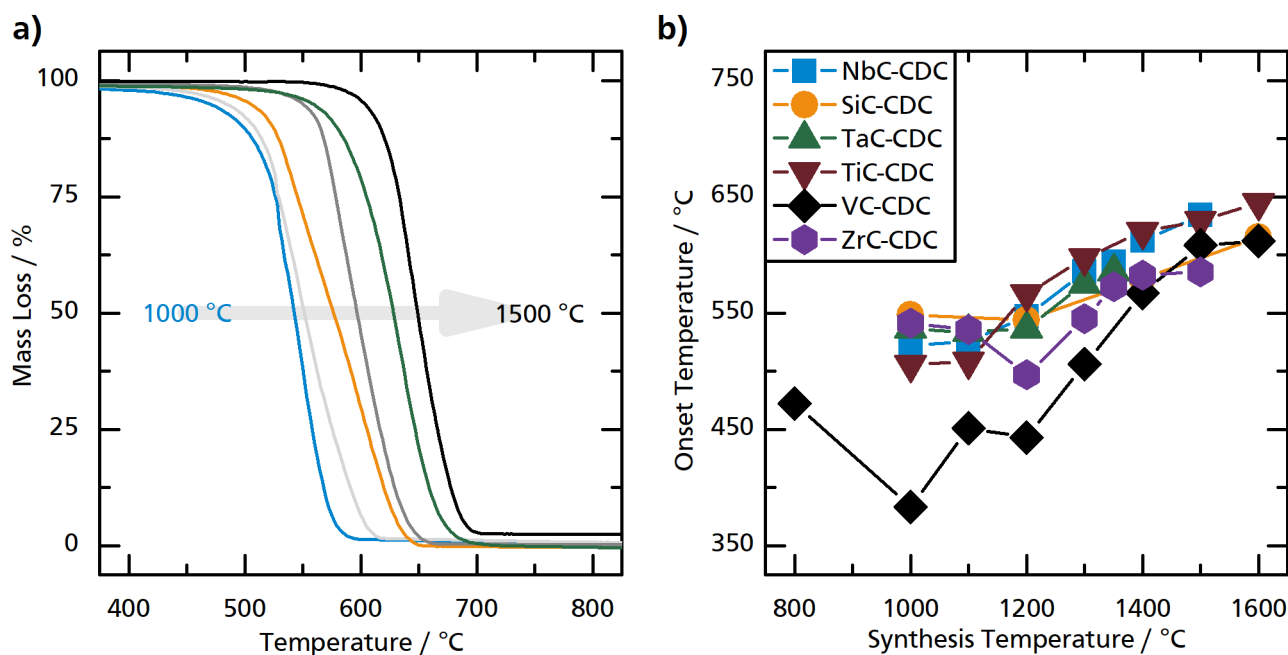


Figure 5.11: **a)** Mass loss curves from temperature-programmed oxidation of CDCs synthesized from NbC at different temperatures. **b)** Oxidation onset temperature of CDCs synthesized from NbC, SiC, TaC, TiC, VC, and ZrC at different temperatures.

All examined CDCs show the D and G bands in Raman spectroscopy, which are characteristic for carbonaceous materials. Furthermore, the second order band 2D at around 2700 cm^{-1} is at least slightly visible in all spectra. Figure 5.12a shows this exemplary for CDCs synthesized from NbC at different temperatures. With increasing chlorination temperature, a growing separation of the bands, a decreasing of the D band in relation to the G band, as well as a narrowing of the G band can be seen. Furthermore, the intensity of the 2D band is increasing with increasing synthesis temperature of the CDC. These aspects of the spectra evolution shown exemplary for NbC-CDCs is a clear indication for the increase in structural order with increasing chlorination temperature and can be found in the spectra of the carbonaceous materials obtained from all examined carbides [196, 199]. In detail, the full width at half maximum of the G band is decreasing for all examined carbide-derived carbons from above 75 cm^{-1} in the low temperature regime to below 30 cm^{-1} in the high temperature regime, except for the CDCs from SiC, which only reach a minimum of 43 cm^{-1} at 1600 °C (see figure 5.12b). The intensity ratio of the Raman bands, depicted in figure 5.12a, offers a similar trend, decreasing from above 1 in the low temperature regime to close to 0 in the high temperature regime. Again, SiC-CDC is the exception, with an almost constant ratio of about 1.2. In addition, the second order Raman intensity ratio I_{2D}/I_G (see figure 5.13b) supports the findings from the first order Raman bands: It is increasing from around 0.5 in the low temperature regime to above 0.75 in the high temperature regime, indicating increasing structural order [200].

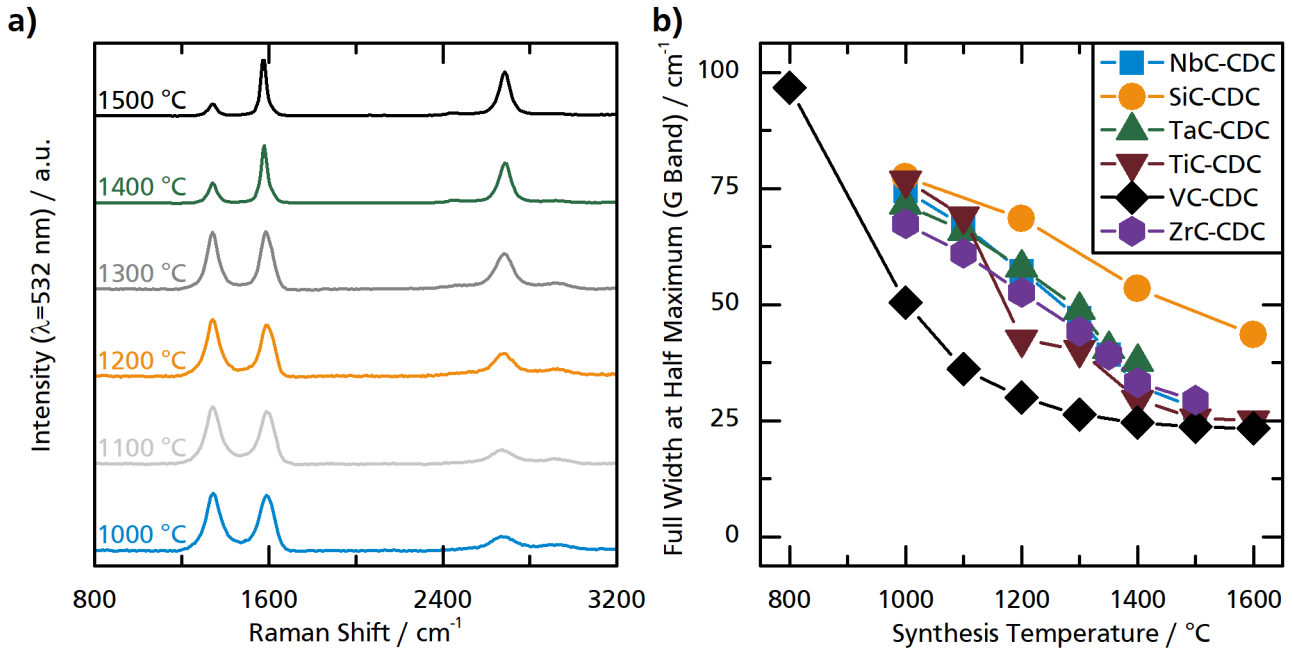


Figure 5.12: **a)** Raman spectra of CDCs synthesized from NbC at different temperatures. **b)** Full width at half maximum of Raman G band (FWHM) of CDCs synthesized from NbC, SiC, TaC, TiC, VC, and ZrC at different temperatures.

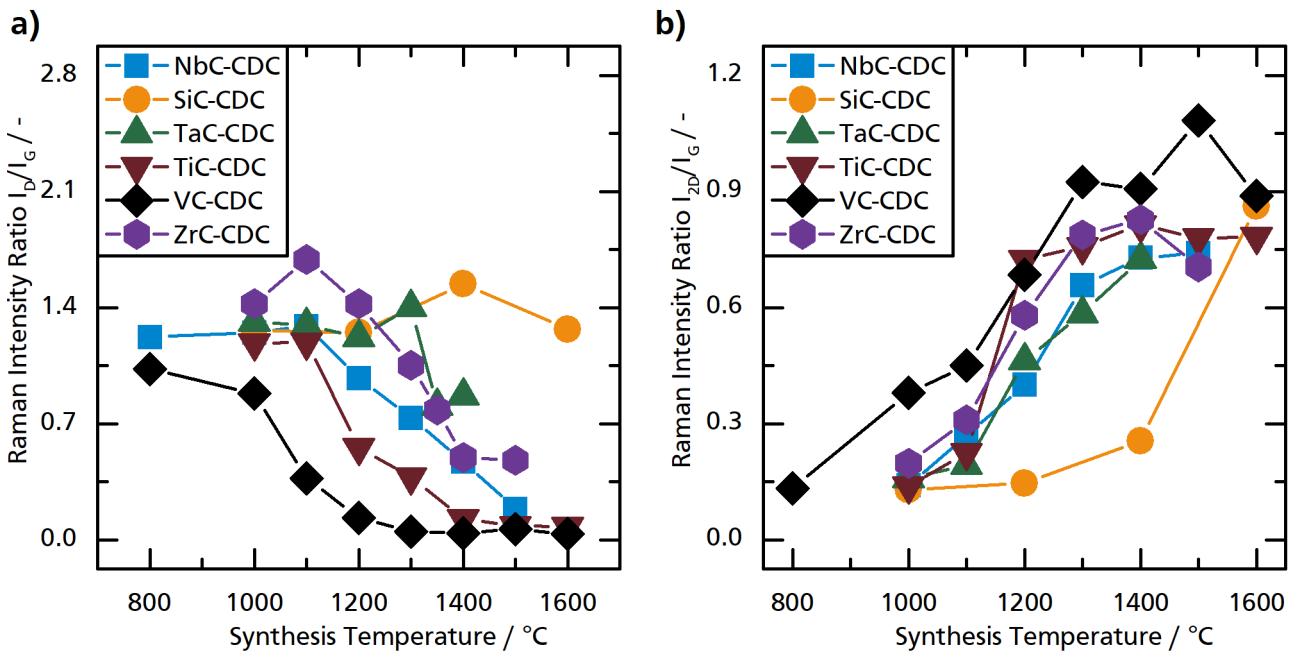


Figure 5.13: **a)** First order intensity ratio I_D/I_G , and **b)** second order intensity ratio I_{2D}/I_G of Raman bands of CDCs synthesized from NbC, SiC, TaC, TiC, VC, and ZrC at different temperatures.

All three characterization methods discussed above indicate a change from amorphous CDCs produced at lower temperature towards crystalline materials from chlorination at high temperatures. Whereas TPO measurements show similar trends for all carbide precursors, XRD and Raman spectroscopy hint at differences between the CDCs produced from different carbides. In both methods, CDCs from NbC, TaC, TiC, VC, and ZrC show similar structural orders in the low and high temperature regime, respectively, but differ in the temperature, where the transition from amorphous to crystalline takes place. CDCs from silicon carbide on the other hand show a significantly less increase in structural order with increasing synthesis temperature.

Textural Properties

Figure 5.14 illustrates adsorption and desorption isotherms from high resolution argon physisorption of CDCs synthesized from NbC and TiC at different temperatures. The materials obtained at 1000 °C both show isotherms of type I with virtually no hysteresis and a high knee indicating highly porous structures with a large amount of micro pores. With increasing synthesis temperature the knee of the isotherm is decreasing and thus indicating decreasing micropore volume. Additionally, the gradual change of curvature with the chlorination temperatures indicates an increasing mesopore volume. Furthermore, a pronounced hysteresis is developing. Generally, the isotherms show a shift of the pore size distribution towards larger pores with increasing synthesis temperature, the structure evolves from microporous to mesoporous, and even to a macroporous structure.

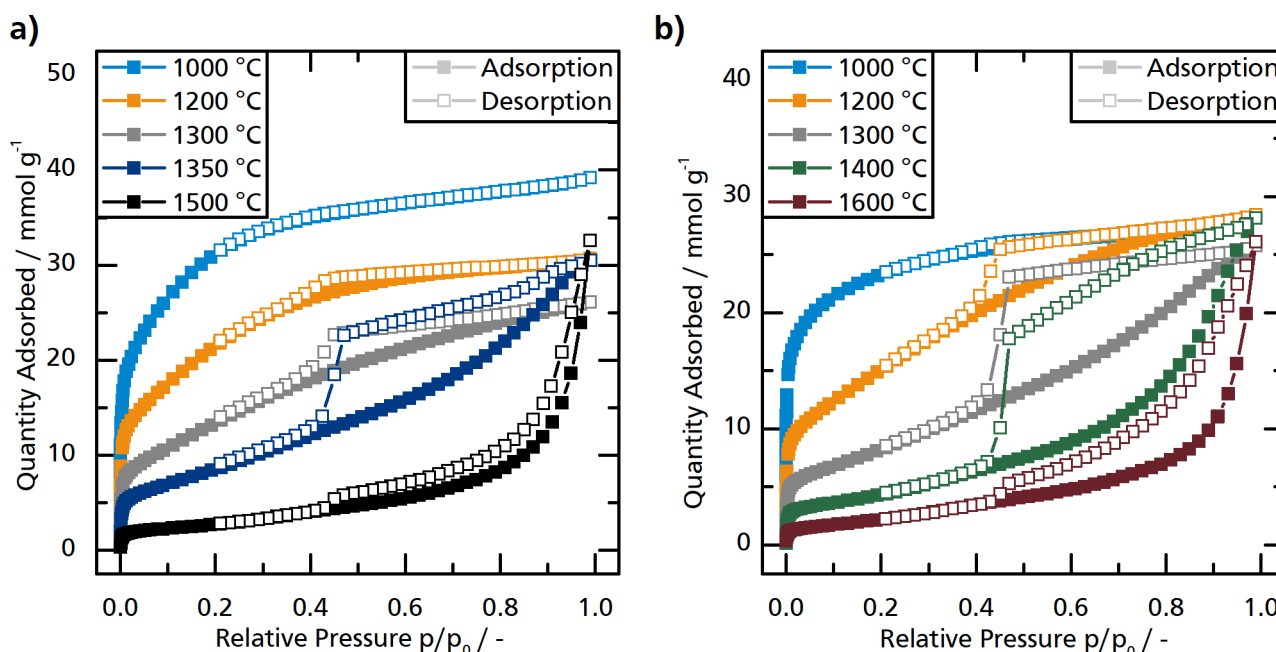


Figure 5.14: **a)** Adsorption / desorption isotherms from argon physisorption of CDCs synthesized from NbC at different temperatures. **b)** Adsorption / desorption isotherms from argon physisorption of CDCs synthesized from TiC at different temperatures.

In order to compare the isotherm shape of the CDCs from different carbides in detail, figure 5.15 depicts isotherms normalized to the maximum uptake. It can be seen, that both materials undergo the same development but at different temperatures. For example, the isotherm of NbC-CDC-1300 has a different shape than the one of TiC-CDC synthesized at the same temperature, but looks exactly like the isotherm from TiC-1200. A similar congruency can be seen for all examined carbide precursors except SiC, where the curvature of the isotherms does not change as much. Furthermore, all materials are microporous in the low temperature regime and while CDCs from SiC stay that way throughout the whole temperature range, CDCs from NbC, TaC, TiC, VC, and ZrC are mostly mesoporous in the high temperature regime.

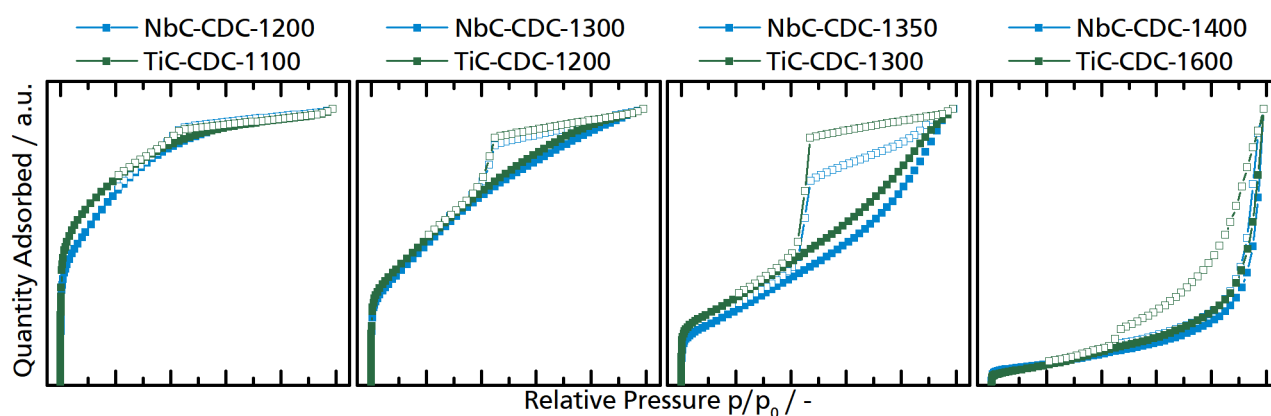


Figure 5.15: Comparison of normalized argon physisorption isotherms of CDCs synthesized from NbC and TiC at different temperatures.

Textural Properties obtained from argon physisorption of the carbide-derived carbons are summarized in table 5.2. The total pore volume does not show a common trend for the CDCs from different carbide precursors. It increases for zirconium carbide CDCs from $1.09 \text{ cm}^3 \text{ g}^{-1}$ at $1000 \text{ }^\circ\text{C}$ to $2.61 \text{ cm}^3 \text{ g}^{-1}$ at $1500 \text{ }^\circ\text{C}$, while it is almost constant around $0.8 \text{ cm}^3 \text{ g}^{-1}$ for TiC-CDCs in the same temperature range. Other carbide precursors result in different trends. This may result from the fact, that the bigger pores could not be filled completely during the measurements, resulting in underestimated values for carbide-derived carbons obtained in the high temperature regime. The specific surface area on the other hand shows a clear trend for all examined CDCs: it decreases with increasing synthesis temperature. For SiC-CDCs, it decreases from around $1400 \text{ m}^2 \text{ g}^{-1}$ at $1000 \text{ }^\circ\text{C}$ to around $800 \text{ m}^2 \text{ g}^{-1}$ at $1600 \text{ }^\circ\text{C}$. CDCs from all other carbide precursors exhibit a high SSA above $1600 \text{ m}^2 \text{ g}^{-1}$ at low synthesis temperatures and a decreased SSA below $400 \text{ m}^2 \text{ g}^{-1}$ at high synthesis temperatures. The transition from a microporous material with high specific surface area to material with low specific surface area but mesoporous structure takes place in a small temperature window, with the exact temperature depending on the carbide precursor.

Table 5.2: Textural properties of CDCs synthesized from NbC, SiC, TaC, TiC, VC, and ZrC at different temperatures.

Temperature °C	BET Specific Surface Area m ² g ⁻¹						Total Pore Volume cm ³ g ⁻¹					
	NbC	SiC	TaC	TiC	VC	ZrC	NbC	SiC	TaC	TiC	VC	ZrC
800	-	-	-	-	1902	-	-	-	-	-	0.82	-
1000	2289	1382	2407	1711	227	2273	1.11	0.55	1.13	0.79	0.18	1.09
1100	2019	-	2080	1668	72	2153	0.98	-	1.01	0.87	0.14	1.21
1200	1596	1422	1703	1128	304	1917	0.87	0.61	0.93	0.81	0.62	1.28
1300	1029	-	1167	638	231	1998	0.74	-	0.82	0.72	0.60	1.65
1350	672	-	826	-	-	1454	0.84	-	1.06	-	-	2.84
1400	367	1548	617	364	136	1089	1.22	1.09	1.09	0.78	0.46	2.37
1500	192	-	-	277	96	565	0.71	-	-	0.82	0.32	2.61
1600	-	831	-	211	64	-	-	0.53	-	0.64	0.20	-

5.2.2 Correlation of Carbide Precursor Structure to Carbide-Derived Carbon Structure

Although the structure of CDCs from different carbides showed a similar trend with the synthesis temperature, an influence of the precursor could be shown in the previous section. An obvious reason for this may be found in the structure of the different carbides. Niobium carbide, tantalum carbide, titanium carbide, vanadium carbide, and zirconium carbide are all so-called 'interstitial compounds', a type of intermetallic compound where small nonmetal atoms sit in interstitial holes in a metal lattice. These compounds maintain metallic character and exhibit a broad phase width [201]. The above mentioned carbides crystallize in a sodium chloride type structure (see structure in figure 5.16). This means, that every metal atoms is surrounded by six carbon atoms in octahedral arrangement and *vice versa*. The same periodic sequence of metal and carbon atoms can be found in every spacial direction. The carbides' structures only differ in the intermolecular distance, the lattice constant a , ranging from 0.4148 nm (VC) to 0.4696 nm (ZrC), with TiC (0.4328 nm), TaC (0.4435 nm), and NbC (0.4450 nm) in-between [202, 203]. Silicon carbide on the other hand is a so-called 'covalent carbide', crystallizing in more than 200 polytypes. In all of them, silicon atoms are surrounded by four carbon atoms in tetrahedral arrangement and *vice versa*, while they vary in the occupied sites along the c-axis of the hexagonal close-packing. The most commonly encountered polytype is α -SiC with a stacking order of ABCACB in a hexagonal unit cell. The lattice constants for this polytype are 0.30805 nm (a) and 1.51151 nm (c) [201, 204].

Five of the examined carbide precursors, identified above as crystallizing in a sodium chloride type structure, result in highly microporous and amorphous carbonaceous materials after chlorination in the low temperature regime, but form highly crystalline and mostly mesoporous materials in the high temperature regime. This transition can be seen most prominently with the temperature trends of crystallite size L_a obtained from XRD measurements and specific surface area from argon physisorption and takes places in a relatively small temperature window varying with the carbide precursor. Qualitatively, it can be seen, that the transition takes

place for CDCs from VC at the lowest temperatures, while the highest temperature is needed for CDCs from ZrC to undergo the transition. Conveniently, these carbide represent the examined precursors with the lowest and highest lattice constants, respectively. In order to examine the correlation further, the 'transition temperature' is introduced. For this purpose, figure 5.16 summarizes L_a as indicator for the crystallinity and SSA as indicator for the pore structure as function of the synthesis temperature for CDCs synthesized from the interstitial carbides. Guidance for the average values observed before the transition (low synthesis temperature) and after the transition (high synthesis temperature) is given with the help of dashed lines. The average between the dashed lines is 15 nm for L_a and $1000 \text{ m}^2 \text{ g}^{-1}$ for SSA and is represented by a gray bar in the diagrams. The transition temperature is the temperature at which the graph of the respective carbide precursor passes the average value. Noticeably, the transition for both indicators more or less occurs at the same transition temperature for each individual carbide, but is a function of the carbide precursor employed. For example, the precursor niobium carbide offers transition temperatures of 1328°C (L_a) and 1274°C (SSA), which results in the largest deviation for all examined carbides of only 54°C . On the one hand, this underlines the link between crystallinity and pore structure in these material. On the other hand, this enables the demonstration of a correlation between carbide precursor structure and resulting carbide-derived carbon structure by plotting the transition temperatures versus the lattice constants of the carbide precursors (figure 5.16, right hand side). A clear correlation for all rock salt type structures can be found: the temperature needed for a transition towards crystalline and mesoporous CDCs increases with larger lattice constants of the carbide precursor.

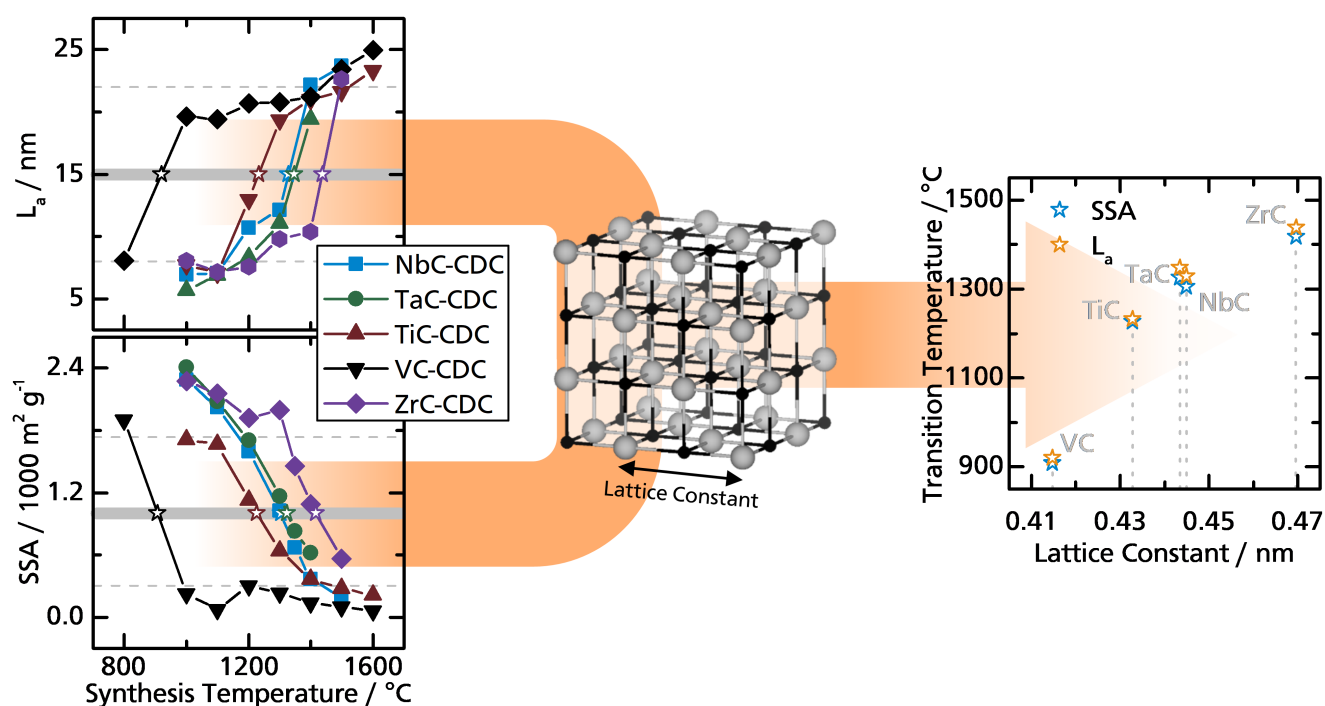


Figure 5.16: Correlation of transition temperatures with lattice constants of the carbide precursors crystallizing in sodium chloride type structure.

A feature of the sodium chloride structure is that the lattice constant coincides with the distance between two atoms of the same element in all spatial directions. In ideal graphite, the carbon to carbon distance is 0.147 nm in plane and 0.335 nm between the planes [205] whereas the initial carbon to carbon distances in the precursor are all above 0.41 nm. Thus, the carbon atoms need to close their distance after metal extraction in order to rearrange and form crystalline carbon domains. Presumably, the bigger the carbide's lattice constant, the longer the distance required to overcome for rearrangement. To do this, a higher mobility might be needed, which could be provided by a higher temperature during the synthesis. This is reflected in the correlation between transition temperature and lattice constant: vanadium carbide with a carbon to carbon distance closest to the interplanar distance in graphite exhibits the lowest transition temperature, while zirconium carbide with the largest lattice constant exhibits the highest transition temperature. Presumably, the graphitized domains in these materials arise directly during the initial CDC formation.

From the six examined carbide precursors, silicon carbide is the only one not fitting into this scheme, while being also the only one not crystallizing in sodium chloride type structure. CDCs from SiC do not reach the level of crystallinity the other CDCs show when synthesized at high temperatures. Nevertheless, a comparably slight increase in structural order and decrease in specific surface area can be observed at 1600 °C, which could be attributed to thermal annealing. For post annealed CDCs around 1600 °C the formation of graphitized domains was found independent of the initial carbon structure prior to the annealing [176]. Thus, in contrast to CDC from the other examined carbide precursors, these domains most likely form after the initial CDC formation. An explanation for this may lay in the different structure of SiC compared to NbC, TaC, TiC, VC, and ZrC and two effects may contribute to this. On the one hand, the carbon atoms in rock salt type structures may already be oriented in sheets with more regular distances than in the hexagonal close-packing of SiC. In theory, this could promote the formation of graphite ribbons with the correct orientation to already formed ribbons in the interstitial carbide while this is not the case in SiC. On the other hand, the carbon to carbon distances in SiC are already smaller than the basal plane distance in graphite. Saturation to direct C-C bonds immediately after metal extraction and formation of graphitic ribbons with a distance of 0.335 nm may be impeded.

5.2.3 Conclusion

In summary, a direct correlation between the precursor structure and the resulting carbon structure at different temperatures was found for carbide-derived carbons obtained from carbides with sodium chloride structure. They show a similar and sharp transition from amorphous materials with micropores to significantly more crystalline materials with mesopores. The temperature at which this transition occurs was correlated to the lattice constant of the carbide precursor. Smaller lattice constants and thus smaller initial carbon to carbon distances lead to lower transition temperatures. Furthermore, it could be shown, that a carbide precursor with a different structure, namely silicon carbide, does not show the same transition. Only a thermal rearrangement due to high synthesis temperatures could be seen. These findings contribute to a better understanding of the

microstructure formation in CDCs and allow the prediction of structural properties for CDCs from other binary carbides. Hafnium carbide is another carbide exhibiting a stone salt type structure ($a = 0.4639$ nm) [202]. It stands to reason, that carbide-derived carbons from HfC undergo the same transition seen with the other interstitial carbides with a transition temperature close to ZrC as their lattice constants are similar. CDCs from other carbides with more complex structures like tungsten carbide [206] and boron carbide [207] are not expected to undergo an abrupt transition but a rather slow slight increasing structural order due to thermal rearrangement similar to SiC-CDCs. This new understanding is a step toward CDCs as tailor-made model materials for electrochemical applications.

5.3 Exemplary Application of Pt/C Catalysts in Oxygen Reduction Reaction

5.3.1 Deposition of Platinum on Carbide-Derived Carbons with Varying Properties

The possibility to employ the prepared carbide-derived carbons as support material for platinum catalysts in the oxygen reduction reaction is examined in the following sections. With this goal, the platinum deposition on a selection of CDCs is investigated. This includes the electrochemical properties of the resulting catalysts as well as the effect of the properties of the carbonaceous materials on the platinum deposition.

With this purpose, 18 CDCs were chosen from the multitude of materials described in the previous sections. Figure 5.17 represents a map of the CDCs' properties by plotting structural properties (crystallite size, Raman intensity ratio) against textural properties (specific surface area, total pore volume). Selected CDCs for the use as support material are colored while the others are marked in gray. In addition to the complete set of TiC-CDCs, CDCs synthesized at temperatures higher and lower than the transition temperature of their respective carbide precursor were selected. Furthermore, figure 5.17 shows that the complete range of properties is covered with CDCs obtained from different precursors. All of the selected materials were loaded with platinum according to the incipient wetness procedure described in the experimental section and the loading was controlled via ICP-OES. Moreover, the resulting catalysts were characterized electrochemically in regard to their double layer capacitance, and electrochemical surface area, while the platinum particle size was calculated from X-ray powder diffraction measurements. Accelerated durability tests were developed in order to see how the catalyst properties change due to electrochemical stress and how the choice of support material can influence it. As a representative for the properties of the support material, the BET specific surface area is selected over the total pore volume because the latter is less accurate due to incomplete pore filling during the physisorption measurements in some of the more mesoporous materials as evidenced by their adsorption isotherms. Furthermore, the specific surface area almost linearly correlates to the microstructural properties of the CDCs, especially the in-plane crystallite size obtained from XRD and the Raman intensity ratio (see left hand tiles in figure 5.17). This way, the SSA can serve as a figure of merit for the textural properties as well as for the carbon microstructure (indirectly).

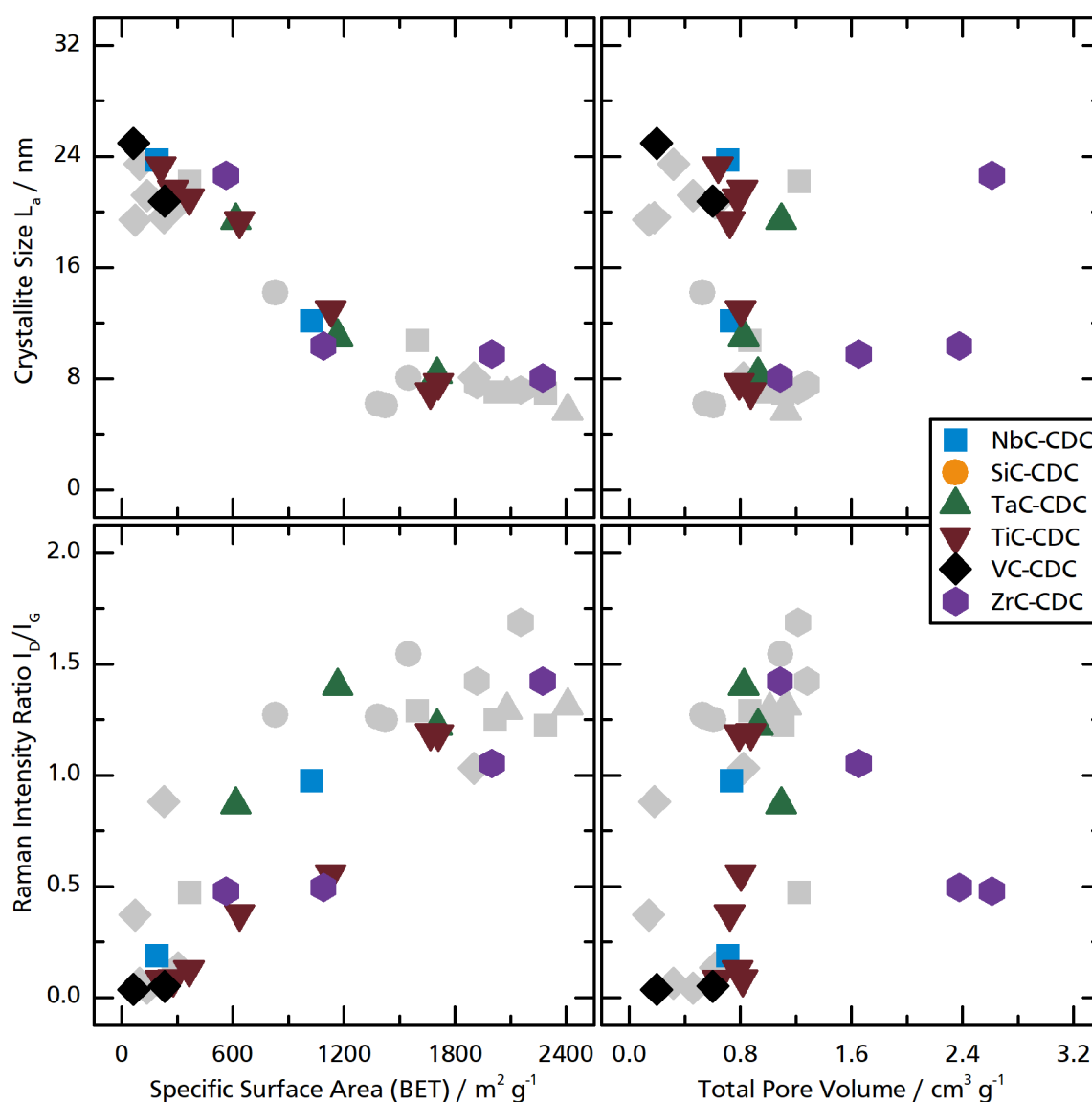


Figure 5.17: Structural properties (crystallite size, Raman intensity ratio) of examined carbide-derived carbons plotted against textural properties (specific surface area, total pore volume) for the selection as support material. Gray: CDCs not used as support material for Pt/C catalysts.

Catalyst Characterization

Figure 5.18 shows the double layer capacitance of the examined platinum catalyst in regard to the specific surface area of the support material. The double-layer capacitance stems from the charged species and oriented dipoles at the electrode / solution interface making up the so-called *electrical double layer* [36]. This means, that every part of the catalysts that is accessible for the electrolyte, no matter whether it is made up off carbon or platinum, contributes equally to to the double layer capacitance. Thus, the DLC can be used as an electrochemical measure for the surface area of the catalyst which is accessible for the electrolyte. In the case of the examined platinum on CDC support catalysts, this surface area comes from the CDCs surface

area for the most part and should correlate to it. This can be seen in figure 5.18 as the DLC almost linearly increases with increasing SSA of the support material with increasing deviation for the highly microporous materials. These deviation might stem from a different accessibility of parts of the porous system for the electrolyte molecule (water) compared to the probing molecule of the physisorption (argon). Extremely small pores or pore entrances might be accessible for argon but not for water. Furthermore, after the platinum deposition on the carbide-derived carbons, platinum clusters cover the carbon surface and may block parts of the pore structure and thus decrease the DLC of the catalyst in proportion to the SSA of the pristine support material. Nevertheless, it could be shown, that the double layer capacitance of the catalysts can be used as a measure for the carbon surface. Thus, it can be employed to gauge effects of electrochemical stress on the catalyst in terms of carbon corrosion, although additional effects concerning the accessibility have to be considered.

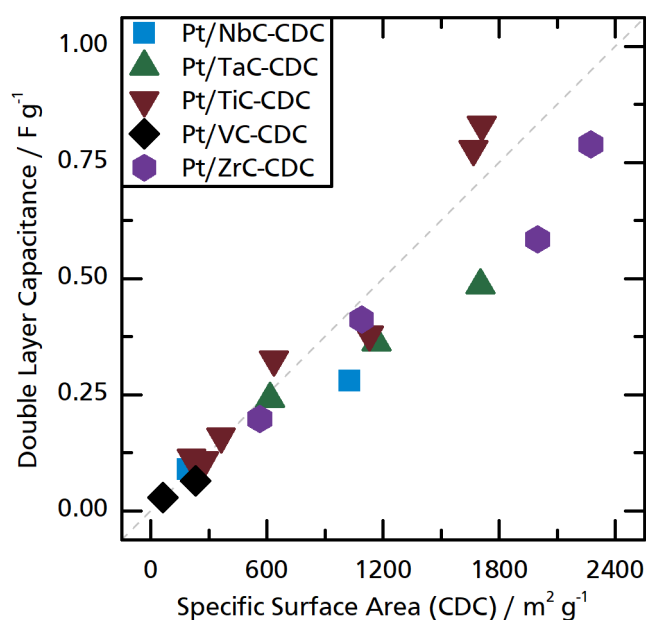


Figure 5.18: Influence of the carbonaceous support's specific surface area on double layer capacitance for platinum catalysts with CDCs from NbC, TaC, TiC, VC, and ZrC as support material.

ICP-OES results, converted into mass fractions and shown in figure 5.19a, show that platinum loadings close to the target loading of 20 wt-% were achieved independent of the carbonaceous support with an average of 19.8 ± 1.5 wt-%. This is important in order to be able to compare the catalysts without having to account for strongly differing platinum loadings. The largest deviation towards lower platinum loading is found in Pt/TiC-1000 with 16.2 wt-%, while Pt/TaC-1200 shows the largest deviation towards higher platinum loading with 22.3 wt-%. Figure 5.19b depicts the platinum particle diameter obtained from XRD measurements with respect to the specific surface area of the carbonaceous support. It is decreasing with increasing SSA where Pt/VC-1600 exhibits the largest platinum particles (13.7 nm) due to the extremely low surface area of its support material ($64 \text{ m}^2 \text{ g}^{-1}$). The other side of the scale is represented by Pt/ZrC-1300 with a platinum particle diameter of 1.4 nm as its support material exhibits an SSA of around $2000 \text{ m}^2 \text{ g}^{-1}$. An explanation for

this trend is that larger surface areas of the CDC support material enable higher dispersion of the platinum particle and thus result in smaller platinum particles in the finished catalyst. One exception for this trend can be found in figure 5.19b with Pt/ZrC-1000. Its support material is highly microporous with an SSA of more than $2250 \text{ m}^2 \text{ g}^{-1}$. Presumably, it contains extremely small pores or pore entrances so that a significant part of the carbon surface might not have been accessible for the platinum precursor. This would result in a reduced effective surface area available for the platinum dispersion and thus larger particles would be formed than expected.

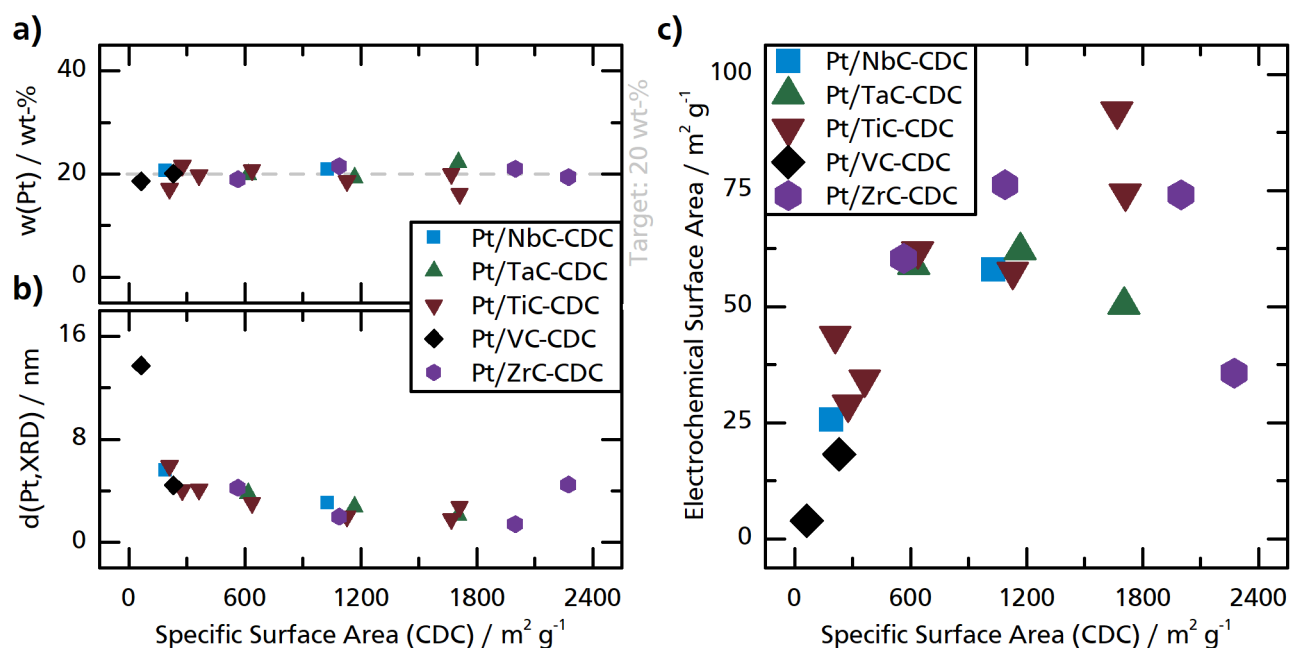


Figure 5.19: Influence of the carbonaceous support's specific surface area on **a)** platinum loading from ICP measurements, **b)** platinum particle diameter from XRD measurements, and **c)** electrochemical surface area for platinum catalysts with CDCs from NbC, TaC, TiC, VC, and ZrC as support material.

The electrochemical surface areas, corresponding to the electrochemically active surface area of the platinum particle, is presented in figure 5.19c with regard to the specific surface area of the support material. The ECSA increases with increasing SSA in accordance with the platinum particle size. Smaller particles exhibit more surface area per weight and thus result in a higher ECSA. Accordingly, Pt/VC-1600 exhibits the lowest ECSA with $3.9 \text{ m}^2 \text{ g}^{-1}$. The highest ECSA could be achieved with the catalyst based on TiC-1100 ($92.1 \text{ m}^2 \text{ g}^{-1}$). For the ECSA there are three apparent exceptions regarding the trend with increasing SSA: Pt/ZrC-1000 ($35.7 \text{ m}^2 \text{ g}^{-1}$) which can be explained by the larger than expected platinum particles discussed above, as well as Pt/TaC-1200 ($50.3 \text{ m}^2 \text{ g}^{-1}$) and Pt/ZrC-1300 ($74.1 \text{ m}^2 \text{ g}^{-1}$). Considering figure 5.18, the three catalysts show a decreased DLC in proportion to the specific surface area of the pristine support material which hints towards a reduced accessibility of the pore structure for the electrolyte molecules. This seems to influence the ECSA of the catalysts as well, meaning that not the entirety of the platinum surface area may be available for the electrochemical reaction.

Accelerated Durability Tests

All in all, the characterization of the platinum particles on the various catalysts showed differences in size and accessibility of the platinum clusters. Thus, when testing the stability of the catalysts with the help of accelerated durability test procedures, changes in carbon structure and platinum particles have to be considered. In this context, the double layer capacitance as a measure for the carbon surface will be used to gauge changes to the carbon structure and the electrochemical surface area as a measure for the platinum particle size will be used to examine changes to the platinum particles. Both quantities will be expressed in regard to the value before the ADT and labeled 'relative DLC' and 'relative ECSA', respectively. In order to find suitable potential ranges for the accelerated durability test procedures, four different ranges were tested: 0.6 - 1.1 V, 0.6 - 1.2 V, 0.6 - 1.3 V, and 0.6 - 1.4 V. The number of cycles for each potential range were chosen with regard to the time needed to perform the ADT and with the goal to be able to conclude the test over the course of one night. Two catalysts with different CDCs as support material were used for the test: Pt/TiC-1000 with a rather amorphous and microporous support material, and Pt/TiC-1500 based on a more crystalline and mesoporous carbonaceous support. Before each stability test, in-between cycles, and afterwards cyclic voltammograms were recorded in order to monitor the catalyst degradation at six different points of the process. They are presented in figures C.1 and C.2 in the appendix for all examined potential ranges for Pt/TiC-1000 and Pt/TiC-1500, respectively. It was found, that all current peaks decrease in intensity with increasing number of cycles for all examined potential ranges.

Figures 5.20a and b give the resulting relative electrochemical surface areas calculated from the cyclic voltammograms. What could be seen in the raw cyclic voltammograms qualitatively, can be seen now quantitatively: the ECSA is decreasing with increasing number of potential cycles for all examined potential ranges. Furthermore, the decrease is more distinct the greater the potential range, thus the harsher the conditions. The difference between varying potential ranges is greater for the catalyst Pt/TiC-1000 than for Pt/TiC-1500. While both catalysts exhibit similar relative ECSAs after 5000 cycles at 0.6 - 1.1 V (82 and 74 %), Pt/TiC-1000 shows a much lower rel. ECSA (28 %) than Pt/TiC-1500 (48 %) after 3000 cycles at 0.6 - 1.4 V. Figures 5.20c and d present relative double layer capacitances for the examined catalysts in the four potential ranges. For Pt/TiC-1500 a similar trend can be observed for all potential ranges as the DLC decreases with increasing number of cycles. The relative DLC at the end of the ADT decreases from 64 to 50 % when increasing the upper potential limit from 1.1 to 1.4 V. For Pt/TiC-1000 the three milder potential ranges show a similar trend to the one observed for Pt/TiC-1500, but the harshest potential range results in increasing DLC with increasing number of cycles. These different trends for support material with different crystallinities will be discussed later on, together with the results from stability tests with the complete set of catalysts. Regarding the choice of potential ranges for further ADTs, it can be said that the potential range between 0.6 and 1.4 V results in a decidedly different trend while the other the ranges result in similar trends. Furthermore, the difference in stability is most pronounced for each catalyst when comparing the mildest (0.6 - 1.1 V) and the harshest (0.6 - 1.4 V) conditions. This is the reason why those two potential ranges are used to examine the stability for the complete set of catalysts.

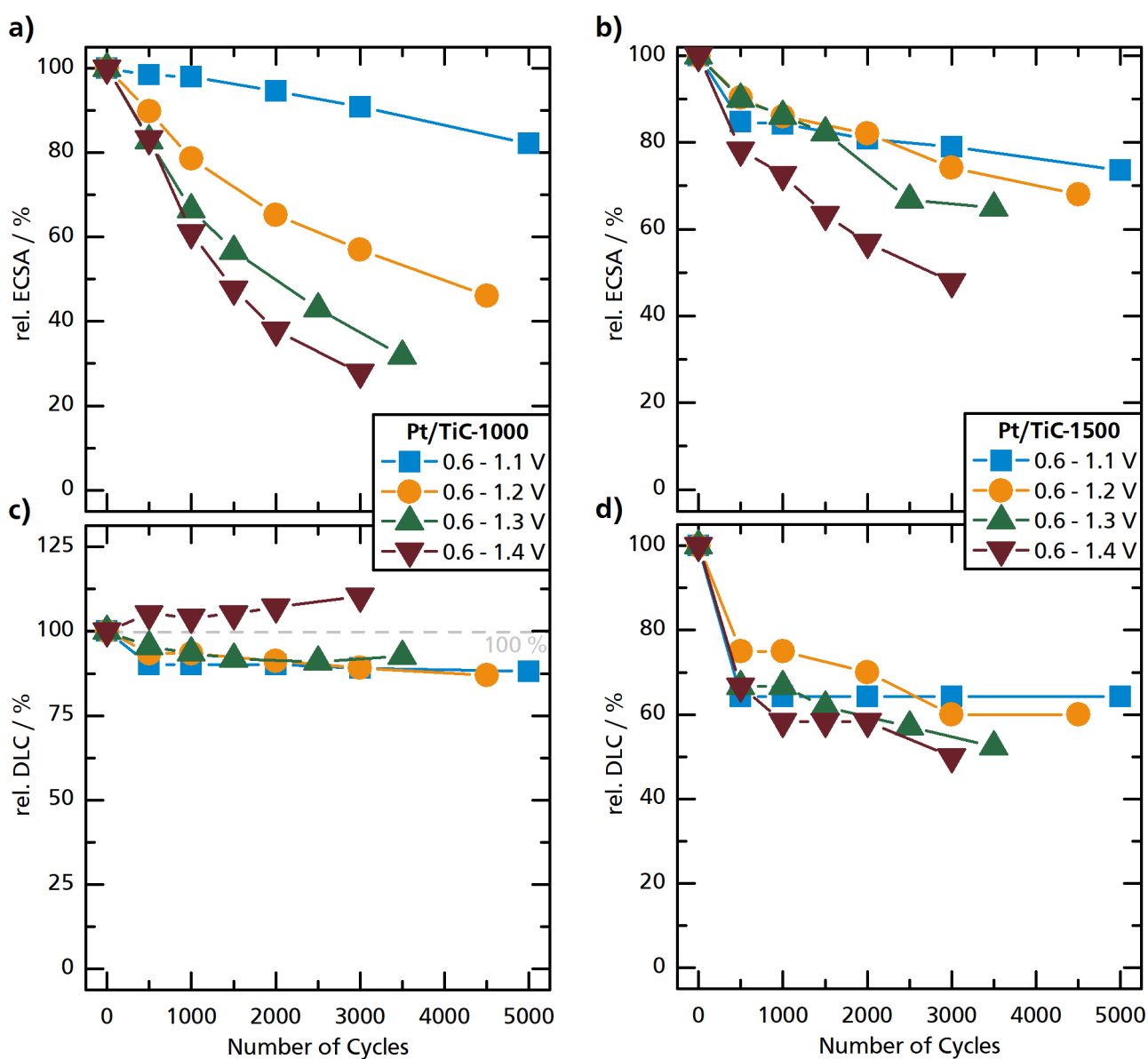


Figure 5.20: Results from accelerated durability tests in different potential ranges. Influence of number of cycles on relative electrochemical surface area for **a)** Pt/TiC-1000 and **b)** Pt/TiC-1500, as well as relative double layer capacitance for **c)** Pt/TiC-1000 and **d)** Pt/TiC-1500.

The effect of accelerated durability tests on the ECSA in terms of relative ECSA for all prepared catalysts is illustrated in figures 5.21a and c. After 5000 cycles at 0.6 - 1.1 V, the relative electrochemical surface area is generally decreasing with increasing specific surface area of the carbonaceous support. Two effects may have a part in this trend: firstly, XRD results presented in figure 5.19b showed smaller platinum particles on carbonaceous support with higher SSA. These smaller platinum particles are more prone to dissolution resulting in the loss of platinum as well as increase of particle size due to Ostwald ripening and reprecipitation [49, 56]. Thus, the platinum surface area decreases. Secondly, carbide-derived carbons with larger specific

surface areas generally exhibit a lower structural order than those with lower surface areas as discussed in chapter 5.2. A lower structural order will result in an increased carbon corrosion during electrochemical stress [49, 53]. Induced by the carbon corrosion, a detachment of platinum particles may take place and would result in further decreased observed ECSA. Under harsher conditions, the trend of decreasing relative ECSA with increasing SSA of the support material is even more pronounced. The crystallinity of the support material seems to play a more pronounced role under these conditions suggesting that carbon corrosion is the primary degradation mechanism in this case.

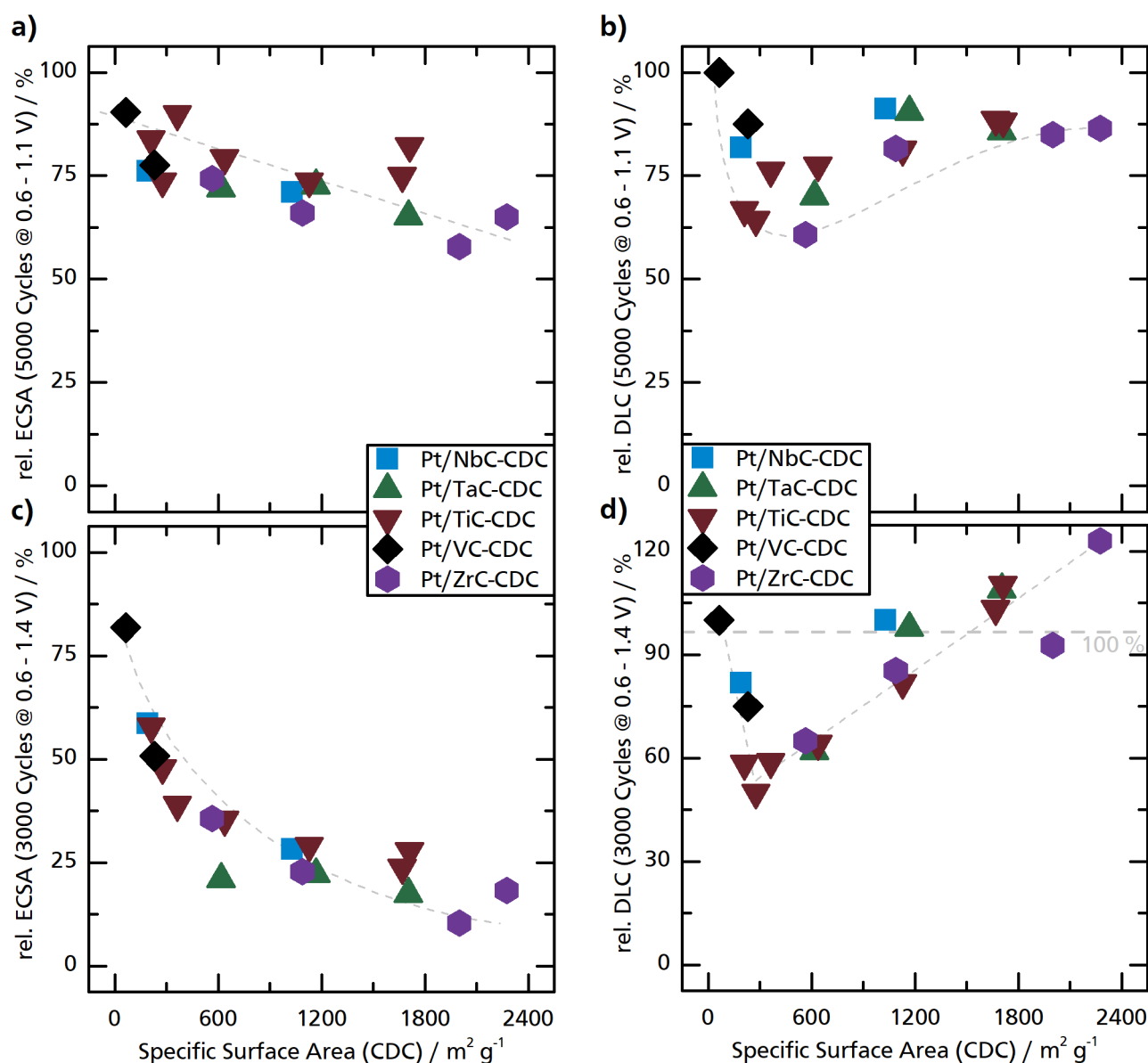


Figure 5.21: Influence of the carbonaceous support's SSA on **a)** relative ECSA and **b)** relative DLC after 5000 cycles at 0.6 - 1.1 V, as well as **c)** relative ECSA and **d)** relative DLC after 3000 cycles at 0.6 - 1.4 V for platinum catalysts with CDCs from NbC, TaC, TiC, and ZrC as support material.

Figures 5.21b and d illustrate the corresponding relative double layer capacitances for the examined catalysts after undergoing accelerated durability tests. Generally, a similar trend can be observed for both potential ranges: For catalysts supported on CDCs with surface areas in the lower range, the relative DLC decreases with increasing SSA to a minimum at around $300 \text{ m}^2 \text{ g}^{-1}$. For catalysts based on CDCs with higher surface areas than that, the relative DLC increases with increasing specific surface area of the support. This trend is more pronounced under the harsher cycling conditions where the relative DLC even exceeds 100 % for the most microporous materials with a maximum of 123 % for Pt/ZrC-1000.

Although varying in their structural order, most examined carbonaceous supports exhibit domains with more amorphous carbon which undergo carbon corrosion during the potential cycling which is accelerated under harsher conditions [50, 53]. For the materials with high specific surface areas, which are highly microporous, the carbon corrosion may result in the opening of pores that were previously inaccessible for the electrolyte. Especially Pt/ZrC-1000 is an example for this, as the catalyst was shown to exhibit a lower DLC than expected, which was attributed to the possibility of extremely small pores or pore entrances. After 3000 cycles at 0.6 - 1.4 V, its DLC increased to 0.89 F g^{-1} and would lay on the diagonal depicted in figure 5.18. With decreasing SSA, the pore size of the CDCs generally increases. Under carbon corrosion, the pore size of mesopores and macropores might be increased further and thus decrease the DLC. Presumably, this effect dominates for the support materials of the catalysts close to the minimum of the relative DLC. The CDCs with the lowest SSAs also exhibit the most crystalline structures and are thus less prone to carbon corrosion which explains the smaller changes in DLC for these materials.

5.3.2 Effect of Thermal Presintering of Carbon Supported Platinum Catalysts

Based on the results from the previous section, four catalysts with different initial properties were chosen to undergo a thermal presintering and to be employed in the oxygen reduction reaction in an RDE setup: Pt/TiC-1300, Pt/TiC-1600, Pt/ZrC-1400, and Pt/ZrC-1500. The support materials ZrC-CDC-1400 and ZrC-CDC-1500 were synthesized just below and above the transition temperature for ZrC of about $1430 \text{ }^\circ\text{C}$. Both TiC-CDC support material were obtained above the transition temperature for TiC of about $1230 \text{ }^\circ\text{C}$, but while the transition is thought to be completed for TiC-CDC-1600, TiC-CDC-1300 shows still a lower structural order. The initial platinum particle diameters of the catalysts range from 1.97 nm (Pt/ZrC-1400) to 5.91 nm (Pt/TiC-1600) so that the effect of thermal presintering on platinum particles of different sizes can be observed.

Exemplary, the platinum particle diameters of the catalysts Pt/TiC-1300 and Pt/TiC-1600 after sintering at temperatures between 400 and $900 \text{ }^\circ\text{C}$ were obtained from XRD measurements and the platinum content was analyzed via ICP-OES for the catalysts sintered at 600 and $900 \text{ }^\circ\text{C}$. The results are summarized in table 5.3. For both catalysts, the platinum particle diameter increases with increasing sintering temperature as expected. Additionally, the platinum loading increased due to the sintering process. No platinum was added during the process, which means, that the support material must have lost mass either in the form of surface groups

or bulk carbon. Because the support materials were synthesized at temperatures way above the sintering temperatures, no influence of the sintering process on the carbon structure was expected. Nevertheless, a small decrease of DLC can be observed for the catalysts Pt/TiC-1300 and Pt/TiC-1600 (see appendix, figure C.3). This change is too small to fully explain the increase of platinum loading from 20.4 to 22.1 wt-% (Pt/TiC-1300) or 17.1 to 23 wt-% (Pt/TiC-1600) upon sintering at 900 °C. Thus, it stands to reason that a loss of surface groups may be responsible for the increased platinum loading.

Table 5.3: Platinum particle diameter from XRD measurements and platinum loading from ICP-OES for the catalysts Pt/TiC-1300 and Pt/TiC-1600 before and after thermal sintering at varying temperatures.

Catalyst	Treatment	Pt Particle Diameter / nm	Pt Loading / wt-%
Pt/TiC-1300	unsintered	3.03	20.4
	400 °C	2.44	
	500 °C	2.53	
	600 °C	2.62	22.3
	700 °C	3.04	
	800 °C	4.96	
	900 °C	4.40	22.1
Pt/TiC-1600	unsintered	5.91	17.1
	400 °C	6.34	
	500 °C	5.75	
	600 °C	6.32	22.6
	700 °C	7.13	
	800 °C	8.32	
	900 °C	9.03	23.3

Figure 5.22a illustrates the electrochemical surface areas of the four examined catalysts before and after thermal sintering with respect to the sintering temperature. Due to the increasing platinum particle size, the ECSA is generally decreasing with increasing sintering temperature with Pt/ZrC-1400 sintered at 600 °C as an apparent outlier. The mass specific activity in the oxygen reduction reaction is decreasing with increasing sintering temperature for the catalysts Pt/TiC-1600 and Pt/ZrC-1500 which are based on highly crystalline CDCs (see figure 5.22b). For the other two catalysts, based on CDCs where the transition is thought to be incomplete, a different trend with increasing sintering temperature is observed: the MSA is increasing up to a maximum of 0.33 A mg⁻¹ at 600 °C and decreases at higher sintering temperatures with Pt/ZrC-1300 sintered at 600 °C constituting the outlier again. Taking into account the platinum particle sizes from table 5.3, the maximum activity is found around a particle diameter of 3 nm and the activity decreases from that point on with increasing particle size. Pt/TiC-1600 and Pt/ZrC-1500 exceed that platinum particle diameter even before the sintering and thus only show decreasing activity after thermal presintering. It shows, that the initial platinum particles have to be small enough to see a positive effect on the activity from the sintering procedure.

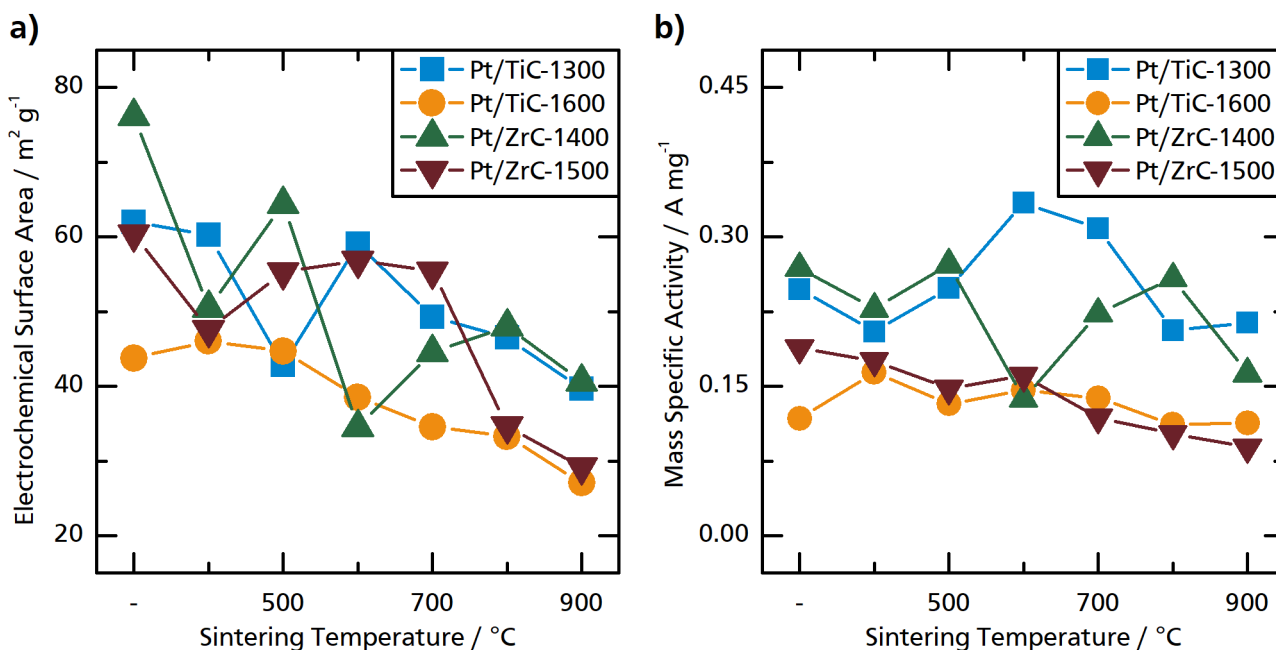


Figure 5.22: Influence of sintering temperature on **a)** electrochemical surface area, and **b)** mass specific activity for the catalysts Pt/TiC-1300, Pt/TiC-1600, Pt/ZrC-1400, and Pt/ZrC-1500.

The most important aspect of thermal presintering is the desire to increase the stability of the platinum particles by (i) increasing their size and (ii) confine them inside the carbon pore structure [65, 66]. Therefore, accelerated durability tests were conducted in the potential ranges 0.6 - 1.1 V and 0.6 - 1.4 V. Figure 5.23 summarizes the relative ECSA after the stability tests for all examined catalysts. It can be seen, that the stability generally increases with increasing sintering temperature for both potential ranges. For example Pt/ZrC-1400 exhibits only 66 % of its initial ECSA after 5000 cycles at 0.6 - 1.1 V without presintering, which was increased to 88 % after thermal presintering at 900 °C. Under the harsher conditions, the relative ECSA increased from 23 to 32 %. Whether this increased stability only results from the increased platinum particle size or an additional stabilization via pore confinement took place cannot be distinguished from these data sets. The relative mass specific activity of the materials is presented in the appendix (figure C.4). For the materials with highly crystalline CDC supports (Pt/TiC-1600, Pt/ZrC-1500), the relative MSA is generally independent of the presintering process although the values are fluctuating. This shows, that the ORR activity is hard to measure with these hydrophobic materials resulting in very low activities. Furthermore, the quality of the catalyst film on the working electrode has a more pronounced effect on the measured catalyst activity than on other catalyst characteristics like the ECSA [194]. Nevertheless, a slight increase in relative MSA can be seen for the other two catalysts at the highest sintering temperatures.

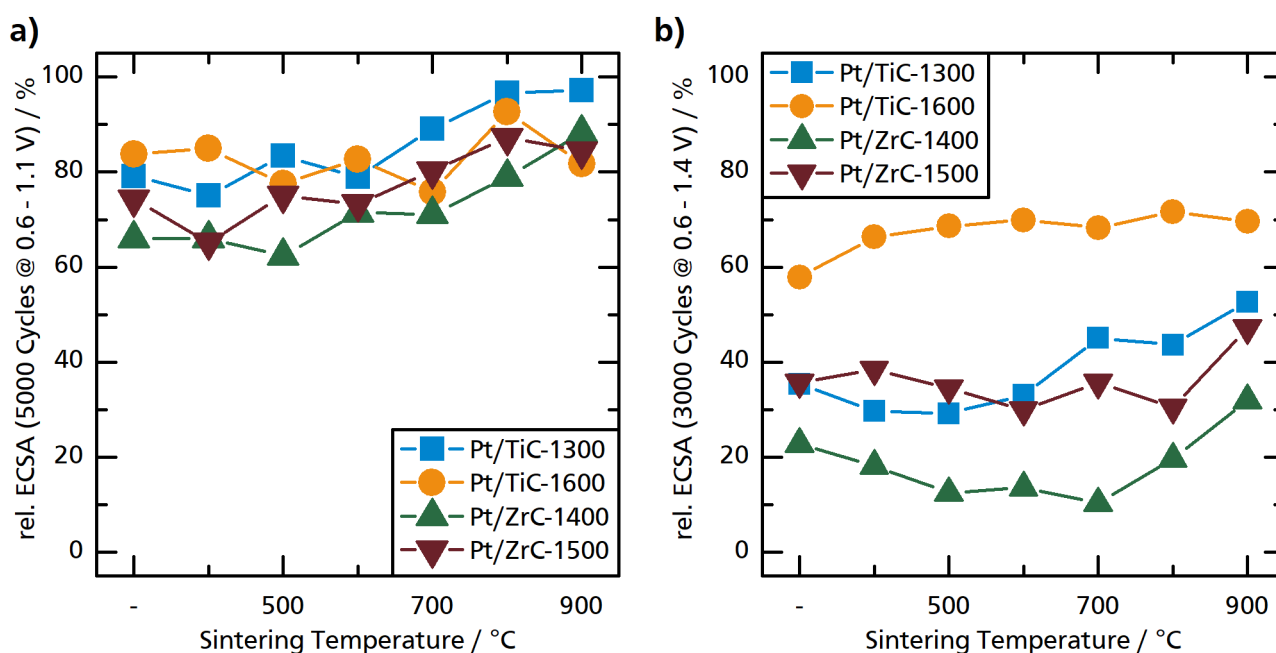


Figure 5.23: Influence of sintering temperature on relative electrochemical surface area after accelerated durability tests with **a)** 5000 cycles at 0.6 - 1.1 V, and **b)** 3000 cycles at 0.6 - 1.4 V for the catalysts Pt/TiC-1300, Pt/TiC-1600, Pt/ZrC-1400, and Pt/ZrC-1500.

5.3.3 Conclusion

In conclusion, it could be shown, that the prepared carbide-derived carbons represent suitable materials to investigate the influence of the carbonaceous support on the characteristics of platinum catalysts for the oxygen reduction reaction. A broad range of properties can be covered with the prepared CDCs and platinum depositions via an incipient wetness methods gives the desired platinum loading with particle sizes varying with the specific surface area of the carbonaceous material. CDCs with extremely high structural order like VC-CDC-1600 may not have enough SSA to ensure a good dispersion of the platinum while extremely microporous materials like ZrC-CDC-1000 might show limitations regarding the full accessibility of their porous structure. Materials in-between with a combination of crystalline and amorphous domains seem to be suited as support materials and show an increasing stability with increasing structural order. The stability can be further increased via thermal presintering to increase the size of the platinum particles. In this work, the quality of the catalyst film on the working electrode was not fully optimized as it was more focused on the proof of concept and thus the comparability of the films for all examined carbonaceous support materials (compare experimental section 4.3.2). In order to fully exploit the possibilities of CDCs as support material, the process of depositing the catalyst onto the working electrode has to be improved and strategies to determine the activities for highly hydrophobic materials more accurately have to be employed. Furthermore, the deposition of smaller platinum particles has to be investigated in order to apply thermal presintering for an increased stability via pore confinement which is out of the scope of this work.

6 Conclusion

In this work, crystalline and mesoporous carbonaceous materials were studied in order to obtain specialized materials with properties that can be adjusted to the demands of various applications. Two synthesis routes were examined and the influences of synthesis parameters on the resulting carbon structure were investigated. In one route, commercial activated carbons were subject to a high temperature vacuum annealing. By increasing the annealing temperature, carbonaceous materials with increased structural order were obtained. The process was able to increase the thermooxidative stability of the activated carbon significantly, as evidenced by an increase of the onset of oxidation from 388 °C for the pristine activated carbon *Darco KB-G* up to 596 °C after annealing at 1900 °C. Simultaneously, the specific surface area decreased drastically due to the changes in the carbon structure. With annealing at the highest temperature, a crystalline and mesoporous carbonaceous material could be obtained from the previously amorphous and microporous commercial activated carbon. Thus, the annealing temperature can be seen as a tuning parameter to obtain materials with structures in-between these two extremes. Furthermore, it was found that the choice of activated carbon precursor does not influence the obtained structural order of the resulting carbonaceous material as much. Nevertheless, the textural properties of the annealed carbonaceous materials are strongly influenced by the existing pore structure of the precursor material. Thus, vacuum annealing of commercially activated carbons presents a suitable method to obtain mesoporous and crystalline carbonaceous materials. Their properties can be controlled via the annealing process to an extent, but no strong correlation could be found to the precursor structure limiting the predictability of the resulting carbon from the annealing of a newly applied activated carbon.

An alternative pathway is the chlorination of metal carbides at elevated temperatures. In this work, different carbides were used to obtain carbide-derived carbons at temperatures up to 1600 °C in order to understand the interplay between synthesis temperature and carbide precursor in influencing the resulting carbon structure. For carbides with sodium chloride type crystal structures, a correlation was found involving the lattice constants of the carbides. They all yield amorphous material with a mesoporous structure in a low temperature regime and highly crystalline materials with mesoporous or even macroporous structures in a high temperature regime. The transition is rather sharp and takes place at a different temperatures for all examined carbide precursors. In order to describe this transition, the so-called 'transition temperature' was introduced, which directly correlates to the lattice constants of the carbides and thus the carbon to carbon distance in sodium chloride structures. Presumably, the larger the initial carbon to carbon distance, the more energy, and thus higher temperature, is needed for the atoms to rearrange with the interplanar distance characteristic for

graphite. Furthermore, an additional carbide with a different crystal structure (SiC) did not show the same transition. Noticeably, the carbon to carbon distance in silicon carbide is smaller than the interplanar distance in graphite. Presumably, for carbides with more complex structures involving small lattice constants, graphitic domains are only formed after the metal extraction due to thermal rearrangement of the carbon atoms. For carbides exhibiting sodium chloride type structures, the graphitic domains could arise directly during the initial CDC formation and thus a generally higher structural order is possible to be obtained from these precursors. This work is a further step to the utilization of carbide-derived carbons as tailor-made model materials for specialized applications.

One of such applications is as support material for platinum catalysts employed in the oxygen reduction reaction in fuel cells. For this, 18 different CDCs were selected to be loaded with platinum particles. With this amount of CDCs, a broad range of different property combinations could be covered in the following investigation. While extremely crystalline materials like VC-CDC-1600 on the one hand may exhibit not enough surface area to ensure a good dispersion of the metal, extremely microporous materials like ZrC-CDC-1000 on the other hand might have limited pore accessibility for metal and electrolyte. Nevertheless, it could be shown that the prepared CDCs in general present suitable materials to study the influence of the carbonaceous support on the resulting platinum catalysts' properties and stability. Although it was out of the scope of this work to develop suitable strategies to accurately determine activities for these highly hydrophobic materials, it was possible to demonstrate general trends. Increasing crystallinity lead to an increased stability of the catalyst which could be further enhanced by thermal presintering of the platinum particles. The specific surface area of the CDCs influenced the dispersion of the platinum on the carbon surface and thus the size of the platinum particles. With the tools presented in this work to obtain carbonaceous materials with closely controlled properties, it is possible to enhance the understanding of the role of the carbonaceous support in catalytic reactions of different kinds.

Bibliography

- [1] H. Jäger, W. Frohs, G. Collin, F. von Sturm, O. Vohler, G. Nutsch in *Ullmann's Encyclopedia of Industrial Chemistry*, Wiley-VCH Verlag GmbH & Co. KGaA., **2010**.
- [2] K. J. Sankaran, K. Haenen in *Synthesis and Application of Nanocarbons*, John Wiley & Sons, Ltd, Oxford, **2020**, pp. 1–23.
- [3] K.-D. Henning, H. von Kienle in *Ullmann's Encyclopedia of Industrial Chemistry*, Wiley-VCH Verlag GmbH & Co. KGaA., **2010**.
- [4] F. Rodríguez-Reinoso, *Carbon* **1998**, *36*, 159–175.
- [5] D. Chen, A. Holmen, Z. Sui, X. Zhou, *Chinese Journal of Catalysis* **2014**, *35*, 824–841.
- [6] R. Schlögl in *Handbook of Heterogeneous Catalysis*, Wiley-VCH Verlag GmbH & Co. KGaA., **2008**, pp. 138–264.
- [7] H. Tamai, T. Kakii, Y. Hirota, T. Kumamoto, H. Yasuda, *Chemistry of Materials* **1996**, *8*, 454–462.
- [8] M. Inagaki, M. Toyoda, Y. Soneda, S. Tsujimura, T. Morishita, *Carbon* **2016**, *107*, 448–473.
- [9] J. Janaun, N. Ellis, *Applied Catalysis A: General* **2011**, *394*, 25–31.
- [10] A. Rabis, P. Rodriguez, T. J. Schmidt, *ACS Catalysis* **2012**, *2*, 864–890.
- [11] G. He, S. Evers, X. Liang, M. Cuisinier, A. Garsuch, L. F. Nazar, *ACS Nano* **2013**, *7*, 10920–10930.
- [12] H. Wang, C. Zhang, Z. Chen, H. K. Liu, Z. Guo, *Carbon* **2015**, *81*, 782–787.
- [13] M. V. Kharlamova, D. Eder in *Synthesis and Application of Nanocarbons*, John Wiley & Sons, Ltd, Oxford, **2020**, pp. 107–147.
- [14] R. H. Baughman, A. A. Zakhidov, W. A. de Heer, *Science* **2002**, *297*, 787–792.
- [15] D. M. Bobrowska, M. E. Plonska-Brzezinska in *Synthesis and Application of Nanocarbons*, John Wiley & Sons, Ltd, Oxford, **2020**, pp. 63–105.
- [16] K. P. D. Jong, J. W. Geus, *Catalysis Reviews* **2000**, *42*, 481–510.
- [17] J. Gläsel, J. Diao, Z. Feng, M. Hilgart, T. Wolker, D. S. Su, B. J. M. Etzold, *Chemistry of Materials* **2015**, *27*, 5719–5725.
- [18] W. Qi, D. Su, *ACS Catalysis* **2014**, *4*, 3212–3218.
- [19] Y. Xia, Z. Yang, R. Mokaya, *Nanoscale* **2010**, *2*, 639–659.

-
- [20] S. Li, F. Li, J. Wang, L. Tian, H. Zhang, S. Zhang, *Nanomaterials* **2018**, *8*, 625.
- [21] M. Hartmann, A. Vinu, G. Chandrasekar, *Chemistry of Materials* **2005**, *17*, 829–833.
- [22] A. Vinu, K. Z. Hossain, G. Satish Kumar, K. Ariga, *Carbon* **2006**, *44*, 530–536.
- [23] N. Mohammadi, H. Khani, V. K. Gupta, E. Amereh, S. Agarwal, *Journal of Colloid and Interface Science* **2011**, *362*, 457–462.
- [24] A. Vinu, C. Streb, V. Murugesan, M. Hartmann, *The Journal of Physical Chemistry B* **2003**, *107*, 8297–8299.
- [25] J. Galán, A. Rodríguez, J. M. Gómez, S. J. Allen, G. M. Walker, *Chemical Engineering Journal* **2013**, *219*, 62–68.
- [26] J. H. Knox, K. K. Unger, H. Mueller, *Journal of Liquid Chromatography* **1983**, *6*, 1–36.
- [27] J. H. Knox, B. Kaur, G. R. Millward, *Journal of Chromatography A* **1986**, *352*, 3–25.
- [28] L. Pereira, *Journal of Liquid Chromatography & Related Technologies* **2008**, *31*, 1687–1731.
- [29] G. Schmidt, *Chemie in unserer Zeit* **1976**, *10*, 189–195.
- [30] T. E. Bapiro, F. M. Richards, D. I. Jodrell, *Analytical Chemistry* **2016**, *88*, 6190–6194.
- [31] C. West, C. Elfakir, M. Lafosse, *Journal of Chromatography A*, 34th International Symposium on High Performance Liquid Phase Separations and Related Techniques **2010**, *1217*, 3201–3216.
- [32] P. Chaimbault, K. Petritis, C. Elfakir, M. Dreux, *Journal of Chromatography A* **2000**, *870*, 245–254.
- [33] M. Ibanez, Y. Pico, J. Manes, *Chromatographia* **1997**, *45*, 402–407.
- [34] M. Wiener, G. Reichenauer, S. Braxmeier, F. Hemberger, H.-P. Ebert, *International Journal of Thermophysics* **2009**, *30*, 1372–1385.
- [35] Z. X. Yang, Y. D. Xia, R. Mokaya, *Advanced Materials* **2004**, *16*, 727–732.
- [36] A. J. Bard, L. R. Faulkner, *Electrochemical Methods: Fundamentals and Applications*, 2nd edition, John Wiley & Sons, Ltd, New York, **2001**.
- [37] S. Li, B. Jin, X. Zhai, H. Li, Q. Jiang, *ChemistrySelect* **2018**, *3*, 2245–2260.
- [38] X. Ji, K. T. Lee, L. F. Nazar, *Nature Materials* **2009**, *8*, 500–506.
- [39] A. Burke, *Electrochimica Acta*, 57th Annual Meeting of the International Society of Electrochemistry **2007**, *53*, 1083–1091.
- [40] M. Zeller, V. Lormann, G. Reichenauer, M. Wiener, J. Pflaum, *Advanced Energy Materials* **2012**, *2*, 598–605.
- [41] M. Wiener, G. Reichenauer, *Microporous and Mesoporous Materials* **2015**, *203*, 116–122.
- [42] W. Gao, Y. Wan, Y. Dou, D. Zhao, *Advanced Energy Materials* **2011**, *1*, 115–123.
- [43] J. Zhang, K. Sasaki, E. Sutter, R. R. Adzic, *Science* **2007**, *315*, 220–222.
- [44] Y. Shao, G. Yin, Y. Gao, *Journal of Power Sources* **2007**, *171*, 558–566.

-
- [45] H. Chen, X. Zhao, T. Zhang, P. Pei, *Energy Conversion and Management* **2019**, *182*, 282–298.
- [46] T. Zhang, P. Wang, H. Chen, P. Pei, *Applied Energy* **2018**, *223*, 249–262.
- [47] P. Pei, H. Chen, *Applied Energy* **2014**, *125*, 60–75.
- [48] M. K. Debe, *Nature* **2012**, *486*, 43.
- [49] J. C. Meier, C. Galeano, I. Katsounaros, J. Witte, H. J. Bongard, A. A. Topalov, C. Baldizzone, S. Mezzavilla, F. Schüth, K. J. J. Mayrhofer, *Beilstein Journal of Nanotechnology* **2014**, *5*, 44–67.
- [50] J. C. Meier, C. Galeano, I. Katsounaros, A. A. Topalov, A. Kostka, F. Schüth, K. J. J. Mayrhofer, *ACS Catalysis* **2012**, *2*, 832–843.
- [51] L. M. Roen, C. H. Paik, T. D. Jarvi, *Electrochemical and Solid-State Letters* **2003**, *7*, A19.
- [52] H. Schulenburg, B. Schwanitz, N. Linse, G. G. Scherer, A. Wokaun, J. Krbanjevic, R. Grothausmann, I. Manke, *The Journal of Physical Chemistry C* **2011**, *115*, 14236–14243.
- [53] B. Y. Xia, J. N. Wang, S. J. Teng, X. X. Wang, *Chemistry – A European Journal* **2010**, *16*, 8268–8274.
- [54] F. Coloma, A. Sepulveda-Escribano, F. Rodriguez-Reinoso, *Journal of Catalysis* **1995**, *154*, 299–305.
- [55] D. A. Stevens, M. T. Hicks, G. M. Haugen, J. R. Dahn, *Journal of The Electrochemical Society* **2005**, *152*, A2309.
- [56] Y. Shao-Horn, W. C. Sheng, S. Chen, P. J. Ferreira, E. F. Holby, D. Morgan, *Topics in Catalysis* **2007**, *46*, 285–305.
- [57] K. N. Sultana, D. Worku, M. T. Z. Hossain, S. Ilias, *Fuel Cells* **2019**, *19*, 27–34.
- [58] E. Antolini, *Applied Catalysis B: Environmental* **2009**, *88*, 1–24.
- [59] P. V. Shanahan, L. Xu, C. Liang, M. Waje, S. Dai, Y. S. Yan, *Journal of Power Sources* **2008**, *185*, 423–427.
- [60] F. Su, J. Zeng, X. Bao, Y. Yu, J. Y. Lee, X. S. Zhao, *Chemistry of Materials* **2005**, *17*, 3960–3967.
- [61] Y. H. Ng, S. Ikeda, T. Harada, T. Sakata, H. Mori, A. Takaoka, M. Matsumura, *Langmuir* **2008**, *24*, 6307–6312.
- [62] F. Schüth, *Chemistry of Materials* **2014**, *26*, 423–434.
- [63] J. Knossalla, P. Paciok, D. Göhl, D. Jalalpoor, E. Pizzutilo, A. M. Mingers, M. Heggen, R. E. Dunin-Borkowski, K. J. J. Mayrhofer, F. Schüth, M. Ledendecker, *Journal of the American Chemical Society* **2018**, *140*, 15684–15689.
- [64] Z. Gan, C. Shu, C. Deng, W. Du, B. Huang, W. Tang, *Nanoscale* **2021**.
- [65] C. Galeano, J. C. Meier, V. Peinecke, H. Bongard, I. Katsounaros, A. A. Topalov, A. Lu, K. J. J. Mayrhofer, F. Schüth, *Journal of the American Chemical Society* **2012**, *134*, 20457–20465.
- [66] C. Yang, M. Zhou, Q. Xu, *Nanoscale* **2014**, *6*, 11863–11870.
- [67] C. Liang, Z. Li, S. Dai, *Angewandte Chemie International Edition* **2008**, *47*, 3696–3717.

-
- [68] J. Pang, A. Wang, M. Zheng, Y. Zhang, Y. Huang, X. Chen, T. Zhang, *Green Chemistry* **2012**, *14*, 614–617.
- [69] N. Ji, T. Zhang, M. Zheng, A. Wang, H. Wang, X. Wang, J. G. Chen, *Angewandte Chemie International Edition* **2008**, *47*, 8510–8513.
- [70] H. Kobayashi, T. Komanoya, K. Hara, A. Fukuoka, *ChemSusChem* **2010**, *3*, 440–443.
- [71] K. Zaghbi, X. Song, K. Kinoshita, *Thermochimica Acta* **2001**, *371*, 57–64.
- [72] R. T. Yang, C. Wong, *The Journal of Chemical Physics* **1981**, *75*, 4471–4476.
- [73] R. T. Yang, C. Wong, *Science* **1981**, *214*, 437–438.
- [74] F. Coloma, A. Sepulveda-Escribano, J. L. G. Fierro, F. Rodriguez-Reinoso, *Langmuir* **1994**, *10*, 750–755.
- [75] M. Kang, Y.-S. Bae, C.-H. Lee, *Carbon* **2005**, *43*, 1512–1516.
- [76] H. Xu, Y. Liu, G. Sun, S. Kang, Y. Wang, Z. Zheng, X. Li, *Materials Letters* **2019**, *244*, 123–125.
- [77] S.-H. Chai, V. Schwartz, J. Y. Howe, X. Wang, M. Kidder, S. H. Overbury, S. Dai, D.-E. Jiang, *Microporous and Mesoporous Materials* **2013**, *170*, 141–149.
- [78] S.-H. Chai, J. Y. Howe, X. Wang, M. Kidder, V. Schwartz, M. L. Golden, S. H. Overbury, S. Dai, D.-E. Jiang, *Carbon* **2012**, *50*, 1574–1582.
- [79] Y. Zhao, S. Huang, L. Wei, Y. Zhang, A. Lin, C. Liu, J. Li, *Industrial & Engineering Chemistry Research* **2020**, *59*, 3279–3286.
- [80] D. S. Su, J. Zhang, B. Frank, A. Thomas, X. Wang, J. Paraknowitsch, R. Schlögl, *ChemSusChem* **2010**, *3*, 169–180.
- [81] E. Lam, J. H. Luong, *ACS Catalysis* **2014**, *4*, 3393–3410.
- [82] F. Herold, S. Prosch, N. Oefner, K. Brunnengräber, O. Leubner, Y. Hermans, K. Hofmann, A. Drochner, J. P. Hofmann, W. Qi, B. J. M. Etzold, *Angewandte Chemie International Edition* **2021**, *60*, 5898–5906.
- [83] D. S. Su, J. J. Delgado, X. Liu, D. Wang, R. Schlögl, L. Wang, Z. Zhang, Z. Shan, F.-S. Xiao, *Chemistry – An Asian Journal* **2009**, *4*, 1108–1113.
- [84] V. Schwartz, H. Xie, H. M. Meyer, S. H. Overbury, C. Liang, *Carbon* **2011**, *49*, 659–668.
- [85] D. S. Su, S. Perathoner, G. Centi, *Chemical Reviews* **2013**, *113*, 5782–5816.
- [86] J. Luo, H. Yu, H. Wang, H. Wang, F. Peng, *Chemical Engineering Journal* **2014**, *240*, 434–442.
- [87] H. Yu, F. Peng, J. Tan, X. Hu, H. Wang, J. Yang, W. Zheng, *Angewandte Chemie International Edition* **2011**, *50*, 3978–3982.
- [88] J. Luo, F. Peng, H. Yu, H. Wang, W. Zheng, *ChemCatChem* **2013**, *5*, 1578–1586.
- [89] A. Villa, J.-P. Tessonier, O. Majoulet, D. S. Su, R. Schlögl, *Chemical Communications* **2009**, 4405–4407.
- [90] X. Zhao, J. Wang, C. Chen, Y. Huang, A. Wang, T. Zhang, *Chemical Communications* **2014**, *50*, 3439–3442.

-
- [91] X. Sun, R. Wang, D. Su, *Chinese Journal of Catalysis* **2013**, *34*, 508–523.
- [92] D. S. Su, G. Wen, S. Wu, F. Peng, R. Schlögl, *Angewandte Chemie International Edition* **2017**, *56*, 936–964.
- [93] H. Christians, K. Brunnengräber, J. Gläsel, B. J. M. Etzold, *Carbon* **2021**, *175*, 215–222.
- [94] D. Yuan, X. Yuan, W. Zou, F. Zeng, X. Huang, S. Zhou, *Journal of Materials Chemistry* **2012**, *22*, 17820–17826.
- [95] L. Zhang, X. Yang, F. Zhang, G. Long, T. Zhang, K. Leng, Y. Zhang, Y. Huang, Y. Ma, M. Zhang, Y. Chen, *Journal of the American Chemical Society* **2013**, *135*, 5921–5929.
- [96] L. Estevez, V. Prabhakaran, A. L. Garcia, Y. Shin, J. Tao, A. M. Schwarz, J. Darsell, P. Bhattacharya, V. Shutthanandan, J.-G. Zhang, *ACS Nano* **2017**, *11*, 11047–11055.
- [97] M. Thommes, K. Kaneko, A. V. Neimark, J. P. Olivier, F. Rodriguez-Reinoso, J. Rouquerol, K. S. Sing, *Pure and Applied Chemistry* **2015**, *87*, 1051–1069.
- [98] K. S. W. Sing, *Pure and Applied Chemistry* **1985**, *57*, 603–619.
- [99] H. Marsh, F. Rodriguez-Reinoso, *Activated Carbon*, Elsevier Science, **2006**.
- [100] Z. Hu, M. P. Srinivasan, Y. Ni, *Advanced Materials* **2000**, *12*, 62–65.
- [101] A. Oya, S. Yoshida, J. Alcaniz-Monge, A. Linares-Solano, *Carbon* **1995**, *33*, 1085–1090.
- [102] T. Kyotani, *Carbon* **2000**, *38*, 269–286.
- [103] R. W. Pekala, C. T. Alviso, F. M. Kong, S. S. Hulsey, *Journal of Non-Crystalline Solids* **1992**, *145*, 90–98.
- [104] H. Tamon, H. Ishizaka, T. Yamamoto, T. Suzuki, *Carbon* **1999**, *37*, 2049–2055.
- [105] C. Moreno-Castilla, F. J. Maldonado-Hódar, *Carbon* **2005**, *43*, 455–465.
- [106] N. Yoshizawa, H. Hatori, Y. Soneda, Y. Hanzawa, K. Kaneko, M. S. Dresselhaus, *Journal of Non-Crystalline Solids* **2003**, *330*, 99–105.
- [107] Y. Hanzawa, K. Kaneko, R. W. Pekala, M. S. Dresselhaus, *Langmuir* **1996**, *12*, 6167–6169.
- [108] H. Steldinger, A. Esposito, K. Brunnengräber, J. Gläsel, B. J. M. Etzold, *Advanced Science* **2019**, *6*, 1901340.
- [109] A. B. Fuertes, T. A. Centeno, *Journal of Materials Chemistry* **2005**, *15*, 1079–1083.
- [110] T. Kyotani, *Bulletin of the Chemical Society of Japan* **2006**, *79*, 1322–1337.
- [111] J. Lee, S. Yoon, T. Hyeon, S. M. Oh, K. B. Kim, *Chemical Communications* **1999**, *0*, 2177–2178.
- [112] R. Ryoo, S. H. Joo, S. Jun, *The Journal of Physical Chemistry B* **1999**, *103*, 7743–7746.
- [113] W. Guo, F. Su, X. S. Zhao, *Carbon* **2005**, *43*, 2423–2426.
- [114] J. Jang, B. Lim, *Advanced Materials* **2002**, *14*, 1390–1393.
- [115] Z. Li, M. Jaroniec, *Carbon* **2001**, *39*, 2080–2082.

-
- [116] J. Lee, K. Sohn, T. Hyeon, *Journal of the American Chemical Society* **2001**, *123*, 5146–5147.
- [117] Y. Oda, K. Fukuyama, K. Nishikawa, S. Namba, H. Yoshitake, T. Tatsumi, *Chemistry of Materials* **2004**, *16*, 3860–3866.
- [118] T. Kyotani, L.-f. Tsai, A. Tomita, *Chemistry of Materials* **1995**, *7*, 1427–1428.
- [119] J. Li, M. Moskovits, T. L. Haslett, *Chemistry of Materials* **1998**, *10*, 1963–1967.
- [120] T. F. Baumann, J. H. Satcher, *Chemistry of Materials* **2003**, *15*, 3745–3747.
- [121] Y. Wan, Y. Shi, D. Zhao, *Chemistry of Materials* **2008**, *20*, 932–945.
- [122] L. Chuenchom, R. Kraehnert, B. M. Smarsly, *Soft Matter* **2012**, *8*, 10801–10812.
- [123] C. Liang, S. Dai, *Journal of the American Chemical Society* **2006**, *128*, 5316–5317.
- [124] Y. Meng, D. Gu, F. Zhang, Y. Shi, L. Cheng, D. Feng, Z. Wu, Z. Chen, Y. Wan, A. Stein, D. Zhao, *Chemistry of Materials* **2006**, *18*, 4447–4464.
- [125] Y. Meng, D. Gu, F. Zhang, Y. Shi, H. Yang, Z. Li, C. Yu, B. Tu, D. Zhao, *Angewandte Chemie International Edition* **2005**, *44*, 7053–7059.
- [126] V. Presser, M. Heon, Y. Gogotsi, *Advanced Functional Materials* **2011**, *21*, 810–833.
- [127] S. Urbonaite, L. Hålldahl, G. Svensson, *Carbon* **2008**, *46*, 1942–1947.
- [128] J. N. Andersen (Stauffer Chemical Co), *US Pat.*, 2739041 A, **1956**.
- [129] R. A. Gonzalez, C. D. Musick, J. N. Tilton (E. I. Du Pont De Nemours And Company), *US Pat.*, 5508015 A, **1996**.
- [130] J. C. Deberry, M. Robinson, M. D. Pomponi, A. J. Beach, Y. Xiong, K. Akhtar (Millennium Inorganic Chemicals, Inc.), *US Pat.*, 6387347 B1, **2002**.
- [131] T.-H. Wang, A. M. Navarrete-López, S. Li, D. A. Dixon, J. L. Gole, *The Journal of Physical Chemistry A* **2010**, *114*, 7561–7570.
- [132] M. Lätt, M. Käärik, L. Permann, H. Kuura, M. Arulepp, J. Leis, *Journal of Solid State Electrochemistry* **2010**, *14*, 543–548.
- [133] R. K. Dash, A. Nikitin, Y. Gogotsi, *Microporous and Mesoporous Materials* **2004**, *72*, 203–208.
- [134] S. Urbonaite, S. Wachtmeister, C. Mirguet, E. Coronel, W. Y. Zou, S. Csillag, G. Svensson, *Carbon* **2007**, *45*, 2047–2053.
- [135] S. Urbonaite, J. M. Juárez-Galán, J. Leis, F. Rodríguez-Reinoso, G. Svensson, *Microporous and Mesoporous Materials* **2008**, *113*, 14–21.
- [136] A. Jänes, T. Thomberg, H. Kurig, E. Lust, *Carbon* **2009**, *47*, 23–29.
- [137] D. Ávila-Brandé, N. A. Katcho, E. Urones-Garrote, A. Gómez-Herrero, A. R. Landa-Cánovas, L. C. Otero-Díaz, *Carbon* **2006**, *44*, 753–761.
- [138] T. X. Nguyen, J.-S. Bae, S. K. Bhatia, *Langmuir* **2009**, *25*, 2121–2132.

-
- [139] A. Silvestre-Albero, S. Rico-Francés, F. Rodríguez-Reinoso, A. M. Kern, M. Klumpp, B. J. M. Etzold, J. Silvestre-Albero, *Carbon* **2013**, *59*, 221–228.
- [140] A. Jänes, T. Thomberg, E. Lust, *Carbon* **2007**, *45*, 2717–2722.
- [141] I. Tallo, T. Thomberg, K. Kontturi, A. Jänes, E. Lust, *Carbon* **2011**, *49*, 4427–4433.
- [142] R. K. Dash, G. Yushin, Y. Gogotsi, *Microporous and Mesoporous Materials* **2005**, *86*, 50–57.
- [143] E. N. Hoffman, G. Yushin, T. El-Raghy, Y. Gogotsi, M. W. Barsoum, *Microporous and Mesoporous Materials* **2008**, *112*, 526–532.
- [144] E. N. Hoffman, G. Yushin, M. W. Barsoum, Y. Gogotsi, *Chemistry of Materials* **2005**, *17*, 2317–2322.
- [145] C. Portet, D. Kazachkin, S. Osswald, Y. Gogotsi, E. Borguet, *Thermochimica Acta* **2010**, *497*, 137–142.
- [146] G. Laudisio, R. K. Dash, J. P. Singer, G. Yushin, Y. Gogotsi, J. E. Fischer, *Langmuir* **2006**, *22*, 8945–8950.
- [147] A. Lee, R. Zhu, M. McNallan, *Journal of Physics: Condensed Matter* **2006**, *18*, S1763.
- [148] P. Becker, F. Glenk, M. Kormann, N. Popovska, B. J. M. Etzold, *Chemical Engineering Journal* **2010**, *159*, 236–241.
- [149] T. Knorr, F. Strobl, F. Glenk, B. J. M. Etzold, *Chemical Engineering & Technology* **2012**, *35*, 1495–1503.
- [150] T. Knorr, M. Kaiser, F. Glenk, B. J. M. Etzold, *Chemical Engineering Science* **2012**, *69*, 492–502.
- [151] Y. G. Gogotsi, I.-D. Jeon, M. J. McNallan, *Journal of Materials Chemistry* **1997**, *7*, 1841–1848.
- [152] Y. Gogotsi, A. Nikitin, H. Ye, W. Zhou, J. E. Fischer, B. Yi, H. C. Foley, M. W. Barsoum, *Nature Materials* **2003**, *2*, 591–594.
- [153] Z. G. Cambaz, G. N. Yushin, Y. Gogotsi, K. L. Vyshnyakova, L. N. Pereselentseva, *Journal of the American Ceramic Society* **2006**, *89*, 509–514.
- [154] A. E. Kravchik, J. A. Kukushkina, V. V. Sokolov, G. F. Tereshchenko, *Carbon* **2006**, *44*, 3263–3268.
- [155] A. E. Kravchik, Y. A. Kukushkina, V. V. Sokolov, G. F. Tereshchenko, E. A. Ustinov, *Russian Journal of Applied Chemistry* **2008**, *81*, 1733–1739.
- [156] O. Vohler, F. von Sturm, E. Wege, G. Nutsch in *Ullmann's Encyclopedia of Industrial Chemistry*, Wiley-VCH Verlag GmbH & Co. KGaA., **2010**, pp. 703–720.
- [157] W. Frohs, F. von Sturm, E. Wege, G. Nutsch, W. Handl in *Ullmann's Encyclopedia of Industrial Chemistry*, Wiley-VCH Verlag GmbH & Co. KGaA., **2010**, pp. 721–730.
- [158] R. E. Franklin, *Proc. R. Soc. Lond. A* **1951**, *209*, 196–218.
- [159] I. A. S. Edwards in *Introduction to Carbon Science*, Butterworth-Heinemann, **1989**, pp. 1–36.
- [160] E. A. Belenkov, *Inorganic Materials* **2001**, *37*, 928–934.
- [161] T. Noda, H. Kato, *Carbon* **1965**, *3*, 289–297.
- [162] T. Noda, M. Inagaki, *Nature* **1962**, *196*, 772–772.
- [163] T. Noda, M. Inagaki, *Carbon* **1964**, *2*, 127–130.

-
- [164] T. Noda, M. Inagaki, T. Sekiya, *Carbon* **1965**, 3, 175–180.
- [165] H. Marsh, A. P. Warburton, *Journal of Applied Chemistry* **1970**, 20, 133–142.
- [166] W. E. Parker, R. W. Marek, E. M. Woodruff, *Carbon* **1965**, 2, 395–406.
- [167] C. Yokokawa, K. Hosokawa, Y. Takegami, *Carbon* **1966**, 4, 459–465.
- [168] H. Li, H. Zhang, K. Li, J. Zhang, M. Sun, B. Su, *Fuel* **2020**, 279, 118531.
- [169] E. P. Sajitha, V. Prasad, S. V. Subramanyam, S. Eto, K. Takai, T. Enoki, *Carbon* **2004**, 42, 2815–2820.
- [170] C. J. Thambiliyagodage, S. Ulrich, P. T. Araujo, M. G. Bakker, *Carbon* **2018**, 134, 452–463.
- [171] A. Ōya, H. Marsh, *Journal of Materials Science* **1982**, 17, 309–322.
- [172] M. Sevilla, A. B. Fuertes, *Carbon* **2006**, 44, 468–474.
- [173] Y. Liu, Q. Liu, J. Gu, D. Kang, F. Zhou, W. Zhang, Y. Wu, D. Zhang, *Carbon* **2013**, 64, 132–140.
- [174] D. Zhai, H. Du, B. Li, Y. Zhu, F. Kang, *Carbon* **2011**, 49, 725–729.
- [175] M. B. Vázquez-Santos, E. Geissler, K. László, J.-N. Rouzaud, A. Martínez-Alonso, J. M. Tascón, *The Journal of Physical Chemistry C* **2012**, 116, 257–268.
- [176] S. Osswald, J. Chmiola, Y. Gogotsi, *Carbon* **2012**, 50, 4880–4886.
- [177] S. Błażewicz, A. Świątkowski, B. J. Trznadel, *Carbon* **1999**, 37, 693–700.
- [178] K. Kuśmierek, A. Świątkowski, K. Skrzypczyńska, S. Błażewicz, J. Hryniewicz, *Korean Journal of Chemical Engineering* **2017**, 34, 1081–1090.
- [179] A. C. Ferrari, J. Robertson, *Physical Review B* **2000**, 61, 14095–14107.
- [180] J. Xu, R. Zhang, P. Chen, D. Shen, X. Ye, S. Ge, *Carbon* **2013**, 64, 444–455.
- [181] J. Xu, C. Wu, P. Yan, R. Zhang, X. Yue, S. Ge, *Microporous and Mesoporous Materials* **2014**, 198, 74–81.
- [182] B. E. Warren, P. Bodenstein, *Acta Crystallographica* **1965**, 18, 282–286.
- [183] Z. Liu, B. Guo, L. Hong, T. H. Lim, *Electrochemistry Communications* **2006**, 8, 83–90.
- [184] G. Bergeret, P. Gallezot in *Handbook of Heterogeneous Catalysis*, Wiley-VCH Verlag GmbH & Co. KGaA., **2008**, pp. 738–765.
- [185] P. Mallet-Ladeira, P. Puech, C. Toulouse, M. Cazayous, N. Ratel-Ramond, P. Weisbecker, G. L. Vignoles, M. Monthieux, *Carbon* **2014**, 80, 629–639.
- [186] P. Mallet-Ladeira, P. Puech, P. Weisbecker, G. L. Vignoles, M. Monthieux, *Applied Physics A* **2014**, 114, 759–763.
- [187] F. Tuinstra, J. L. Koenig, *The Journal of Chemical Physics* **1970**, 53, 1126–1130.
- [188] R. P. Vidano, D. B. Fischbach, L. J. Willis, T. M. Loehr, *Solid State Communications* **1981**, 39, 341–344.
- [189] D. S. Knight, W. B. White, *Journal of Materials Research* **1989**, 4, 385–393.
- [190] M. J. Matthews, M. A. Pimenta, G. Dresselhaus, M. S. Dresselhaus, M. Endo, *Physical Review B* **1999**, 59, R6585–R6588.

-
- [191] L. G. Cançado, K. Takai, T. Enoki, M. Endo, Y. A. Kim, H. Mizusaki, A. Jorio, L. N. Coelho, R. Magalhães-Paniago, M. A. Pimenta, *Applied Physics Letters* **2006**, *88*, 163106.
- [192] G. A. Zickler, B. Smarsly, N. Gierlinger, H. Peterlik, O. Paris, *Carbon* **2006**, *44*, 3239–3246.
- [193] H. A. Gasteiger, S. S. Kocha, B. Sompalli, F. T. Wagner, *Applied Catalysis B: Environmental* **2005**, *56*, 9–35.
- [194] Y. Garsany, O. A. Baturina, K. E. Swider-Lyons, S. S. Kocha, *Analytical Chemistry* **2010**, *82*, 6321–6328.
- [195] <https://www.cabotcorp.com/solutions/products-plus/activated-carbon/powdered>, Cabot Corporation, **2020**.
- [196] J. Ribeiro-Soares, M. E. Oliveros, C. Garin, M. V. David, L. G. P. Martins, C. A. Almeida, E. H. Martins-Ferreira, K. Takai, T. Enoki, R. Magalhães-Paniago, A. Malachias, A. Jorio, B. S. Archanjo, C. A. Achete, L. G. Cançado, *Carbon* **2015**, *95*, 646–652.
- [197] A. C. Ferrari, *Solid State Communications*, Exploring Graphene **2007**, *143*, 47–57.
- [198] <http://www.silcarbon.eu/englisch/products/activated-carbon/powder-activated-carbon/>, Silcarbon Aktivkohhle GmbH, **2020**.
- [199] Y.-J. Lee, *Journal of Nuclear Materials* **2004**, *325*, 174–179.
- [200] S. Vollebregt, R. Ishihara, F. D. Tichelaar, Y. Hou, C. I. M. Beenakker, *Carbon* **2012**, *50*, 3542–3554.
- [201] E. Riedel, C. Janiak, *Anorganische Chemie*, 7th edition, Walter de Gruyter, Berlin, New York, **2007**.
- [202] P. Ehrlich, H. Kühnl in *Handbuch Der Präparativen Anorganischen Chemie in 3 Bänden: II, Vol. 2*, Enke, Stuttgart, **1978**, pp. 1323–1398.
- [203] G. Brauer, A. Simon in *Handbuch Der Präparativen Anorganischen Chemie in 3 Bänden: III, Vol. 3*, Enke, Stuttgart, **1981**, pp. 1407–1476.
- [204] T. Kimoto, J. A. Cooper, *Fundamentals of Silicon Carbide Technology*, John Wiley & Sons, Ltd, Singapore, **2014**.
- [205] U. Müller, *Anorganische Strukturchemie*, 6th edition, Vieweg+Teubner, Wiesbaden, **2008**.
- [206] A. Kurlov, A. I. Gusev, *Tungsten Carbides*, Springer International Publishing, Heidelberg, New York, **2013**.
- [207] D. Emin, *Physics Today* **2008**, *40*, 55.

Appendix

A Activated Carbon as Precursor for Mesoporous and Crystalline Carbons

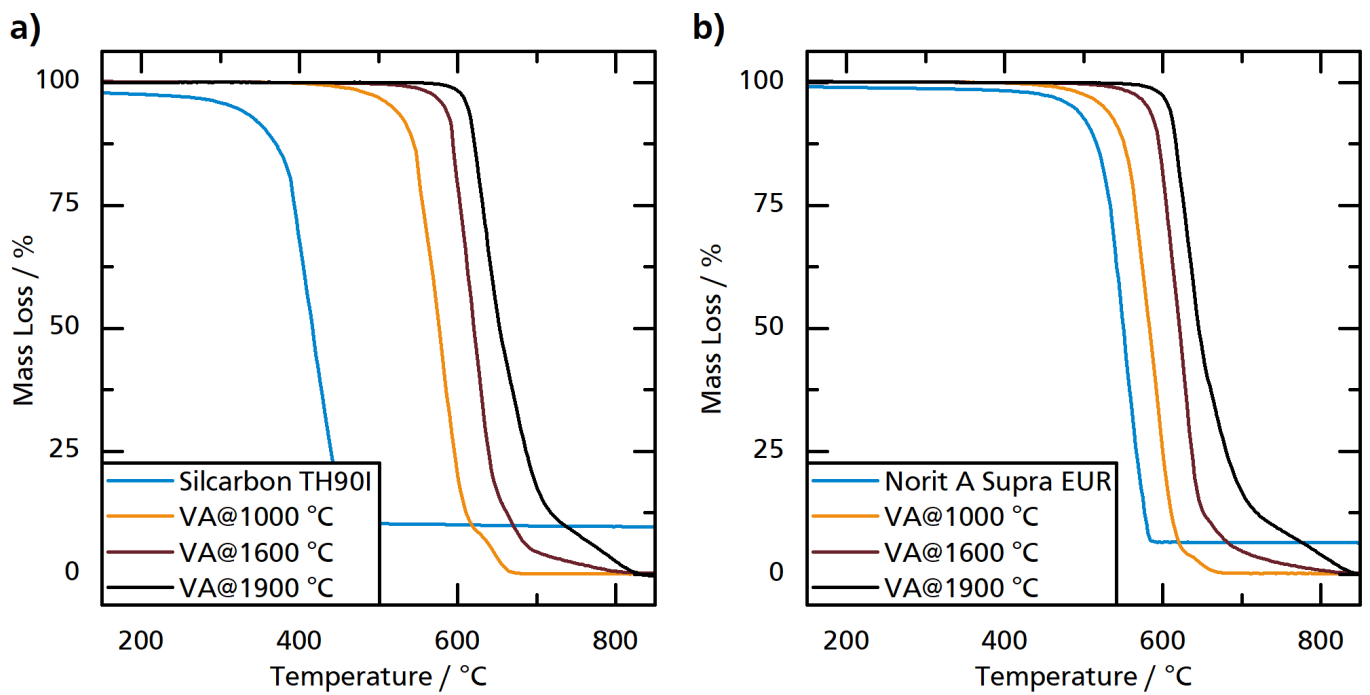


Figure A.1: Mass loss curves from temperature-programmed oxidation of **a)** *Silcarbon TH90I*, and **b)** *Norit A Supra EUR* before and after vacuum annealing at different temperatures.

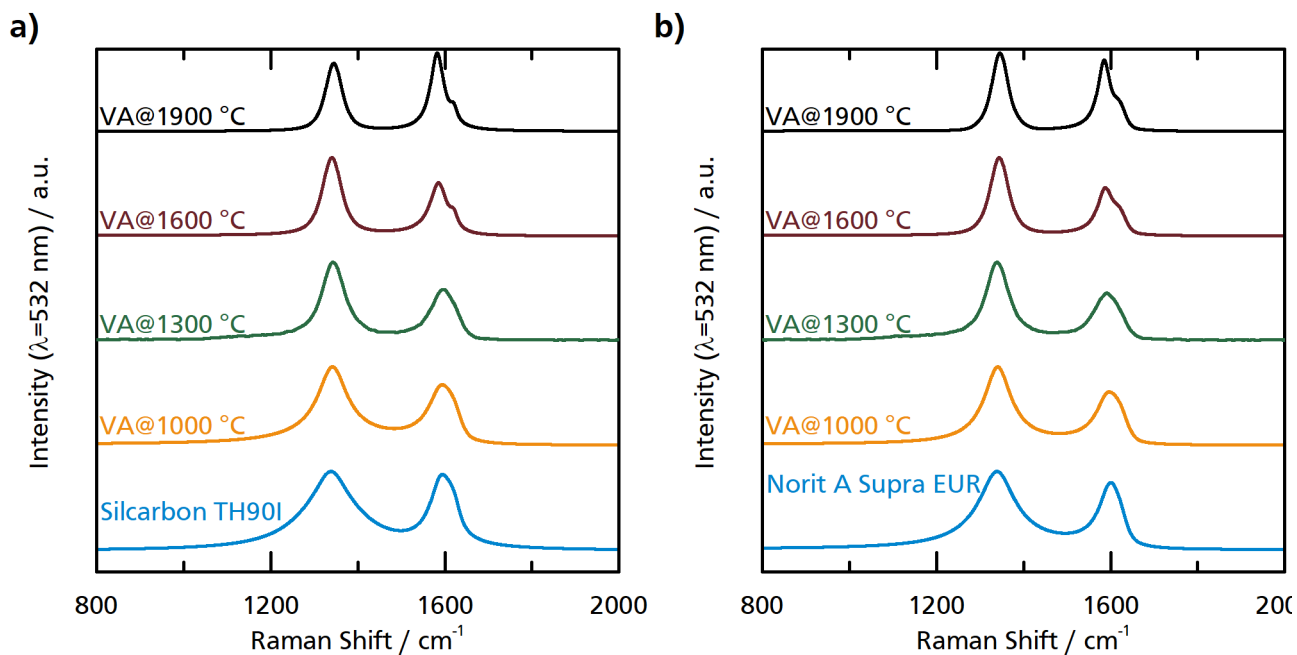


Figure A.2: Raman spectra of **a) Silcarbon TH90I**, and **b) Norit A Supra EUR** before and after vacuum annealing at different temperatures.

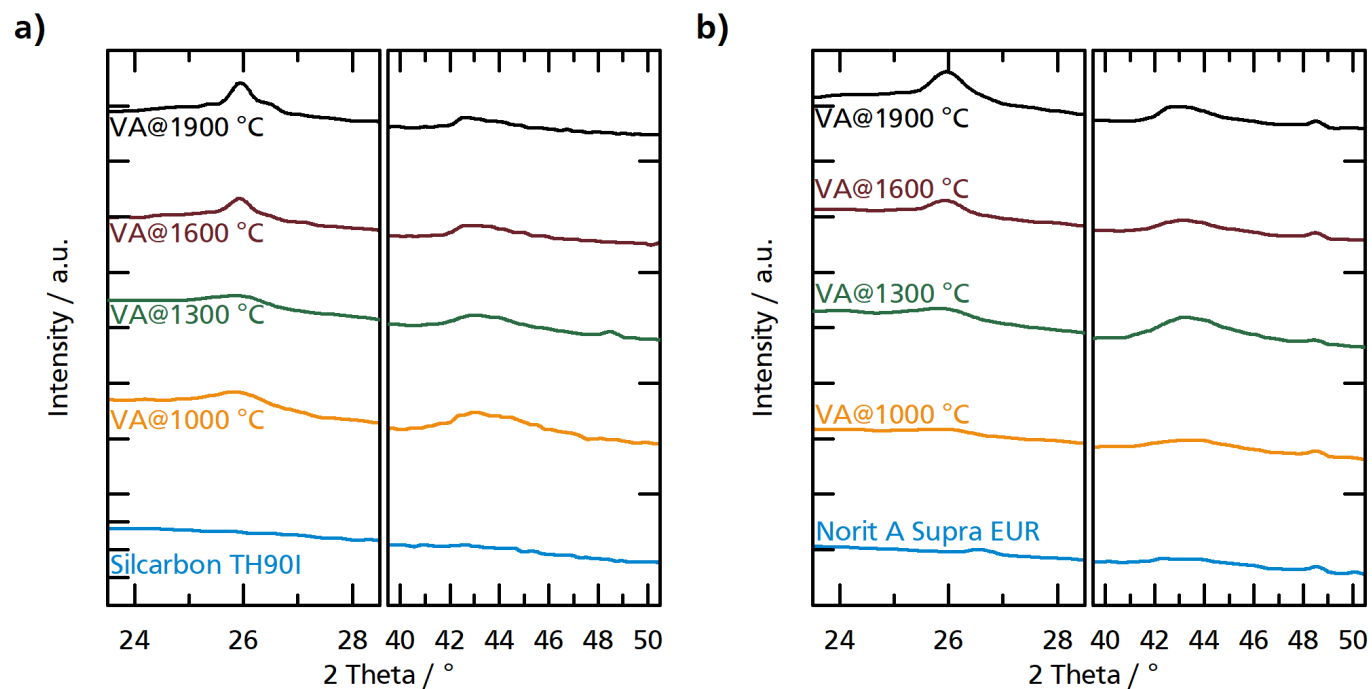


Figure A.3: X-Ray powder diffraction patterns of **a) Silcarbon TH90I**, and **b) Norit A Supra EUR** before and after vacuum annealing at different temperatures.

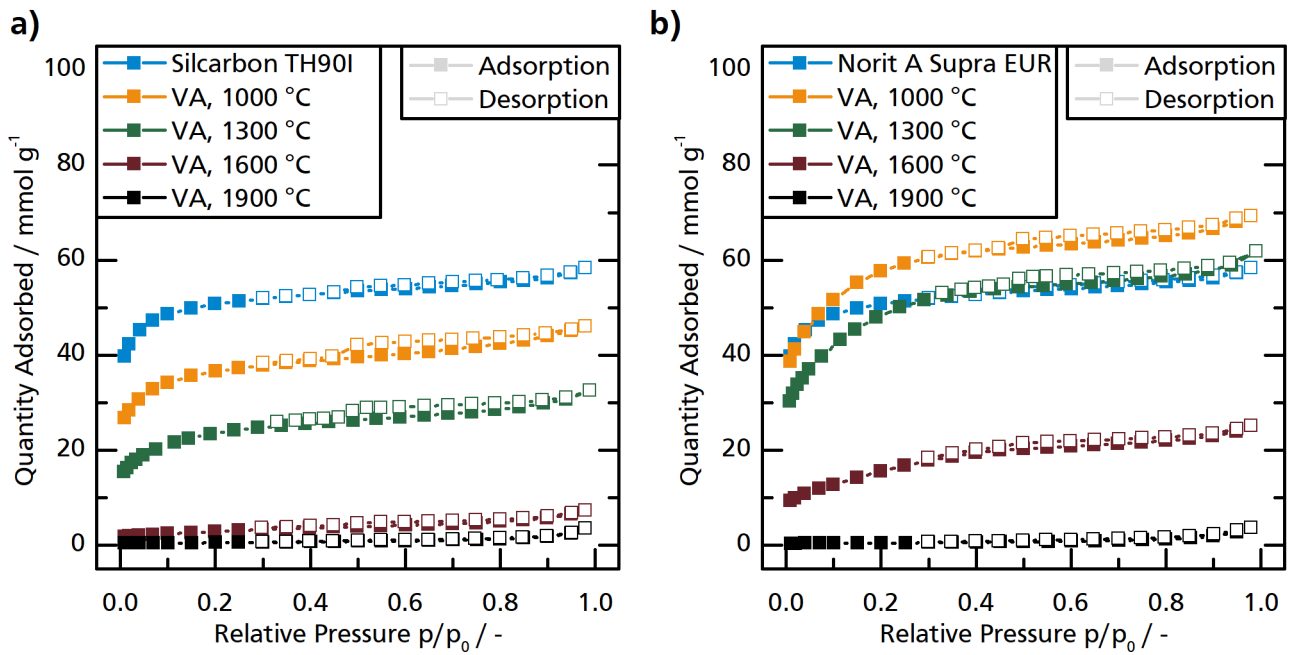


Figure A.4: Adsorption / desorption isotherms from nitrogen physisorption of **a)** *Silcarbon TH90I*, and **b)** *Norit A Supra EUR* before and after vacuum annealing at different temperatures.

B Metal Carbides as Precursor for Mesoporous and Crystalline Carbons

The complete data sets of raw characterization data are available as tab delimited text files through an open access repository provided by the Technical University of Darmstadt (TUdatalib). They are accessible via DOI:

X-Ray Powder Diffraction Data

NbC-CDC: <https://doi.org/10.25534/tudatalib-242.2>

SiC-CDC: <https://doi.org/10.25534/tudatalib-242.2>

TaC-CDC: <https://doi.org/10.25534/tudatalib-242.2>

TiC-CDC: <https://doi.org/10.25534/tudatalib-242.2>

VC-CDC: <https://doi.org/10.25534/tudatalib-246.2>

ZrC-CDC: <https://doi.org/10.25534/tudatalib-247.3>

Raman Spectroscopy Data

NbC-CDC: <https://doi.org/10.25534/tudatalib-236.2>

SiC-CDC: <https://doi.org/10.25534/tudatalib-237.2>

TaC-CDC: <https://doi.org/10.25534/tudatalib-238.2>

TiC-CDC: <https://doi.org/10.25534/tudatalib-239.2>

VC-CDC: <https://doi.org/10.25534/tudatalib-240.2>

ZrC-CDC: <https://doi.org/10.25534/tudatalib-241.3>

TPO Mass Loss Data

NbC-CDC: <https://doi.org/10.25534/tudatalib-248.2>

SiC-CDC: <https://doi.org/10.25534/tudatalib-249.2>

TaC-CDC: <https://doi.org/10.25534/tudatalib-250.2>

TiC-CDC: <https://doi.org/10.25534/tudatalib-251.2>

VC-CDC: <https://doi.org/10.25534/tudatalib-252.2>

ZrC-CDC: <https://doi.org/10.25534/tudatalib-253.3>

Argon Physisorption Data

NbC-CDC: <https://doi.org/10.25534/tudatalib-230.2>

SiC-CDC: <https://doi.org/10.25534/tudatalib-231.2>

TaC-CDC: <https://doi.org/10.25534/tudatalib-232.2>

TiC-CDC: <https://doi.org/10.25534/tudatalib-233.2>

VC-CDC: <https://doi.org/10.25534/tudatalib-234.2>

ZrC-CDC: <https://doi.org/10.25534/tudatalib-235.3>

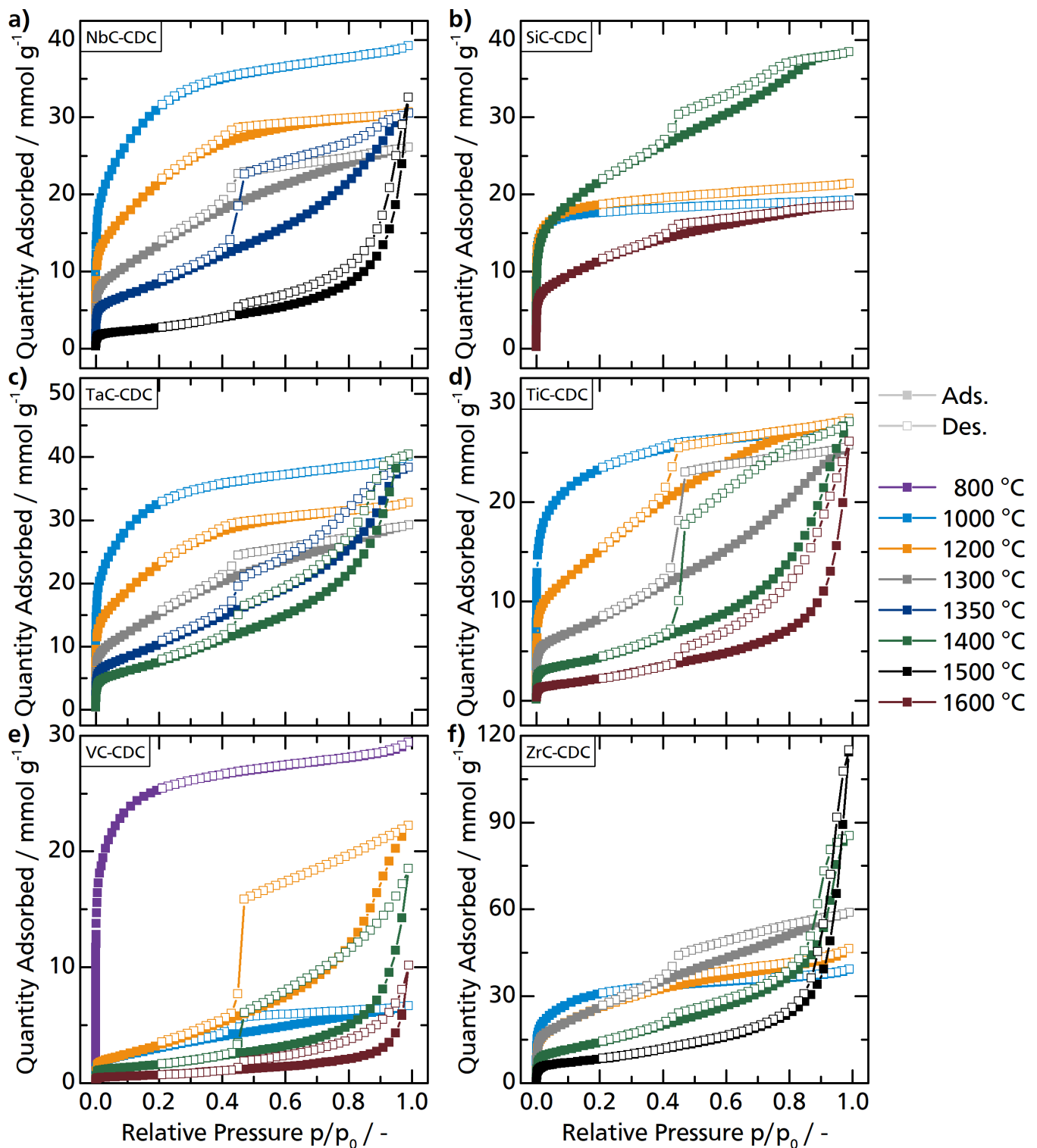


Figure B.1: Adsorption / desorption isotherms from argon physisorption of CDCs synthesized at different temperatures from the carbide precursors a) NbC, b) SiC, c) TaC, d) TiC, e) VC, and f) ZrC.

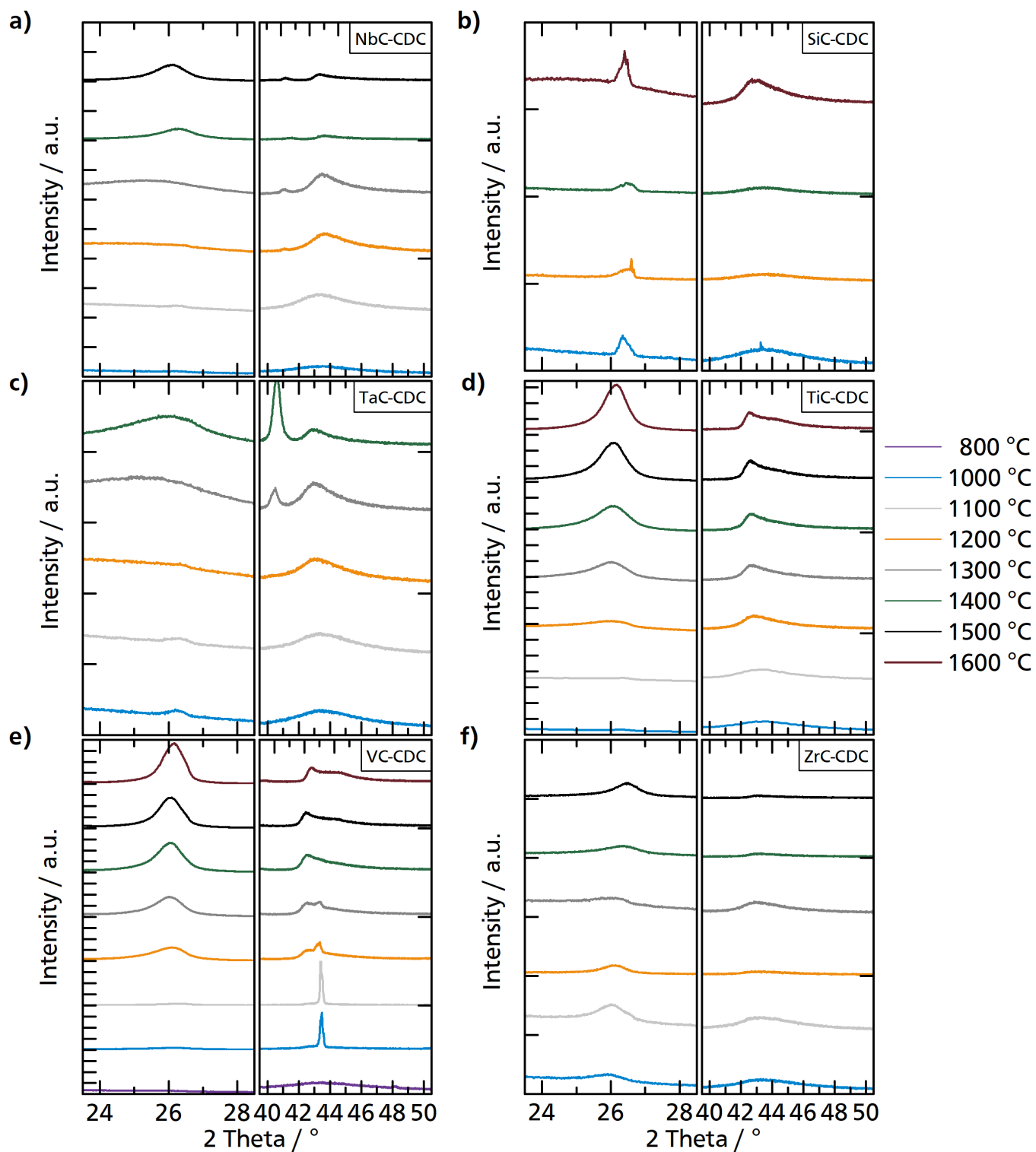


Figure B.2: X-Ray powder diffraction patterns of CDCs synthesized at different temperatures from the carbide precursors a) NbC, b) SiC, c) TaC, d) TiC, e) VC, and f) ZrC.

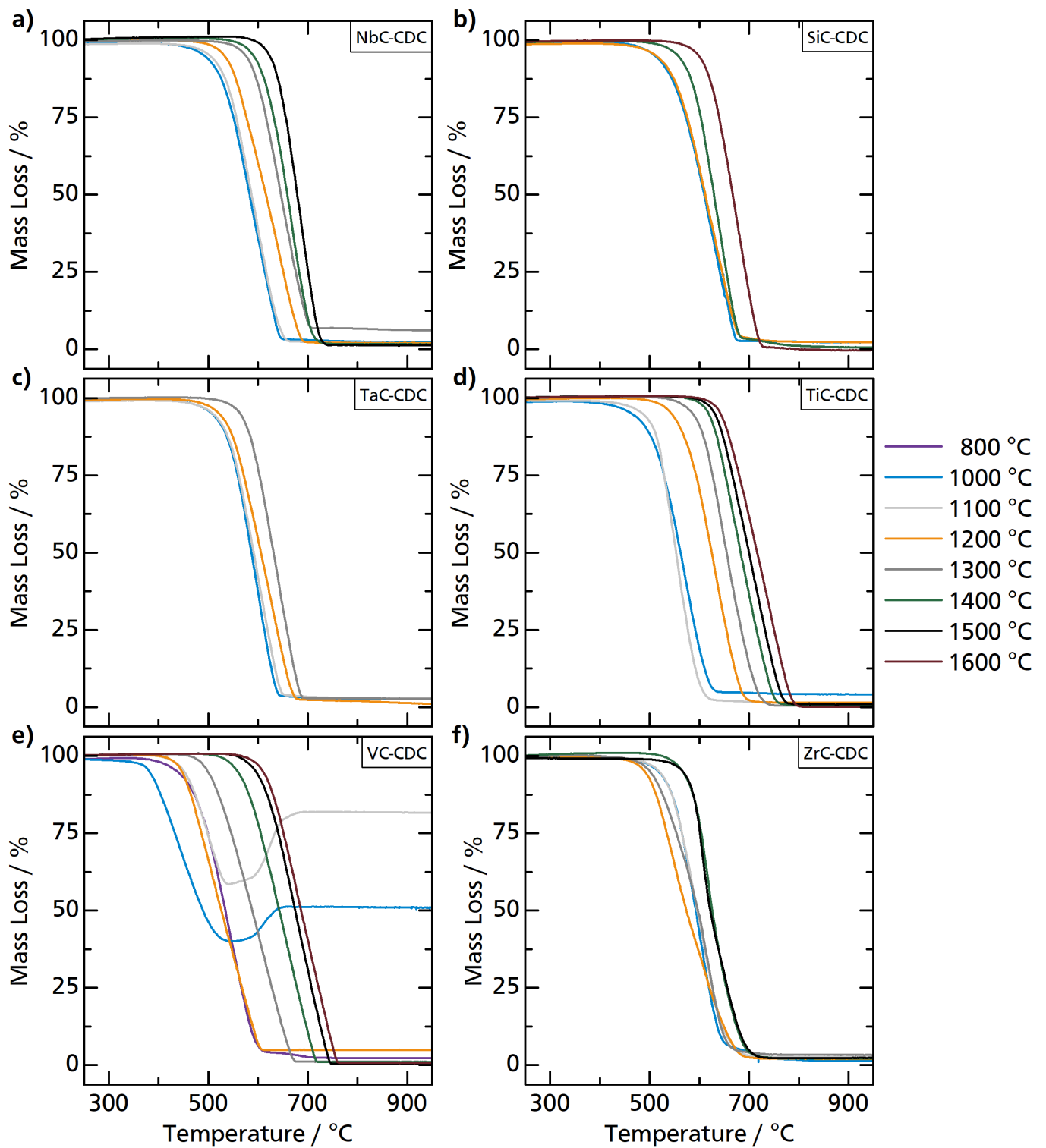


Figure B.3: Mass loss curves from temperature-programmed oxidation of CDCs synthesized at different temperatures from the carbide precursors a) NbC, b) SiC, c) TaC, d) TiC, e) VC, and f) ZrC.

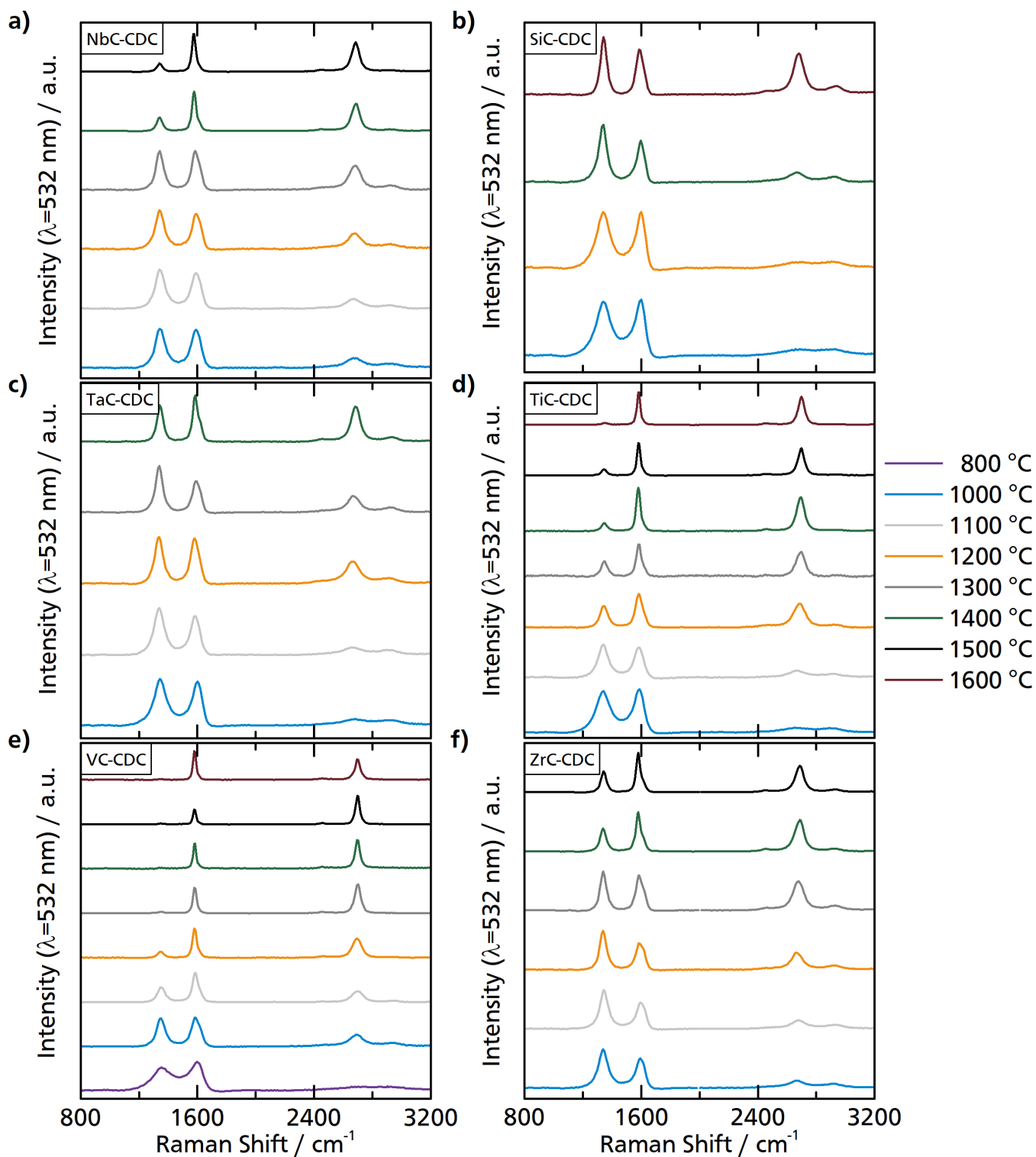


Figure B.4: Raman spectra of CDCs synthesized at different temperatures from the carbide precursors a) NbC, b) SiC, c) TaC, d) TiC, e) VC, and f) ZrC.

C Exemplary Application of Pt/C Catalysts in Oxygen Reduction Reaction

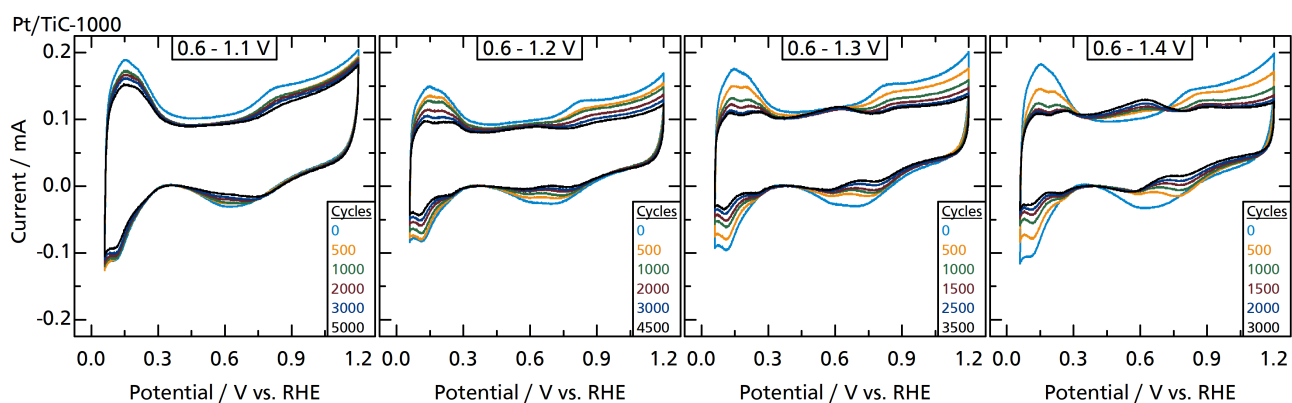


Figure C.1: Cyclic voltammograms from the catalyst Pt/TiC-1000 during accelerated durability tests in the ranges 0.6 - 1.1 V, 0.6 - 1.2 V, 0.6 - 1.3 V, and 0.6 - 1.4 V.

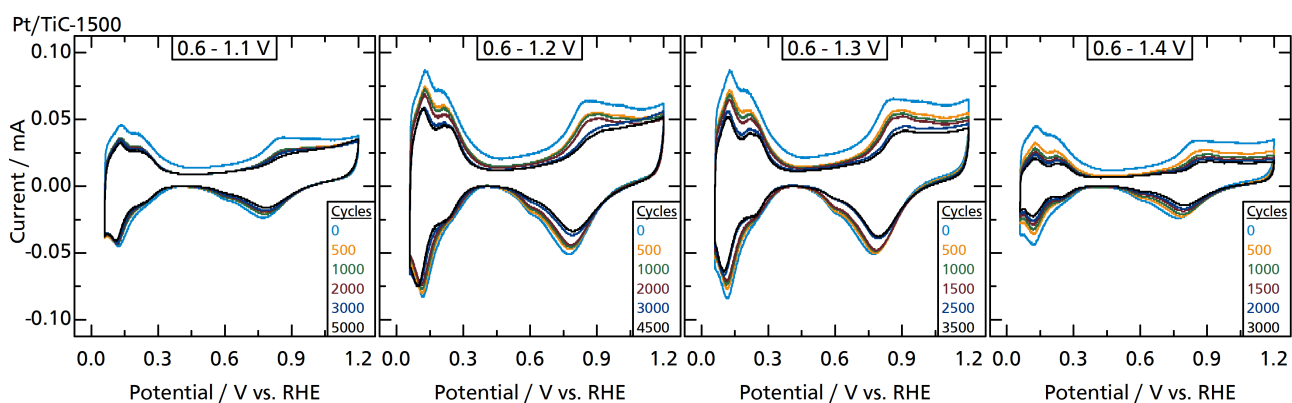


Figure C.2: Cyclic voltammograms from the catalyst Pt/TiC-1500 during accelerated durability tests in the ranges 0.6 - 1.1 V, 0.6 - 1.2 V, 0.6 - 1.3 V, and 0.6 - 1.4 V.

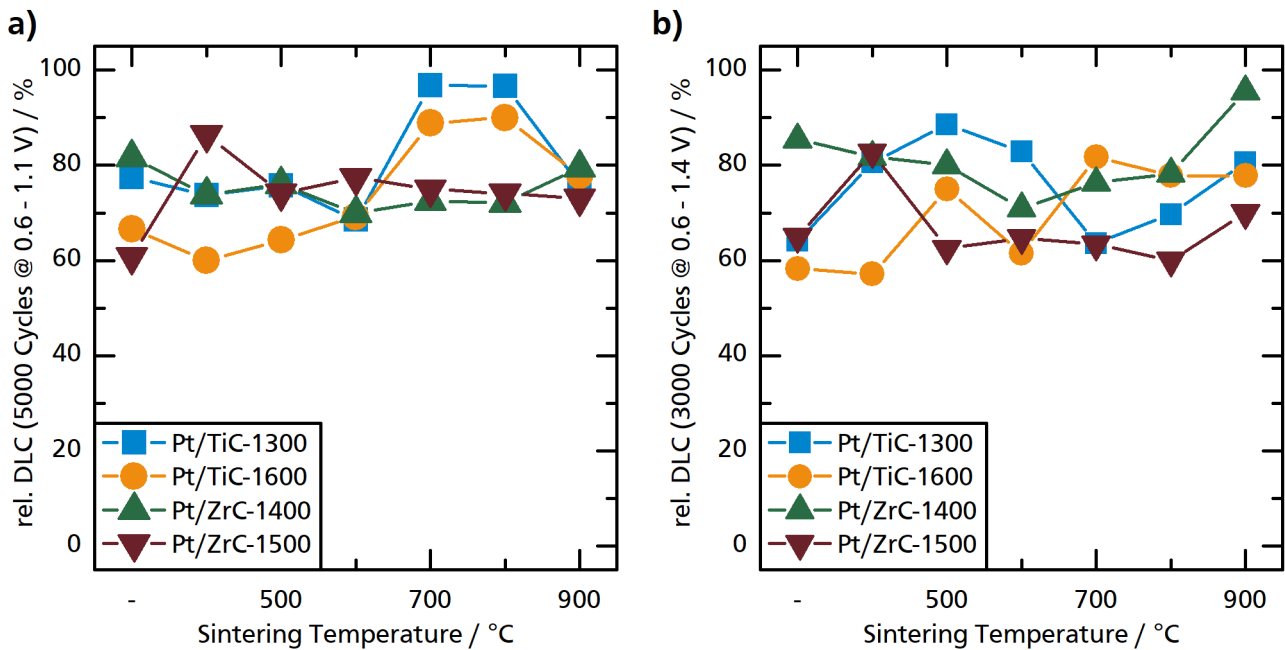


Figure C.3: Influence of sintering temperature on relative double layer capacitance after accelerated durability tests with **a)** 5000 cycles at 0.6 - 1.1 V, and **b)** 3000 cycles at 0.6 - 1.4 V for the catalysts Pt/TiC-1300, Pt/TiC-1600, Pt/ZrC-1400, and Pt/ZrC-1500.

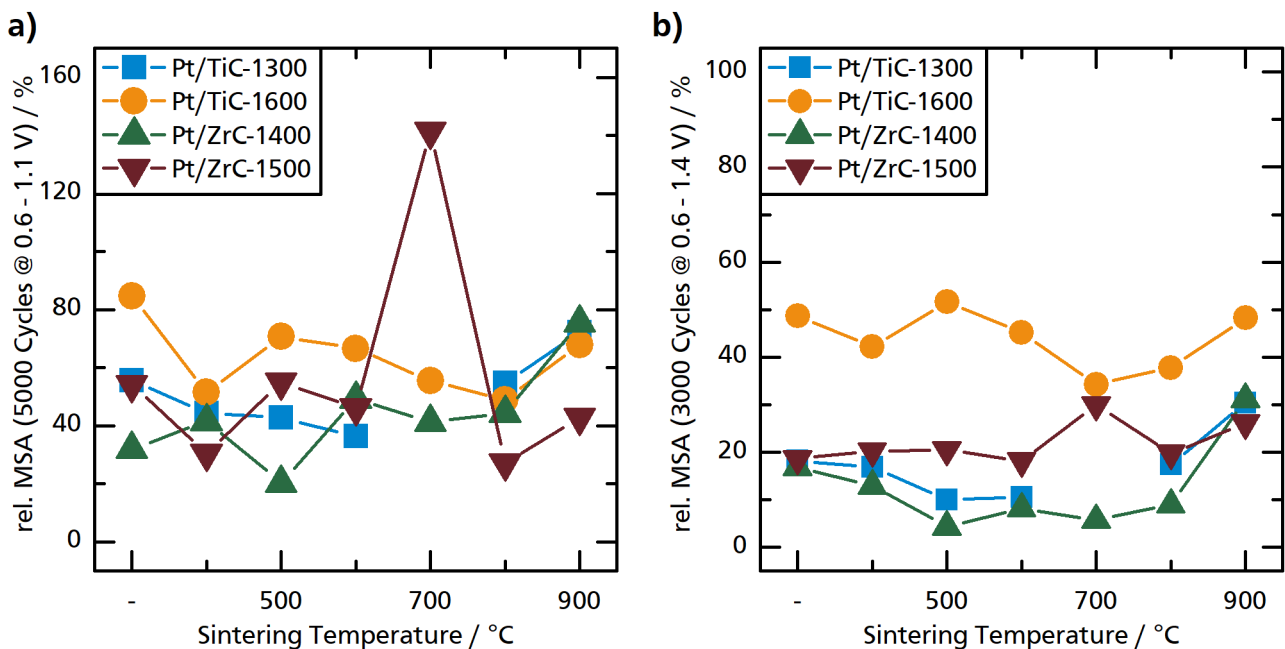


Figure C.4: Influence of sintering temperature on relative mass specific activity after accelerated durability tests with **a)** 5000 cycles at 0.6 - 1.1 V, and **b)** 3000 cycles at 0.6 - 1.4 V for the catalysts Pt/TiC-1300, Pt/TiC-1600, Pt/ZrC-1400, and Pt/ZrC-1500.